The Impact of Oil-Based Muds and Formation Damage on the CO_2 Hydrate Formation in Depleted Reservoirs :

Micromodel Experiments and Coupled Wellbore-Reservoir Simulations

Mohammad Wildan Alfian

Delft University of Technology

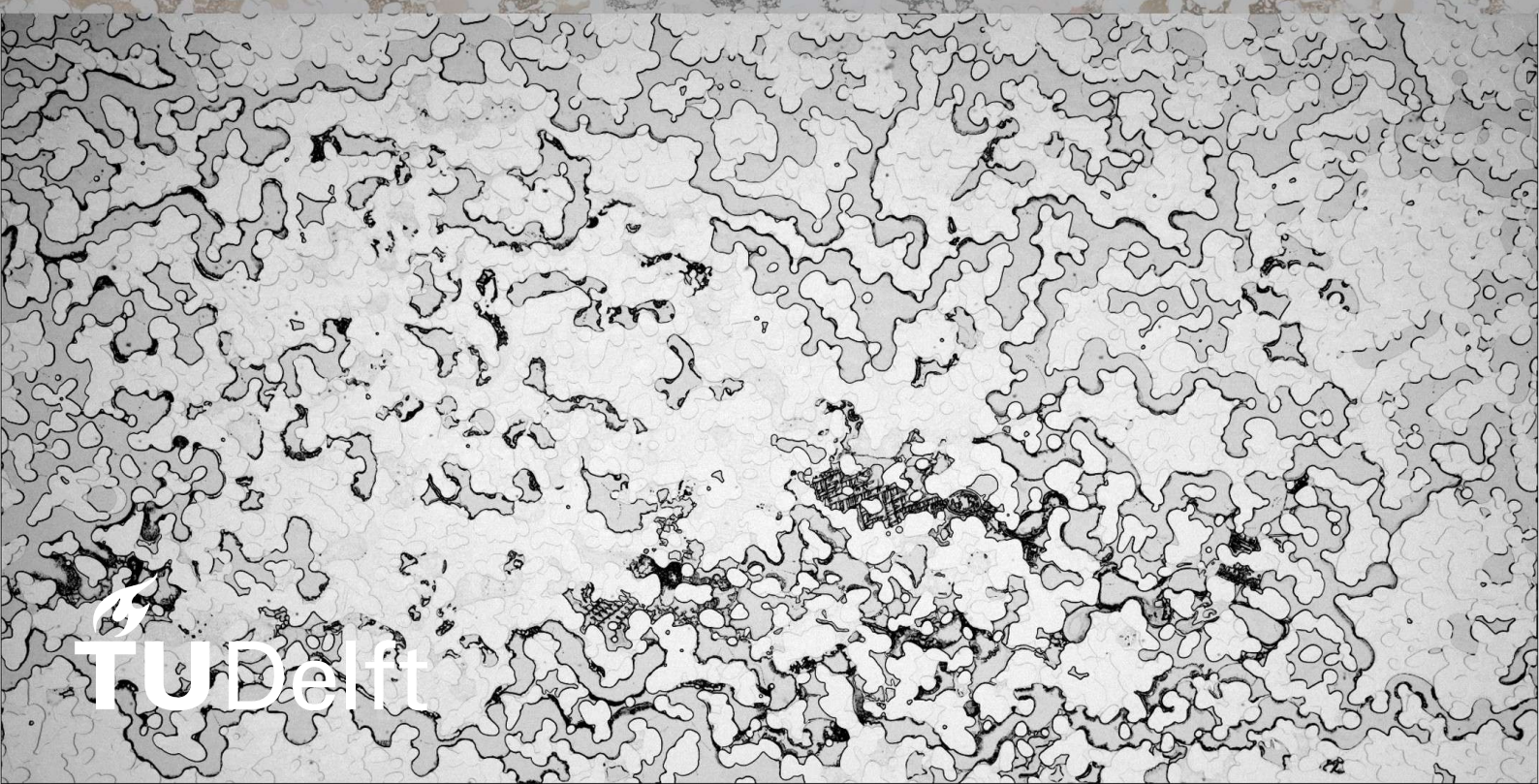

TU Delft

The Impact of Oil-Based Muds and Formation Damage on the CO_2 Hydrate Formation in Depleted Reservoirs :

Micromodel Experiments and Coupled Wellbore-Reservoir Simulations

by

Mohammad Wildan Alfian

Student Number : 5958474

to obtain the degree of Master of Science

at the Delft University of Technology,

to be defended publicly on Tuesday, August 19th, 2025 at 14:00 CEST.

Chair and Main Supervisor:	Dr. Rouhi Farajzadeh	TU Delft
Co-Supervisor:	Dr. Diederik Boersma	TU Delft
Daily Supervisor:	Dr. Lifei Yan	TU Delft
Graduation Committee Member :	Dr. Denis Voskov	TU Delft
Graduation Committee Member :	Dr. Anne Pluymaker	TU Delft
Project Duration:	November, 2024 - August, 2025	
Faculty:	Faculty of Civil Engineering and Geosciences	

Acknowledgement

I would like to express my deepest gratitude to my supervisory team for their invaluable guidance, constructive feedback, and insightful discussions that have enabled me to complete this thesis successfully. My sincere thanks go to my principal supervisor, Dr. Rouhi Farajzadeh, whose presence and guidance were strongly felt despite our interactions being conducted online while he was based in Oman. His direction has left a lasting impression on my academic journey. I am also grateful to my co-supervisor, Dr. Diederik Boersma, for his motivation, engaging discussions, and thought-provoking questions that encouraged me to think more critically. Special thanks to my daily supervisor, Dr. Lifei Yan, for guiding me through the experiments from the very beginning, starting from zero, until I was able to work independently, and for always making time for discussions even during his leave.

I would also like to thank Dr. Denis Voskov, a member of my thesis committee and lead of the ASSET Team, for his consistent input during the weekly ASSET meetings, mid-term review, and greenlight meeting. My gratitude also goes to Dr. Anne Pluymakers, as thesis committee member, for her highly valuable suggestions during the greenlight meeting, which significantly improved the quality of this thesis.

I am thankful to Michiel Slob, the lab supervisor, for his assistance in setting up experiments, his practical advice during lab work, and the many thoughtful conversations about life. My thanks also go to Dr. Sian Jones for her constant support in the laboratory and for helping me perform additional analyses that strengthened the findings for my experiments.

Special thanks to Sajjad Moslehi for sharing the DARTS-well code and providing detailed guidance on performing coupled wellbore–reservoir simulations. Although not part of the official supervisory team, his help and feedback were essential to completing the simulation work.

I would also like to acknowledge my lab colleague from the University of Manchester, Saleh Mohammadrezaei, who was a great discussion partner in both experimental work and image analysis. Working together in the lab and exchanging ideas with you was truly a memorable experience.

My heartfelt thanks go to my colleagues in the ASSET Team, fellow Geo-Energy Engineering students, the Applied Earth Sciences students, and all my fellow Indonesian students in Delft. The interactions, laughter, and shared experiences have made my two-year academic journey truly special, and I hope we will maintain these bonds for years to come.

I am deeply grateful to the Indonesian Endowment Fund for Education Agency (LPDP) for providing the financial support that allowed me to pursue my dream of continuing my studies abroad. My thanks also go to Pertamina for granting me the opportunity to take a study leave to enhance my knowledge and experience.

Beyond my academic life, my deepest gratitude goes to my wife, Neni Anggraheni, for supporting my great decision to study abroad and for being my greatest source of strength. This journey has been not only an academic pursuit but also a life experience that has made our family stronger and more united. Without your support, I could not have achieved this. To my beloved children, Umar, Khansa, and Hafsah, thank you for being my constant source of joy and motivation. I hope these two years will leave you with cherished memories and valuable lessons for your future.

I want to thank my mother and my brother for their unwavering prayers and support in every decision I have made. Lastly, I dedicate my deepest appreciation to my late father and my late father-in-law, whom we will no longer be able to see when we return to Indonesia. May they be granted the best place by His side. I believe that if they were still with us, they would be proud of the accomplishments and experiences we have gained.

Mohammad Wildan Alfian
Delft, August 2025

Summary

Carbon Capture and Storage (CCS) is an effective method for reducing CO_2 emissions by permanently storing captured CO_2 underground. Depleted oil and gas fields are promising CCS targets due to their well-characterised nature. However, injecting high-pressure CO_2 into low-pressure reservoirs can lead to hydrate formation due to Joule-Thomson (JT) cooling and phase changing during CO_2 injection, potentially reducing injectivity.

Since hydrate formation mainly occurs in the near-wellbore, it is essential to assess the influence of mud filtrate and formation damage on CO_2 hydrate formation. Oil-based mud (OBM) can invade the formation, making its filtrate the first material to interact with injected CO_2. This study addressed the impact of the synthetic OBM filtrate, represented by dodecane, $CaCl_2$-15wt%, and W/O emulsion, on CO_2 hydrate formation in micromodel experiments, focusing on hydrate morphology and saturation.

Results show that the interaction between CO_2 and synthetic OBM filtrate can induce CO_2 hydrate formation under certain pressure-temperature conditions. Instability of the OBM filtrate emulsion during low-temperature CO_2 injection, followed by water droplet coalescence, increases the water-CO_2 contact area, thereby promoting hydrate formation. Experiments involving oil and W/O emulsion revealed a distinct hydrate morphology, with hydrates present not only at the CO_2-water interface but also within the CO_2 flow pathways.

The study also highlights that high salinity $CaCl_2$–15wt% acts as a CO_2 hydrate inhibitor. In the presence of synthetic OBM filtrate, hydrate saturation is higher than in the system containing only $CaCl_2$–15wt% or a combination of $CaCl_2$–15wt% and dodecane, likely due to enhanced water–CO_2 contact from droplet coalescence in the W/O emulsion.

Furthermore, the impact of formation damage on near-wellbore pressure and temperature relative to the hydrate stability zone (HSZ) was examined. Mud filtrate can reduce permeability, while hydrate formation can exacerbate this damage. Such changes alter local thermodynamic conditions, requiring a coupled wellbore–reservoir simulation to capture the dynamic interactions.

Simulation results indicate that greater formation damage may reduce the risk of hydrate formation by increasing the temperature and pressure in the near-wellbore. If hydrate occurs and leads to additional permeability impairment, it could result in increased bottom-hole temperatures. Such a temperature rise may help dissociate the hydrates, provided the increase is sufficient to shift the system out of the HSZ. Formation damage due to mud filtrate (30-60% permeability reduction) typically keeps pressure and temperature conditions within the HSZ. Additional damage due to hydrate formation (80-90% permeability reduction) significantly increases bottom-hole pressure (BHP) and bottom-hole temperature (BHT), thus shifting the pressure and temperature conditions outside the HSZ. Notable changes in both BHP and BHT occur when the radius of the damaged zone increases from 0 to approximately 0.5 meters. Beyond this threshold, further increases in damaged radius result in only marginal BHP and BHT changes.

Contents

List of Figures

List of Tables

Nomenclature

Abbreviations

Abbreviation	Definition
BH	Bottom Hole
BHP	Bottom Hole Pressure
BHT	Bottom Hole Temperature
$CaCl_2$	Calcium Chloride
CCS	Carbon, Capture, and Storage
CCUS	Carbon, Capture, Utilization, and Storage
CO_2	Carbon Dioxide
DARTS	Delft Advance Reservoir Terra Simulator
DFM	Drift-Flux Model
EOR	Enhanced Oil Recovery
HEL	Hydrate Equilibrium Line
HLB	Hydrophilic-Lipophilic Balance
HQP	High Quadruple Point
HSZ	Hydrate Stability Zone
IEAGHG	International Energy Agency Greenhouse Gas R&D Programme
IFT	Interfacial Tension
IHWG	Ice-Hydrate-Water-Gas
IOGP	International Association of Oil & Gas Producers
JT	Joule-Thomson
LCT	Labile Cluster Theory
LQP	Low Quadruple Point
MEG	Mono Ethylene Glycol
$MtCO_2$	Million ton of CO_2
NaCl	Natrium Chloride
OBL	Operator-Based Linearization
OBM	Oil-Based Mud
OWR	Oil-Water-Ratio
PT	Pressure and Temperature
PV	Pore Volume
ROI	Region of Interest
S_{hyd}	Hydrate Saturation
S_o	Oil Saturation
S_w	Water Saturation
v/v	Volume/Volume
WBM	Water-Based Mud
WH	Wellhead
WHP	Wellhead Pressure
WHT	Wellhead Temperature
$WHL_{CO2}G$	Water-Hydrate-Liquid CO_2-Gas
W/O	Water-in-oil

Symbols

Symbol	Definition	Unit
dP_{nwb}	pressure difference in the near-wellbore	[bar]
dP_{well}	pressure difference in the wellbore	[bar]
f_{conv}	conversion factor	[-]
n_{H_2O}	total number of water moles	[moles]
H	enthalpy	[kJ/kg]
II	injectivity index	[kg/s/bar]
k	permeability	[mD]
k_d	damaged-zone permeability	[mD]
k_0	undamaged-zone permeability	[mD]
$k_{SH=0}$	initial permeability before hydrate formation	[mD]
Mw^{H_2O}	molecular weight of water	[g/mol]
Mw^{CO_2}	molecular weight of CO_2	[g/mol]
N_H	number of water molecules per CO_2 molecule	[-]
P_{res}	reservoir pressure	[bar]
q	CO_2 injection rate	[kg/s]
r_d	damaged-zone radius	[m]
r_w	wellbore radius	[m]
S	skin factor	[-]
T_{res}	reservoir temperature	[°C]
∂p	pressure change	[bar]
∂T	temperature change	[°C]
ΔP	pressure difference	[bar]
μ_{JT}	Joule-Thomson coefficient	[°C/bar]
ρ_H	hydrate density	[g/cm^3]
ρ_w	brine density	[g/cm^3]

1

Introduction

1.1. Relevance of the Study

Carbon Capture and Storage (CCS) is one of the effective methods for reducing carbon dioxide (CO_2) emissions, as it captures CO_2 and stores it permanently underground to prevent atmospheric release (Davoodi et al., 2023; Schellart, 2024) as illustrated in Figure 1.1. However, to create a substantial global impact, CCS projects must be implemented on a large scale, with continuous improvements in storage sites and capacity in the coming years (Skogestad et al., 2024). CCS is a proven and safe technology that has been successfully implemented in Europe since 1996 through the Sleipner project in Norway, and it remains a key strategy to achieve climate neutrality (IOGP, 2025). Europe is actively promoting greater CO_2 storage and injection capacity, with 52 projects targeting a combined capacity of 126 $MtCO_2$/yr by 2030, 19 of which focus on depleted oil and gas reservoirs (IOGP, 2025).

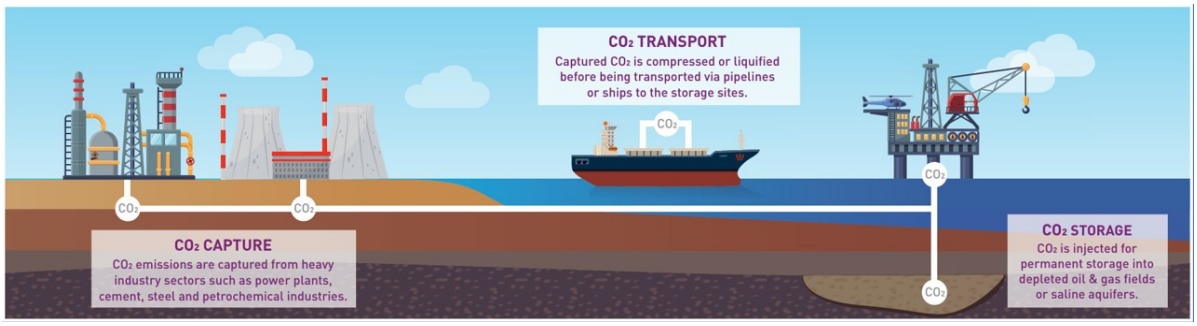

Figure 1.1: Illustration of CCS operation (IOGP, 2025).

One of the most promising targets for CCS is depleted oil and gas fields, as they are typically well-characterized during exploration, production, and post-production stages (IEAGHG, 2022). These reservoirs offer reliable capacity estimates, good storage integrity, and relatively high technical feasibility (Heidarabad and Shin, 2024). However, injecting high-pressure CO_2 into low-pressure depleted reservoirs leads to the Joule-Thomson (JT) cooling effect caused by the isenthalpic expansion of CO_2 and also phase changing of the CO_2 which creates the pressure and temperature condition at the phase boundary between gas and liquid which can severely reduce the temperature of the well and reservoir (IEAGHG, 2024). When CO_2 contact with water at this low temperature, it poses a risk of hydrate formation that can significantly reduce CO_2 injectivity into the reservoir (IEAGHG, 2024; Indina et al., 2024; Hoteit, Fahs, and Soltanian, 2019).

Since hydrate formation primarily occurs in the near-wellbore region, evaluating the impact of the near-wellbore condition on CO_2 hydrate formation is essential. This region is often affected by the invasion of mud filtrate during drilling and is also where the formation damage is most likely to occur. Such damage, typically in the form of reduced permeability, can alter local pressure and temperature conditions during

CO_2 injection. Furthermore, if CO_2 hydrate forms in this region, it can act as an additional source of formation damage, further influencing the pressure–temperature behavior near the wellbore.

Oil-based mud (OBM) is a type of the drilling fluid that commonly used for drilling in depleted reservoirs (Orun, Akpabio, and Agwu, 2023). OBM provides better thermal and chemical stability than water-based mud (WBM), particularly in complex shale formations, and offers improved lubrication while reducing corrosion from gases like CO_2 and H_2S. OBM is a water-in-oil (W/O) emulsion, typically consisting of base oil as the continuous phase, water (brine) as the dispersed phase, and various additives such as emulsifiers, weighting agents, filtration control agents, and viscosifiers (J. Li et al., 2022). Filtrate invasion during drilling and completion can cause formation damage in the near-wellbore region (Emiliani et al., 2005). During CO_2 injection, the gas first contacts the invaded zone before reaching the main reservoir. Therefore, assessing the effect of OBM filtrate on CO_2 hydrate formation is critical, particularly in the near-wellbore region.

The role of OBM in hydrate risk has been well studied in drilling operations. Grigg and Lynes (1992) found that OBM acts as a methane hydrate inhibitor in deepwater drilling environments. Similarly, Skogestad et al. (2024) evaluated the capability of OBM to mitigate CO_2 hydrate formation in CCS applications targeting depleted reservoirs. However, most of these studies rely on bulk-phase models to evaluate hydrate risk during drilling. The effect of OBM on CO_2 hydrate formation in porous media, especially in the context of CO_2 injectivity, remains underexplored.

OBM as an emulsion composed of oil, brine, emulsifiers, and other chemical additives, presents a complex system whose interaction with CO_2 hydrate formation in porous media is still not well understood. Previous studies have shown that oil can act either as a promoter or inhibitor of hydrate formation, depending on its type and concentration. However, all such studies have been conducted in bulk systems. As a result, critical aspects such as hydrate morphology and its effects on permeability impairment in porous structures remain unknown. No existing literature has been found that experimentally investigates the impact of oil and its components on CO_2 hydrate formation within porous media.

The role of salt as an hydrate inhibitor has been extensively studied, particularly in bulk fluid systems. However, when both brine and oil are present, the interaction and behavior of CO_2 hydrate formation become significantly more complex and are not yet well understood. This knowledge gap becomes even more pronounced in the case of emulsions, where the mechanisms governing CO_2 hydrate formation and stability remain largely unexplored.

This research addresses this gap by evaluating the impact of the primary components of OBM filtrate, such as base oil, brine, and W/O emulsion, on CO_2 hydrate formation in porous media. Dodecane, $CaCl_2$-15wt%, and Span80 were used to represent base oil, brine, and emulsifier, respectively, in creating a W/O emulsion as synthetic OBM filtrate. The study aims to improve the understanding of how OBM filtrate and its main components influence CO_2 hydrate saturation, particularly in micromodel experiments.

Lastly, current simulations of CO_2 storage and the associated risk of CO_2 hydrate formation predominantly focus on dynamic behavior at the reservoir region. In contrast, studies that specifically investigate the near-wellbore region remain very limited. As CO_2 hydrates are most likely to form in the near-wellbore zone, where complex interactions, such as formation damage in the invaded zone, can significantly affect injectivity and overall storage performance, the study of the near-wellbore dynamics is essential. Furthermore, the pressure and temperature change in the near-wellbore due to permeability reduction can trigger dynamics hydrate formation and dissociation.

An accurate analysis of this region must also account for the dynamic conditions within the wellbore during CO_2 injection, since bottomhole parameters derived from the wellbore model serve as input for the reservoir simulation (Estrada, 2023). Neglecting wellbore processes in CCS operations can lead to inaccurate predictions of bottomhole pressure and temperature, as well as an oversimplified representation of wellbore–reservoir interactions, which compromises the reliability of numerical simulations (Moslehi and D. Voskov, 2025). Therefore, to obtain more realistic and reliable predictions, it is essential to model this interaction using a coupled wellbore–reservoir simulation approach (Moslehi and D. Voskov, 2025).

1.2. Research Questions

This research aims to investigate the following key questions:

Question 1: What are the effects of the synthetic OBM filtrate as the fluid/chemical component, represented by dodecane, $CaCl_2$-15wt%, and W/O emulsion, on the formation of the CO_2 hydrate in porous media?

- What are the characteristic morphologies of CO_2 hydrate in the presence of the synthetic OBM filtrate?
- How does the presence of the synthetic OBM filtrate influence the CO_2 hydrate saturation in the micromodels?

Question 2: What is the impact of formation damage on the pressure and temperature in the near-wellbore in relation to the CO_2 hydrate stability zone?

1.3. Report Structure

This thesis is systematically structured to address the research objectives and questions outlined in section 1.2. It comprises seven chapters, each contributing to a comprehensive investigation of the influence of oil-based mud and formation damage on CO_2 hydrate formation in depleted reservoirs. The chapters are organized as follows:

- **Chapter 1 - Introduction:** Explains the relevance of the study, presents the research questions and scope, and outlines the overall structure of the report.
- **Chapter 2 - Theoretical Background:** Reviews the literature and fundamental concepts, including CCS in depleted reservoirs, the Joule-Thomson cooling effect, CO_2 hydrate formation, oil-based mud, formation damage near the wellbore, applications of the micromodel experiments, and coupled wellbore-reservoir simulation.
- **Chapter 3 - Methodology:** Describes the experimental setup and procedures for the micromodel experiments, along with image analysis and data processing methods. It also introduces the assumptions and parameters for the wellbore and reservoir models, initial and boundary conditions, simulation tools used, and the sensitivity scenarios for the coupled wellbore-reservoir simulations. This chapter also explains the key assumptions and limitations of both the experiments and simulations.
- **Chapter 4 - Micromodel Experiment Results:** Presents and analyzes the results of each experiment, including the hydrate morphology, hydrate saturation, and dissociation temperature.
- **Chapter 5 - Coupled Wellbore-Reservoir Simulation Results:** Provides simulation results on the impact of permeability of the damaged zone and radius of the damaged zone on the pressure and temperature in the near-wellbore in relation to CO_2 hydrate stability zone.
- **Chapter 6 - Discussions:** Discusses findings from the experiments and simulations to answer the research questions.
- **Chapter 7 - Conclusions and Recommendations:** Summarizes the key outcomes of the study, answers the research questions, and provides recommendations for future research.

2

Theoretical Background

2.1. CCS in Depleted Reservoirs and Near-Wellbore Cooling Effect

CCS is recognized as one of the key strategies for reducing atmospheric CO_2 emissions from human activities. It involves a series of technological steps: capturing and concentrating CO_2 from industrial and energy-related sources, transporting it to a suitable storage site, and injecting it into a subsurface rock formation for long-term isolation from the atmosphere. Several types of geological formations have been extensively studied for CO_2 storage, including depleted oil and gas reservoirs, deep saline aquifers, unmineable coal seams, and basalt formations. (Metz et al., 2005; IOGP, 2025)

Depleted fields are among the most favourable sites for CO_2 injection due to their well-characterised properties throughout the exploration, production, and possibly post-production phases (IEAGHG, 2022). Their storage capacities are well known, and they typically offer good containment and high technical feasibility (Heidarabad and Shin, 2024). These fields are characterized by low reservoir pressures as a result of hydrocarbon extraction during production. According to C. M. Oldenburg, Pruess, and Benson (2001), pressures in depleted gas reservoirs generally range from 20 to 50 bar, with temperatures between 27–120 °C. In contrast, CO_2 is commonly injected in a dense phase at high pressure. As a result, injecting high-pressure CO_2 into low-pressure depleted reservoirs can lead to the JT cooling effect, caused by isenthalpic expansion. Additionally, phase changing of the CO_2 during injection, which creates the pressure and temperature condition at the phase boundary between gas and liquid, can severely reduce the temperature of the well and reservoir (IEAGHG, 2024). When CO_2 contact with water at this low temperature, it poses a risk of hydrate formation that can significantly reduce CO_2 injectivity into the reservoir (IEAGHG, 2024; Indina et al., 2024; Hoteit, Fahs, and Soltanian, 2019).

JT cooling is a phenomenon that refers to the temperature drop experienced by a real gas, such as CO_2, during expansion from high pressure to low pressure at constant enthalpy (adiabatic conditions). This occurs due to a sudden volume increase, which increases intermolecular distance and reduces kinetic energy, especially in non-ideal gases. During CO_2 injection into depleted gas reservoirs, where reservoir pressure is extremely lower than the injection pressure, this cooling effect can be significant. The system is typically considered adiabatic, meaning no heat is exchanged with the surroundings. Therefore, the expansion results in a change in internal energy and potential energy, with no external heat input. The JT cooling process is at constant enthalpy. From experiments, the temperature change with respect to pressure at constant enthalpy defines the Joule-Thomson coefficient as described in Equation 2.1. (Curtis M. Oldenburg, 2007; Scheffer, 2022)

$$\mu_{JT} = \left(\frac{\partial T}{\partial p}\right)_H \tag{2.1}$$

A positive μ_{JT} implies cooling during expansion. The magnitude of μ_{JT} indicates the cooling intensity, which is important in predicting temperature changes and assessing thermal impacts during CO_2 injection.

Figure 2.1a shows the CO_2 injection process from the CO_2 capture and compression station to its injection into the reservoir. During pre-injection, the CO_2 is compressed into a supercritical fluid (A). The bubble point of CO_2 is much higher than the reservoir pressure. As CO_2 flows through the pipeline to the wellhead, pressure and temperature decrease, leading to a phase change from supercritical to liquid (B). Subsequently, CO_2 vaporizes within the tubing and near the wellbore. Due to the significant difference between the injection pressure and reservoir pressure, the CO_2 density drops sharply (C) (Hoteit, Fahs, and Soltanian, 2019). Along with the Joule-Thomson cooling process, the vaporization process leads to latent heat absorption, which also significantly cools down the surroundings.

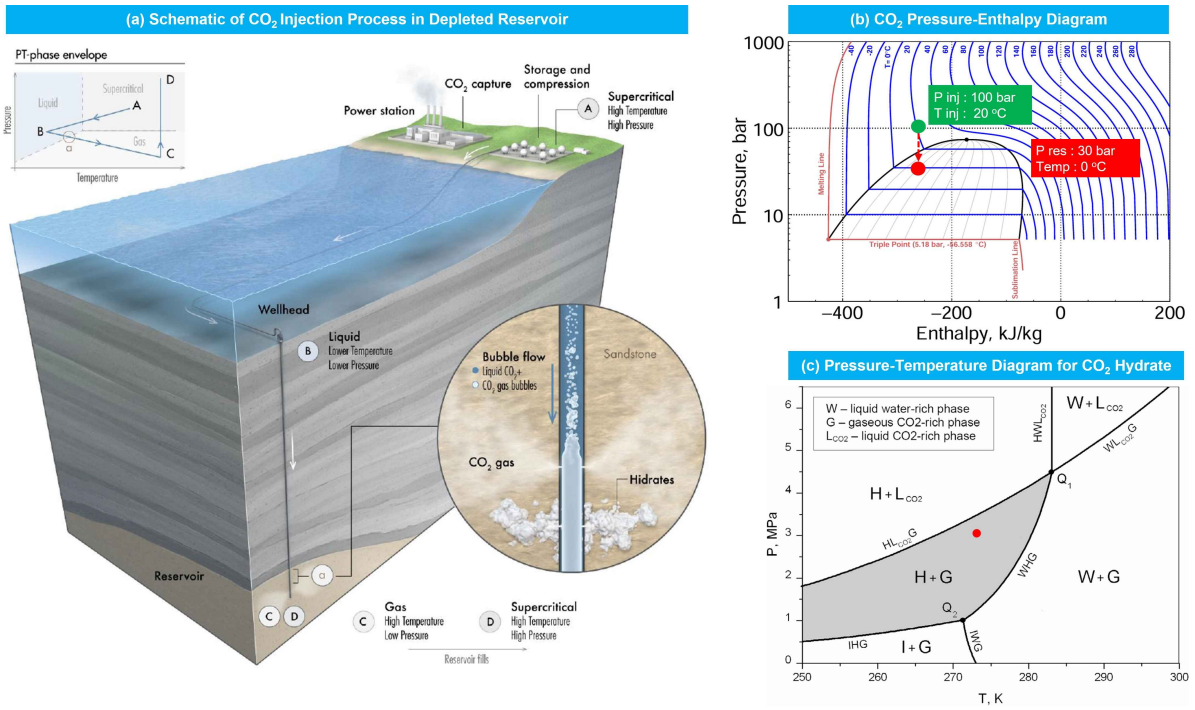

Figure 2.1: (a) Schematics of CO_2 injection process in depleted reservoir (Hoteit, Fahs, and Soltanian, 2019), (b) CO_2 Pressure-Enthalpy Diagram (diagram adapted from (Lavrik, 2017)), (c) Pressure and Temperature Diagram for binary system water-CO_2. Thick lines are three phase-equilibrium curve. Gray area is region of two-phase hydrate-gas equilibrium. Q1 and Q2 mark the upper ($WHL_{CO2}G$) and lower (IHWG) quadruple point, respectively. (Voronov et al., 2016). Green dot illustrates the pressure and temperature injection in the wellhead, while red dot illustrates pressure and temperature in the near-well during CO_2 injection.

Figure 2.1b illustrates the significant temperature change during CO_2 injection in a depleted reservoir. Assuming an injection pressure of 100 bar and an injection temperature of 20 °C (green point), when injecting CO_2 into a depleted reservoir with a reservoir pressure of 30 bar, the isenthalpic cooling effect causes the temperature in the reservoir/wellbore to drop significantly to 0 °C (red point). This condition leads the near-wellbore condition to enter the CO_2 hydrate stability zone (HSZ), illustrated by the grey area in Figure 2.1c.

2.2. CO_2 Hydrate Formation in Porous Media

CO_2 hydrates are crystalline, ice-like solids that form when low molecular weight gases and water molecules combine under specific thermodynamic conditions (Sloan and Koh, 2008). In this structure, water molecules create a hydrogen-bonded lattice that traps CO_2 molecules inside cage-like cavities (Sloan and Koh, 2008; Mahnaz Aghajanloo, Lifei Yan, et al., 2024). Figure 2.1c shows an example of a pressure–temperature diagram for CO_2 hydrate. The hydrates form within the HSZ, as indicated by the grey area. Induction times for hydrate nucleation are stochastic and difficult to predict, while metastable states can occur during the hydrate growth phase (Sloan and Koh, 2008). The hydrate formation process depends on several factors, such as fluid composition, geometry, surface area, water contaminant, degree of turbulency, presence of additives, and degree of subcooling (Sloan and Koh, 2008; Gambelli, Filipponi, and Rossi, 2022).

There is a notable distinction between hydrate formation in bulk fluids and within porous media. Porous media possess a high specific surface area, enhancing the gas–water interface and offering abundant solid surfaces for water molecules to organize and initiate nucleation. However, when pore sizes are relatively large, hydrate formation conditions resemble those of the bulk phase, as gas molecules tend to occupy micropores where water activity is minimal. As pore size decreases, the risk of hydrate formation is reduced due to lower water activity caused by dominant capillary forces, which shift the hydrate phase boundary to the left. Consequently, hydrate dissociation temperatures in porous media are lower than in bulk systems, also attributed to the influence of capillary forces.(Mahnaz Aghajanloo, Lifei Yan, et al., 2024)

2.3. CO_2 Hydrate Morphology and Permeability Reduction

In porous media, these hydrates can exhibit different morphologies, as depicted in Figure 2.2a and b. Based on their structural characteristics, hydrate morphologies are commonly classified into five main types, as shown in Figure 2.2b (Ren et al., 2020; Waite et al., 2009), as follows:

i) Grain-coating: hydrate forms around the grains and eventually encapsulates them;

ii) Cementing: hydrate cements the intergranular contacts;

iii) Pore-filling: hydrate grows freely within the pore space without connecting two or more grains;

iv) Load-bearing: hydrate bridges neighboring grains, contributing to mechanical stability by becoming part of the sediment framework;

v) Patchy: hydrate develops under pore-filling conditions and evolves through Ostwald ripening in mature, coarse-grained hydrate-bearing sediments.

Among these hydrate types, the grain-coating and pore-filling morphologies are more commonly found in hydrate-bearing sediments (Ren et al., 2020).

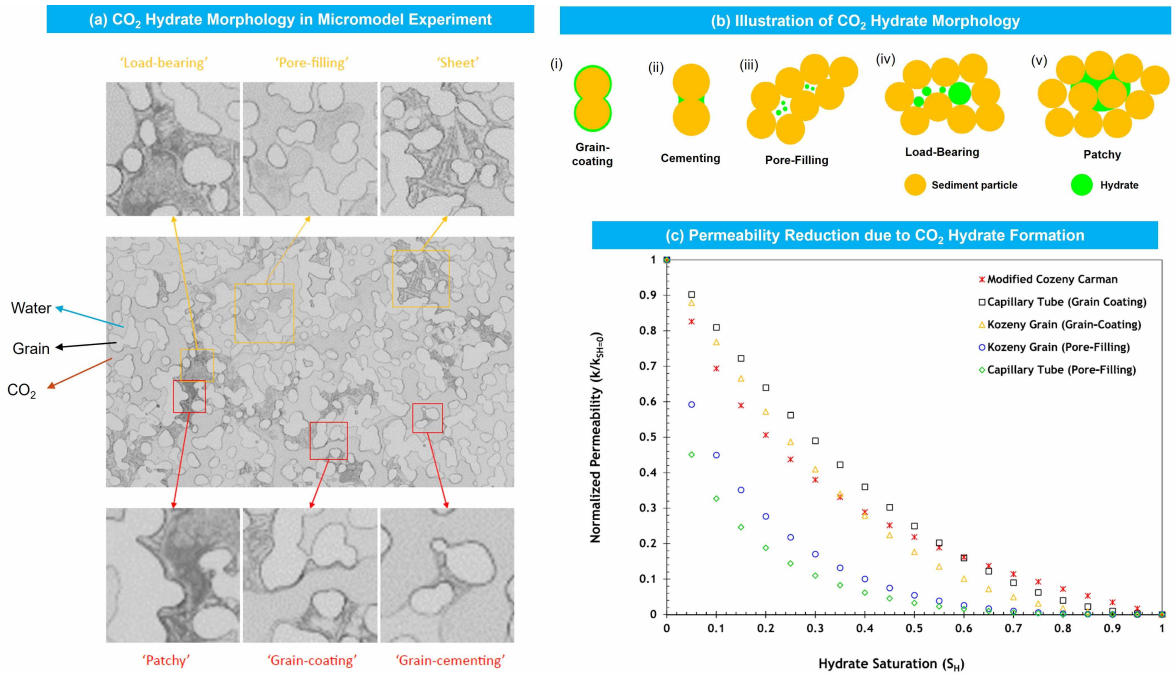

Figure 2.2: (a) Visual image of CO_2 hydrate morphology in micromodel experiment (Schellart, 2024), (b) illustration of CO_2 hydrate morphology (Ren et al., 2020) (c) Permeability reduction due to CO_2 hydrate formation (Mahnaz Aghajanloo, Lifei Yan, et al., 2024)

Figure 2.2a shows the morphology of CO_2 hydrate observed in a micromodel experiment reported by Schellart (2024). In the experiment, Schellart (2024) also identified a newly observed hydrate morphology: a sheet-like structure that had not been previously reported. The image clearly illustrates that, due to its solid phase, CO_2 hydrate can clog reservoir pores, significantly reducing both the porosity and

permeability of the rock. This reduction in permeability can hinder injectivity, thereby decreasing CO_2 storage efficiency and capacity. Additionally, the associated cooling effect may compromise long-term storage integrity and trigger thermal fracturing within the reservoir (Park, Berentsen, and Pater, 2024).

Figure 2.2c illustrates the impact of hydrate formation on permeability. Here, $k/k_{SH=0}$ represents the ratio of permeability after hydrate formation (k) to the initial permeability before hydrate formation $k_{SH=0}$. The figure clearly shows that rock permeability decreases significantly as hydrate saturation increases. Moreover, the type of hydrate morphology contributes differently to permeability impairment: at the same hydrate saturation, the pore-filling morphology results in greater permeability reduction compared to the grain-coating type. This impairment in permeability directly reduces the injectivity index of CO_2 injection. As permeability declines, achieving the same injection target requires higher pressure, as shown in Equation 2.2. In severe cases, hydrate formation may even drastically lower the injection rate.

$$II = \frac{q}{\Delta P} \tag{2.2}$$

where II is the injectivity index, q is the injection rate, and ΔP is the pressure difference between bottom hole and reservoir.

2.4. Dynamic of Well-Reservoir Interaction Influencing Hydrate Formation and Dissociation

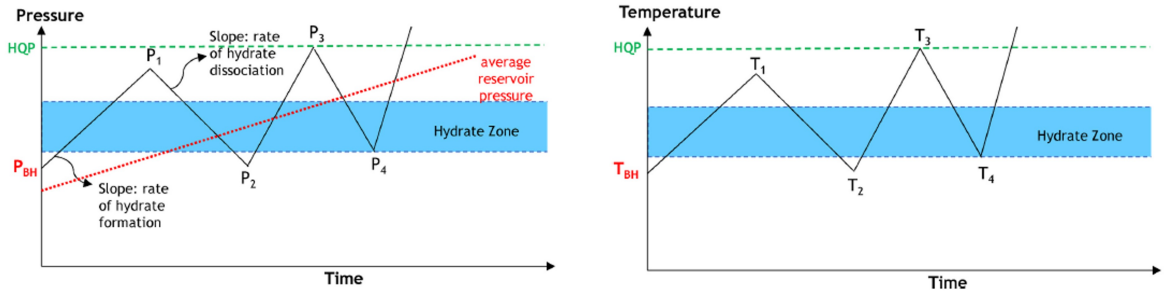

Figure 2.3: Dynamic change of bottom hole pressure and temperature during hydrate formation and dissociation (Mahnaz Aghajanloo, Lifei Yan, et al., 2024).

Mahnaz Aghajanloo, Lifei Yan, et al. (2024) discussed the dynamics of well-reservoir interaction, which influences the dynamics of hydrate formation and dissociation in the near-wellbore as illustrated in Figure 2.3. As expressed in Equation 2.2, the permeability drives the pressure drawdown in the sandface, between the porous medium connected to the well. This pressure drawdown influences the temperature of the bottomhole. If this temperature falls below the hydrate equilibrium point, CO_2 hydrates begin forming at the sandface, reducing permeability and raising wellbore pressure (P1), which subsequently increases temperature (T1). The rate at which pressure rises depends on how quickly hydrates form and how severely permeability is impaired. Once the temperature exceeds the hydrate equilibrium, dissociation begins, restoring permeability and lowering pressure. However, hydrate dissociation also releases CO_2, which can locally raise pressure. The slope of the pressure–temperature curve (P1–P2) is dictated by the hydrate dissociation rate. As pressure decreases, the well temperature also drops. Due to the self-preservation effect, not all encaged CO_2 may be released, resulting in residual pressure and temperature higher than before. With continued CO_2 injection, the reservoir pressure increases, and if the temperature again drops below the hydrate equilibrium, new hydrates can form. Owing to the water memory effect, subsequent hydrate formation may occur more rapidly and in greater volume or with a more compact structure. This cycle of formation and dissociation continues at the well–reservoir boundary until the reservoir pressure rises above the hydrate equilibrium line or high quadruple point (HQP).

2.5. Oil-Based Mud and Formation Damage

In this study, we focus on the oil-based muds (OBM) as drilling fluid for drilling CCS wells in depleted reservoirs. OBM is commonly used for drilling in depleted reservoirs due to their superior thermal and chemical stability compared to water-based muds (WBMs), particularly in complex shale formations. OBMs also offer improved lubrication and help mitigate corrosion from reactive gases such as CO_2 and H_2S.

OBMs are typically formulated as water-in-oil (W/O) emulsions, where the oil serves as the continuous phase and water (usually brine) is the dispersed phase. These emulsions also include various additives such as emulsifiers, weighting agents, filtration control agents, and viscosifiers (J. Li et al., 2022). The surfactants used in OBM formulations generally have low hydrophilic-lipophilic balance (HLB) values, ranging from 4 to 8, which supports the stability of W/O emulsions (Emiliani et al., 2005). During drilling, the OBM-filtrate, comprising the oil phase and excess surfactants, passes through the mud filter cake and invades the formation (Emiliani et al., 2005).

Filtrate invasion during drilling and completion can lead to near-wellbore formation damage. The OBM filtrate, when exposed to completion brine, may form persistent emulsion droplets that are difficult to remove, leading to irreversible reductions in permeability (Emiliani et al., 2005). Furthermore, interactions between the OBM filtrate and native formation fluids (gas and connate water) can alter wettability and further impair the reservoir's permeability (Emiliani et al., 2005). While permeability damage is often minimal or even beneficial in tight formations, it can be substantial in high-permeability rocks (>1,000 mD), with core tests showing damage of up to 60% in cores with permeabilities of 5,000–8,000 mD (Davison et al., 2001).

Formation damage is typically quantified using the skin factor (S), as defined by the Hawkins formula:

$$S = \left(\frac{K_0}{K_d} - 1\right) \ln\left(\frac{r_d}{r_w}\right) \tag{2.3}$$

where K_0 and K_d represent the undamaged and damaged permeabilities, respectively, and r_w and r_d denote the wellbore radius and the radius of the damaged zone.

During CO_2 injection, the gas first interacts with the near-wellbore zone, which may have been altered by OBM filtrate during drilling, before it reaches the main reservoir. This highlights the importance of evaluating how OBM filtrate affects CO_2 hydrate formation under such near-wellbore conditions. While conventional hydrocarbon wells often undergo clean-up or backflow operations to remove drilling-induced damage, such procedures are generally impractical for CO_2 injection in saline aquifers or depleted fields (Byrne, Gilbert, and Anderson, 2024). As a result, direct injection following well completion is commonly applied in CCS operations (Byrne, Gilbert, and Anderson, 2024).

Hydrate formation predominantly occurs in the near-wellbore region, where conditions are susceptible to the effects of mud-filtrate invasion. This area is also the most vulnerable to formation damage, particularly in the form of reduced permeability. Such damage can alter local pressure and temperature conditions during CO_2 injection. Furthermore, if CO_2 hydrate forms in this region, it may introduce additional formation damage, further influencing the pressure–temperature behavior. As described in section 2.4, this pressure-temperature change can influence the dynamics cycle of hydrate formation and dissociation in the near-wellbore, which potentially impacts the CO_2 injectivity.

2.6. Impact of Salt, Oil, Surfactant, and W/O Emulsion on CO_2 Hydrate Formation

The following section provides a focused review of the influence of key OBM components, such as brine/salt, oil, surfactant, and emulsion, on CO_2 hydrate formation.

2.6.1. Impact of Salt on CO_2 Hydrate Formation

Salinity is a critical factor influencing the thermodynamic and kinetic behavior of CO_2 hydrate formation in porous media. When salts such as NaCl or $CaCl_2$ are present in formation brines, they dissociate into ions and interact with water molecules, reducing water activity and disrupting the hydrogen bonding

network essential for hydrate cage formation. This mechanism makes salts function as thermodynamic hydrate inhibitors (THIs). The effectiveness of this inhibition depends on the type and concentration of the salt. In general, $CaCl_2$ exhibits a stronger inhibitory effect than NaCl due to its divalent calcium ions, which have higher charge density and stronger interactions with water molecules, resulting in a more substantial reduction in hydrate formation temperature, especially at low temperatures. (Mahnaz Aghajanloo, Lifei Yan, et al., 2024; M. Aghajanloo et al., 2024)

Simulation results have confirmed that increasing salt concentrations shifts the CO_2 hydrate phase boundary, leading to decreased hydrate formation temperatures and pressures as presented in Figure 2.4 (M. Aghajanloo et al., 2024). Based on experiment conducted by Esfahani (2023), the inhibitory effect is more pronounced with $CaCl_2$, which not only delays hydrate nucleation but also causes less permeability reduction compared to NaCl. Moreover, $CaCl_2$ is fully compatible with inhibitors like MEG and methanol and does not precipitate easily, unlike NaCl, which tends to crystallize under certain conditions (Esfahani, 2023).

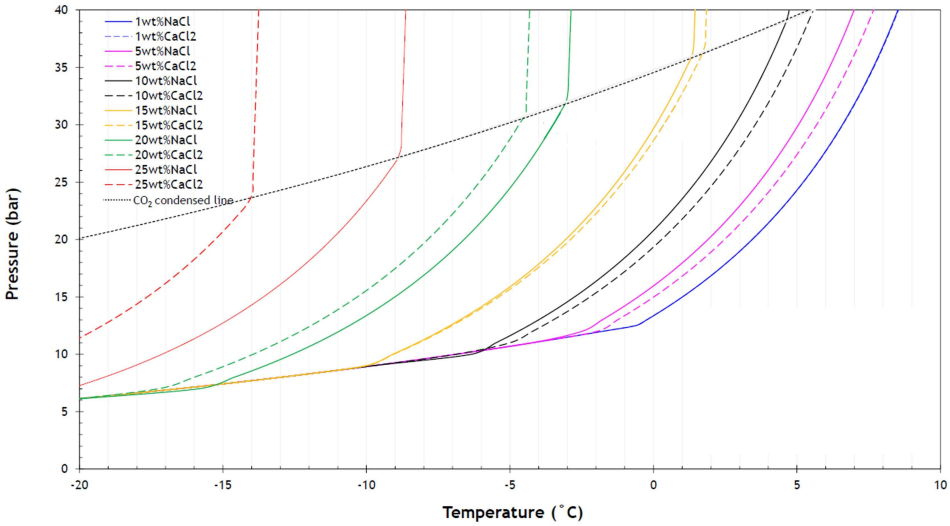

Figure 2.4: CO_2 hydrate pressure-temperature boundary diagram as the presence of NaCl and $CaCl_2$ (adapted from (M. Aghajanloo et al., 2024)).

Experimental findings also show that hydrate morphology, induction time, and permeability damage vary depending on the salt type. For instance, $CaCl_2$ extends the induction time and causes less permeability damage than NaCl due to its higher solubility and lower tendency to precipitate (Esfahani, 2023; M. Aghajanloo et al., 2024). Additionally, increasing mean water activity, regardless of salt type, slightly decreases hydrate saturation and reduces the normalized permeability impairment (Mahnaz Aghajanloo, Lifei Yan, et al., 2024).

2.6.2. Impact of Oil on CO_2 Hydrate Formation

The formation behavior of CO_2 hydrates in the presence of oil and its components has been extensively studied through experimental setups such as high-pressure visual autoclaves, stirred tank reactors, and isochoric stepwise heating methods. These studies examine the role of various types of oil, such as gas condensates, paraffinic and heavy crudes, waxes, asphaltenes, and long-chain alkanes such as *n*-dodecane and *n*-tetradecane in hydrate nucleation and growth. However, all of these studies were conducted in bulk systems. No literature has been found reporting experimental investigations on the impact of oil and its components on CO_2 hydrate formation in porous media.

The results indicate that oil can act either as a hydrate formation promoter or inhibitor, depending on its composition and concentration. Lighter components such as gas condensates and *n*-dodecane promote hydrate formation by increasing CO_2 solubility and expanding the gas–liquid interfacial area, thereby reducing induction time and enhancing CO_2 uptake (Sandoval, 2019; W. Dai, 2022). In contrast, heavier fractions like asphaltenes and waxes tend to inhibit hydrate formation. Asphaltenes, as observed by Zhang et al. (2021), delay nucleation by adsorbing at the oil–water interface and disrupting

the hydrogen bonding required for hydrate cage formation, while waxes hinder gas diffusion and thermal transport. Interestingly, flocculated asphaltenes under certain conditions may modify interfacial characteristics in a way that promotes hydrate formation (Sinquin, 2001).

M.-L. Dai et al. (2020) provided thermodynamic insights using a stepwise heating method under constant volume conditions to evaluate CO_2–*n*-dodecane–water systems at different oil mass fractions (0.33–0.60) as presented in Figure 2.5. Their results showed that the addition of *n*-dodecane had little influence on hydrate equilibrium conditions at lower pressures. However, at higher pressures, small additions of *n*-dodecane promoted hydrate formation at higher temperatures. In contrast, excessive *n*-dodecane concentrations shifted the phase equilibrium to lower temperatures, thereby inhibiting CO_2 hydrate formation rather than promoting it.

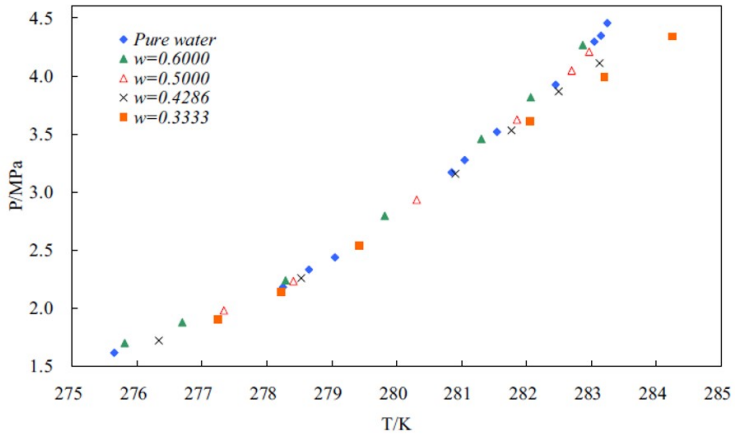

Figure 2.5: CO_2 hydrate equibrium condition in the presence of n-dodecane. w is the mass fraction of n-dodecane in the water + n-dodecane liquid phase (M.-L. Dai et al., 2020).

2.6.3. Impact of Surfactant on CO_2 Hydrate Formation

Surfactants have been widely studied for their ability to influence gas hydrate formation, particularly for CO_2 and other guest molecules. Some surfactants have been observed to enhance hydrate formation kinetics, but other surfactants have no influence on improving hydrate formation, and the mechanism by which surfactants promote hydrate formation is not well understood (Song and Z. Sun, 2022).

Kumar et al. (2015) found that among the types of surfactants, the anionic surfactants were the most effective in promoting hydrate formation by reducing induction time and enhancing nucleation and growth rates. The proposed mechanisms include enhanced gas solubility, lowered interfacial tension improving gas–water contact, and altered hydrate morphology that enables continuous capillary-driven water supply to the hydrate interface. However, the promoting effect of surfactants is highly system-dependent, and their influence varies with gas type, liquid medium, and reactor configuration.

M. Li et al. (2018) conducted an experimental study to investigate the effect of Span80 (sorbitan monooleate), a typical anti-agglomerant, on the interaction between cyclopentane (CyC5) hydrate particles and water droplets using a micromechanical force (MMF) apparatus. Span80 was dissolved in the CyC5 phase at concentrations ranging from 0.01 wt% to 1 wt%, and experiments were performed at two temperatures: 1.5°C and 7°C. The results showed that Span80 generally stabilizes the droplet–hydrate interface, thereby inhibiting hydrate agglomeration. However, when the water droplet interface failed, the interaction behavior became temperature-dependent. At 1.5°C, the water droplet spontaneously spread over the hydrate surface due to a significant reduction in interfacial tension, resulting in rapid hydrate formation and promoting agglomeration. Under these conditions, Span80 reduced the time required to separate the droplet from the hydrate particle, inadvertently accelerating contact. In contrast, at 7°C, capillary bridging dominated the interaction behavior. The presence of Span80 effectively reduced the capillary force by lowering the water–CyC5 interfacial tension, thereby enhancing its anti-agglomeration performance. This study highlights that while Span80 can act as an effective hydrate anti-agglomerant, its performance is highly sensitive to temperature and interfacial force dynamics.

Recent studies add nuance to this understanding. Song and Z. Sun (2022) reported that anionic surfactants had no clear promoting effect on cyclopentene hydrate formation, whereas nonionic surfactants like Tween80 and AEO-9 showed measurable enhancement. Lv et al. (2022) emphasized the role of the hydrophile–lipophile balance (HLB) of surfactants: surfactants with HLB values between 4.3 and 9.2 inhibited hydrate nucleation, while those with HLB > 10.2 promoted hydrate formation. These findings suggest that beyond the ionic type, the molecular structure and HLB value of surfactants play a critical role in determining whether they act as promoters or inhibitors in CO_2 hydrate systems.

2.6.4. CO_2 Solubility and CO_2 Hydrate Formation in the Presence of Emulsion

Understanding CO_2 behavior in emulsified systems is essential for evaluating its implications in hydrate formation. Recent studies have highlighted how CO_2 solubility, phase dispersion, and interfacial dynamics in the emulsion system influence hydrate formation kinetics and emulsion stability.

In the hydrate study by Galfré et al. (2011), the use of cyclopentane-water emulsions demonstrates that CO_2 hydrate formation is enhanced in emulsified systems. Cyclopentane acts as a thermodynamic and kinetic promoter, significantly lowering the hydrate formation pressure and reducing induction time when dispersed as emulsion droplets. The emulsion provides a high interfacial area and facilitates CO_2 transport to the water phase, where hydrate nucleation occurs. This emphasizes the crucial role of phase dispersion and droplet size in hydrate kinetics.

The work by Hu, Trusler, and Crawshaw (2017) highlights the rheological changes in heavy oil/water emulsions upon CO_2 dissolution. Dissolved CO_2 lowers the viscosity of the continuous oil phase and alters emulsion flow behavior by increasing the critical shear rate at which phase inversion occurs. At high CO_2 pressures, the emulsion demonstrates a viscosity drop and potential inversion from W/O to O/W structure. These findings suggest that CO_2 alters both the bulk and interfacial properties of emulsions, potentially compromising emulsion stability under dynamic conditions.

Similarly, G. Sun et al. (2018) reveal that CO_2 dissolved in crude oil weakens the viscoelastic interfacial film formed by asphaltenes and resins, reducing emulsion stability. CO_2 causes destabilization of asphaltenes and alters the pH of the water phase, diminishing the interfacial elasticity. This facilitates droplet coalescence and water separation in water-in-oil (W/O) emulsions. The study combines interfacial viscoelasticity measurements and water separation tests to confirm that CO_2 is a destabilizing agent in crude oil emulsions, particularly at higher pressures.

X. Sun et al. (2022) investigates CO_2 solubility in water-based (WBM) and oil-based drilling fluids (OBM), demonstrating that CO_2 has significantly higher solubility in OBM than in WBM. This is attributed to the non-polar nature of oil, which aligns with the physicochemical properties of CO_2. Electrolytes and polymers in WBM reduce CO_2 solubility through salting-out and molecular crowding effects. Their experimental data and predictive models show a consistent increase in solubility with pressure and a decrease with temperature.

Taken together, these studies show that while CO_2 is highly soluble in the oil phase of W/O emulsions, its presence poses a dual effect: it disrupts emulsion stability and simultaneously enhances the conditions for CO_2 hydrate formation. The high solubility of CO_2 in oil enables rapid diffusion into dispersed water droplets, increasing local CO_2 concentration and promoting hydrate nucleation. However, this dissolution leads to the softening of interfacial films and lower droplet resistance to coalescence. Thus, CO_2 solubility in W/O emulsions plays a critical role in both destabilizing the emulsion microstructure and accelerating hydrate growth due to increased interfacial mass transfer and thermodynamic favorability.

2.7. Coupled Wellbore-Reservoir Simulations

As described in the section 2.4, the impact of pressure and temperature (PT) in the wellbore is crucial for the dynamic CO_2 hydrate formation and dissociation process. As the formation damage impact the permeability in the wellbore which impact to the PT change in the wellbore, simulating the impact of formation damage is essential. Furthermore, as the hydrate formation also introduce an additional damage, it will also impact on PT behaviour in the near-wellbore.

To evaluate the impact of formation damage on pressure and temperature in the near-wellbore region,

a coupled wellbore–reservoir simulation is essential. Neglecting wellbore processes in CCS operations can lead to inaccurate predictions of bottomhole pressure and temperature, as well as an oversimplified representation of wellbore–reservoir interactions, which compromises the reliability of numerical simulations (Moslehi and D. Voskov, 2025). In particular, for cold CO_2 injection into depleted hydrocarbon reservoirs, using the tubing head temperature as a proxy for bottomhole temperature is misleading, since CO_2 experiences both heating from the geothermal gradient and cooling due to expansion (Joule–Thomson effect) along the wellbore (Moslehi and D. Voskov, 2025). Integrating the wellbore with the reservoir model allows these thermal and pressure dynamics to be captured more accurately, thus improving model fidelity and operational predictions (Nimwegen et al., 2023; Estrada, 2023).

In the coupled simulations, the reservoir model often functions as a plug-in to the wellbore model, with the latter governing the overall simulation and providing boundary conditions, while the reservoir model calculates the resulting flow rate, whether for injection or production scenarios (Estrada, 2023). Accurate reservoir characterisation is crucial for predicting CO_2 plume propagation, but injection conditions themselves, particularly injection rate and temperature, directly influence CO_2 phase behavior in the wellbore (Strpić, 2022). The pressure differential between the wellhead and the incoming CO_2, as well as between the bottomhole and the reservoir, serves as a key driver of injection performance. Therefore, a reliable simulation of CO_2 injection processes must also account for transient wellbore flow conditions to provide a complete understanding of the CCS system and to optimize injection strategies (Wan et al., 2021).

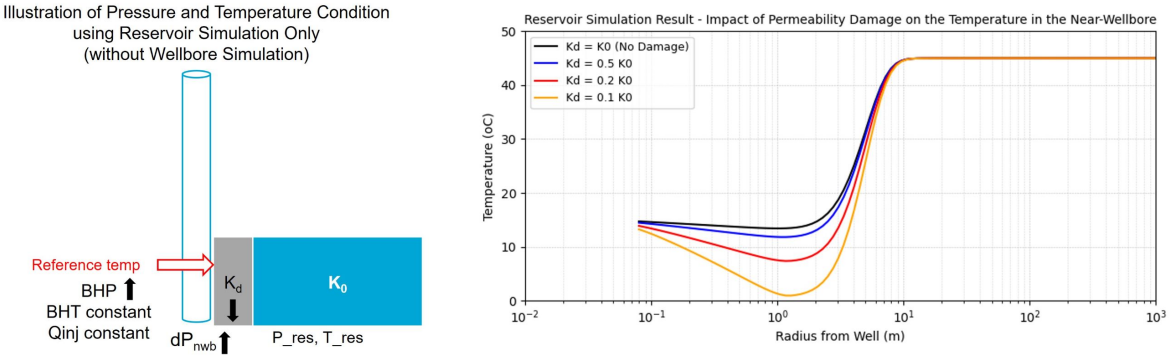

Figure 2.6: Left figure : illustration of pressure and temperature condition using reservoir simulation only (without wellbore simulation). Right figure : reservoir simulation result examining impact of permeability damage on the temperature in the near-wellbore.

Figure 2.6 shows the result of a simulation that uses only a reservoir model, without coupling to a wellbore simulation. The simulation was conducted using CMG GEM, with reservoir parameters adapted from Curtis M. Oldenburg (2007), as detailed in the Appendix A. The near-wellbore permeability (K_d) was varied from $K_d = K_0$ (without any damage) to lower values representing formation damage ($K_d = 0.5K_0, 0.2K_0, 0.1K_0$), where K_0 is the initial reservoir permeability. The results indicate that cooling effects become more pronounced as near-wellbore permeability decreases. This is because, under the reservoir simulation setup, the bottomhole injection temperature (BHT) is held constant across all permeability values. To maintain a constant injection rate (Q_{inj}) at lower K_d, a greater pressure difference (dP_{nwb}) between the bottomhole and reservoir is required, which increases bottomhole pressure (BHP). A higher dP_{nwb} enhances Joule–Thomson (JT) cooling, resulting in greater temperature reduction near the wellbore.

However, using only a reservoir simulation approach is inadequate, since in real field operations, both injection pressure and temperature are controlled at the wellhead. During injection, bottomhole temperature can vary, and under low-permeability conditions, it would typically be higher due to increased pressure drop in the near-wellbore region. Therefore, a coupled wellbore–reservoir simulation is necessary for more accurate modelling. Some commercial simulators are currently developing such coupling methods, such as CMG GEM (for reservoir simulation) integrated with LedaFlow (for transient wellbore simulation). While the initial plan for this study involved using CMG GEM coupled with LedaFlow, due to time constraints and other circumstances, the simulations were instead carried out using DARTS-well, developed by TU Delft, which supports coupled wellbore–reservoir simulation.

DARTS-well is an open-source numerical model, which integrates a multi-segment, multiphase, non-isothermal wellbore model developed using the Drift-Flux Model (DFM) with the Delft Advanced Reservoir Terra Simulator (DARTS) as the reservoir simulator (Moslehi and D. Voskov, 2025). The coupled model uses the Operator-Based Linearization (OBL) approach, which efficiently manages complex physical processes while significantly reducing computational time (Khait and D. V. Voskov, 2017). This model enables the simulation of both transient phenomena during early injection and pseudo-steady-state conditions during extended injection periods. The governing equations applied for the simulations are presented in the Appendix B.

The simulator employs pressure (P) and enthalpy (H) as its primary thermodynamic variables. All thermophysical properties (such as density, viscosity, temperature, and phase fractions) are subsequently derived using appropriate equations of state. In the coupled setup, output variables from the wellbore simulation, particularly those at the bottomhole, serve as the input for the reservoir simulation. Conversely, any resulting changes in reservoir conditions are fed back into the wellbore model. This bidirectional data exchange occurs continuously at each simulation timestep, ensuring full coupling between the wellbore and reservoir domains.

3

Methodology

The study is divided into two parts. The first part of the study used micromodel experiments to examine the effects of synthetic OBM filtrate in the form of water-in-oil (W/O) emulsion composed of dodecane, $CaCl_2$-15wt% brine, and Span80 surfactant on CO_2 hydrate formation in porous media. Image analysis was conducted using a thresholding method in ImageJ software to distinguish between hydrate, water, oil, and grain. CO_2 hydrate morphology was then interpreted, and CO_2 hydrate saturation was calculated by dividing the hydrate area by the pore area of the micromodel.

The second part involved a coupled wellbore-reservoir simulation to investigate the impact of formation damage caused by mud filtrate and additional damage caused by CO_2 hydrate formation on pressure and temperature in the near-wellbore region. Formation damage was modelled by assigning reduced permeability in the near-wellbore zone. The simulated pressure and temperature profiles were then evaluated using a CO_2 hydrate phase boundary approach to assess the associated hydrate formation risk.

3.1. Micromodel Experiments

The micromodel experiments were conducted to investigate the key characteristics of hydrate formation in porous media, including hydrate morphology, hydrate saturation, and the dissociation processes within porous structures. The micromodel approach offers several advantages over conventional methods, including safer handling under high-pressure conditions, higher experimental throughput due to shorter equilibration times, and time-resolved direct visualization of phenomena (Le Goff, Lagarde, and Santanach Carreras, 2022).

Three main components were evaluated to reflect the impact of the primary constituents of OBM filtrate: base oil as the continuous phase in OBM, brine as the dispersed phase in OBM, and W/O emulsion.

- **Base Oil.** Dodecane was selected as the analogue for base oil, as it was commonly used in oil-related experiments. It had been widely referenced in CO_2 hydrate studies and served as a representative model for the oil phase.
- **Brine.** Two types of brine were used to represent different salinity levels: NaCl-1wt% for low salinity and $CaCl_2$-15wt% for high salinity. NaCl-1wt% was chosen as the base case and was assumed to represent a low salinity formation water, while $CaCl_2$-15wt% was commonly used as dispersed fluid in oil-based mud formulations (Patil et al., 2010).
- **Water-in-Oil (W/O) Emulsion.** Oil-based mud typically consisted of base oil as the continuous phase and brine as the dispersed phase, along with additives such as emulsifiers, weighting materials, filtration control agents, and viscosifiers (J. Li et al., 2022). For simplification, a W/O emulsion composed of dodecane as base oil, $CaCl_2$-15wt% as brine, and Span 80 as the emulsifier was used to represent the OBM.

Five experiments were conducted to analyze the effects of each component:

- **Experiment #1:** NaCl-1wt% brine (baseline fluid for the experiment and low salinity fluid as formation water).
- **Experiment #2:** $CaCl_2$-15wt% brine (high salinity brine as dispersed fluid in OBM).
- **Experiment #3:** NaCl-1wt% as formation water and dodecane as the base oil (representing OBM filtrate).
- **Experiment #4:** $CaCl_2$-15wt% as dispersed fluid and dodecane as the base oil in OBM. Those fluids represent the mud filtrate of the OBM
- **Experiment #5:** NaCl-1wt% as formation water and W/O emulsion as a simplified oil-based mud.

3.1.1. Fluids and Chemicals

Table 3.1 presents the information on the fluids and concentrations used in the micromodel experiments. The density values were measured using an Anton Paar density meter (DMA4100M) at a temperature of 20°C and room pressure. Table 3.2 shows the chemicals used to prepare the solutions.

Table 3.1: Type of Fluids for the Micromodel Experiments

No	Fluid	Density (g/cm^3)
1	NaCl-1wt%	1.0056
2	$CaCl_2$-15wt%	1.132
3	Dodecane + 0.05wt% Oil Red O	0.751
4	Water-in-Oil Emulsion	1.003

Table 3.2: Chemical Properties for Micromodel Experiments

Chemical	Formula	MW (g/mol)	Density (g/cm^3)	Supplier	Purity
Carbon Dioxide	CO_2	44.01	1.977	Linde Gas	99.7%
Sodium Chloride	NaCl	58.44	2.165	Fisher Scientific	99.5%
Calcium Chloride Dihydrate	$CaCl_2{\cdot}2H_2O$	147.02	1.835	Thermo Scientific	99%
Dodecane (mixture of isomers)	$C_{12}H_{26}$	170.34	0.751	Acros Organics	99%
Oil Red O	$C_{26}H_{24}N_4O$	408.49	0.838	Sigma Aldrich	99%
Sorbitan Monooleate (Span 80)	$C_{24}H_{44}O_6$	428.62	0.986	Sigma Aldrich	68.4%

For Experiments #3 and #4, dodecane was doped with 0.05wt% Oil Red O to distinguish between the oil (dodecane) and water phases for image analysis purposes. Oil Red O was selected because it is soluble in oil and insoluble in water, and it has been widely used in laboratory experiments. Interfacial tension (IFT) measurements using the pendant drop method were performed to examine the effect of Oil Red O on the IFT between dodecane and brine. The open-source ImageJ and OpenDrop software (https://github.com/jdber1/opendrop) were used to analyze the IFT values. Figure 3.1 shows that the addition of Oil Red O slightly reduced the IFT between dodecane and brine.

For Experiment #5, the W/O emulsion was prepared using dodecane, $CaCl_2$-15wt%, and Span 80. Dodecane acted as the base fluid (continuous phase), $CaCl_2$-15wt% as the dispersed phase, and Span 80 as the emulsifier. $CaCl_2$ was chosen because it is the most common salt used for the brine in OBM (*Baker Hughes Drilling Fluids Reference Manual* 2006). A concentration of 15 wt% was selected, as the typical range of $CaCl_2$ in OBM is 3–25wt% (Patil et al., 2010). Span 80 was chosen due to its solubility in oil and its widespread use in oil-based mud formulations, as reported in Numkam and Akbari (2019), Numkam and Akbari (2018), J. Sun et al. (2018), Al-Yami et al. (2018), and also in micromodel studies by Lifei Yan et al. (2023), which use 1 - 3 wt% of Span 80 during their experiments. An oil–water ratio (OWR) of 50%:50% (v/v) and 1wt% Span 80 were selected for the emulsion preparation. Additionally, 0.1wt% Oil Red O was added to the dodecane to distinguish the oil and water phases and to differentiate brine from emulsion during image analysis. The mixture was homogenized using an IKA Turrax T50 overhead mixer. The emulsion preparation steps were as follows:

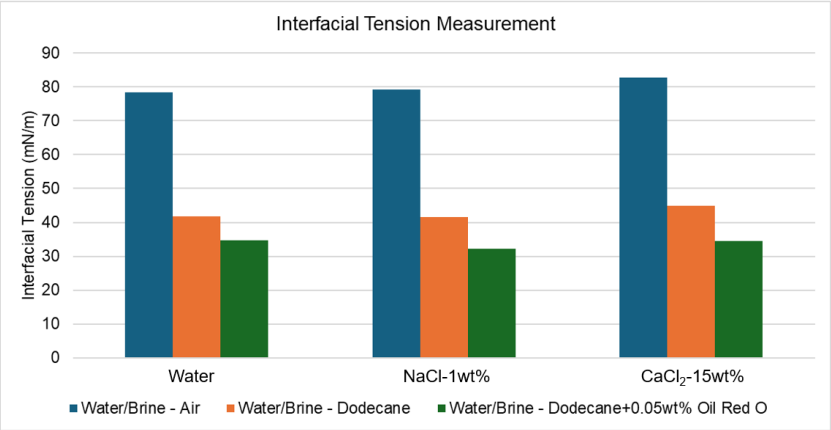

Figure 3.1: Interfacial tension measurement to check the impact of Oil Red O as oil dye

1. Placed 50 ml of dodecane into a beaker glass.
2. Added 0.1wt% Oil Red O (0.05 g) and stirred manually.
3. Added 1wt% Span 80 (1.4 g) and mixed at 3000 rpm for 2 minutes.
4. Added 50 ml of $CaCl_2$-15wt% and mixed at 5000–7000 rpm for 5 minutes.

A Modular Compact Rheometer (MCR 302) was used to measure the viscosity of the emulsion. Figure 3.2 presents the viscosity profile of the emulsion at temperatures of 25°C and 0°C. The emulsion exhibited shear-thinning behavior, as is commonly observed in OBM systems. The measured viscosity values were within a reasonable range compared to typical OBM viscosities done by Fakoya and Ahmed (2018).

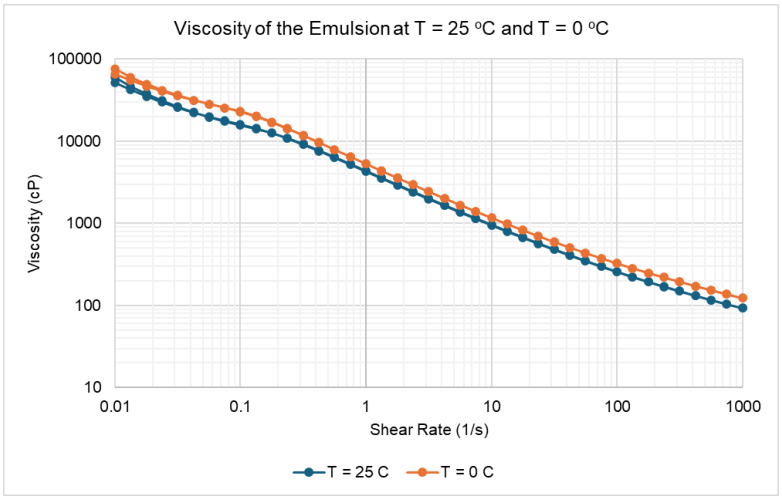

Figure 3.2: Viscosity of the emulsion at 25°C and 0°C

IFT measurements between the emulsion and NaCl-1wt% were attempted using the pendant drop method. However, the emulsion droplet adhered to the needle, making the measurements unreliable. Trials with a horizontal needle position and alternative methods (e.g., free-drop from a syringe) were also conducted, but the droplet still adhered to the needle or plastic syringe.

A simple pH sensitivity test was conducted by adding 0.1 M HCl (pH = 2) to the emulsion sample at room temperature and pressure. The result indicated that the emulsion was not sensitive to pH changes.

3.1.2. Experimental Set Up

The micromodel experiments were conducted using a Physical Rock Network Enhanced Oil Recovery (EOR.PR.20.2) chip, fabricated by Micronit Micro Technologies. The chip was constructed from borosilicate glass and fused silica and was manufactured using acid chemical etching to produce isotropic pore structures. The design and configuration of the chip used in this study followed those described by Lifei Yan (2024) and Schellart (2024), as shown in Figure 3.3.

The chip consisted of a porous medium structure with dimensions of 20 mm (length) $\times$ 10 mm (width), a pore size range from 75 µm to 675 µm, and a geometric median of 280 µm. The pore depth was 20 µm. The chip's porosity was 0.56, and its permeability was approximately 7.2 Darcy, with a pore volume of 2.24 µL. The chip exhibited a typical water-wet wettability.

Figure 3.4 shows the pore and grain structure of the chip as a binary image alongside the corresponding pore size distribution. In the image, black regions represent pore spaces, while white regions represent solid grains. The graph on the right illustrates the pore size distribution, with a fitted normal distribution represented by the solid line.

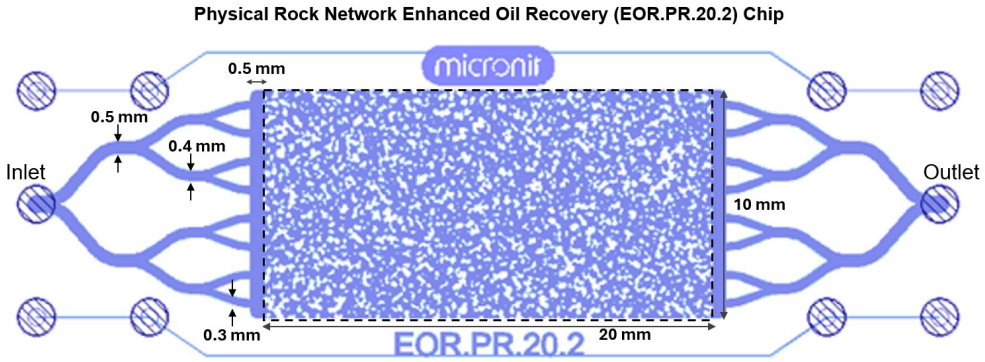

Figure 3.3: Physical Rock Network Enhanced Oil Recovery (EOR.PR.20.2) chip

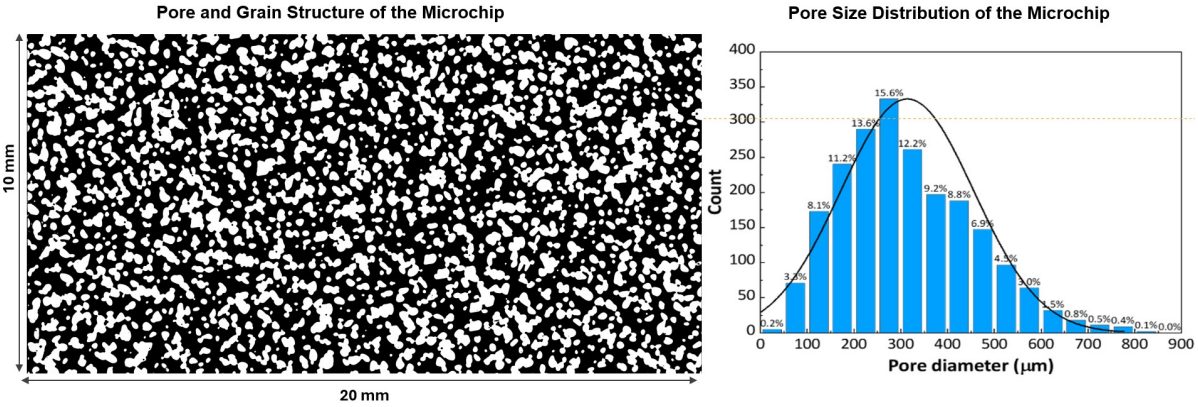

Figure 3.4: Pore and grain structure of microchip and pore size distribution (adapted from Lifei Yan (2024)).

The experimental setup was adapted from Schellart (2024) and Lifei Yan (2024). Figure 3.5 presents a schematic and a photograph of the experimental setup.

At the center of the setup, the microfluidic chip was securely mounted inside a high-pressure chip holder and enclosed within an insulated cooling box to simulate subsurface temperature conditions required for hydrate formation. The cooling box was covered with polystyrene foam for thermal insulation. The cooling system, which consisted of a cooling box and an external cooling bath, was capable of reaching temperatures as low as -12°C. Three temperature sensors were installed to monitor the ambient room temperature, cooling box temperature, and the chip surface temperature.

The microfluidic chip had two fluid connection ports. The left port was connected to a CO_2 source, while the right port was connected to a line that connected to a valve for the Quizix pump and a syringe pump.

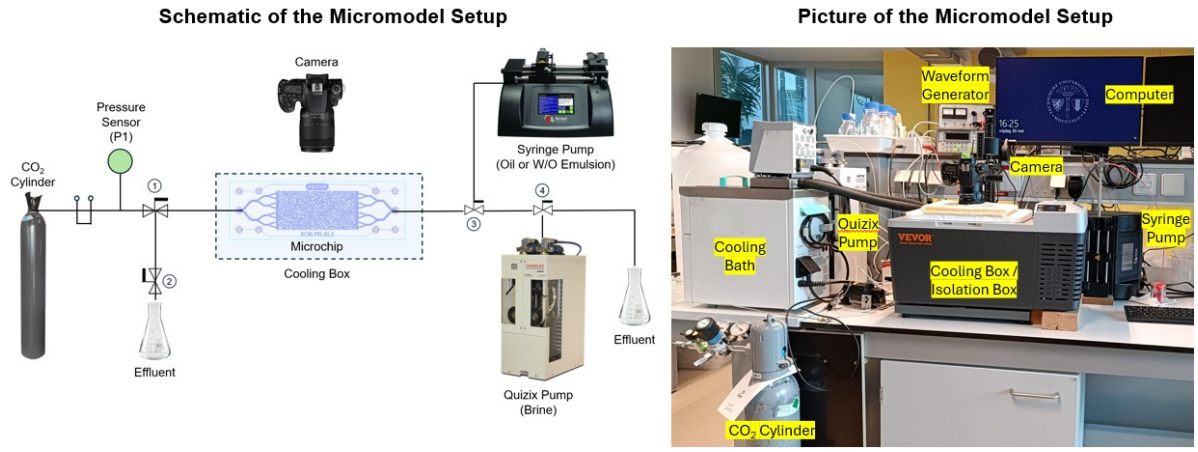

Figure 3.5: Micromodel experimental setup (modified from Lifei Yan (2024) and Schellart (2024))

The connections were made using 1/32 inch tubing. A pressure regulator was installed on the CO_2 inlet to maintain desired pressure levels, and a pressure sensor (P1) was placed to monitor pressure. Throughout this report, the pressure measured by the P1 sensor is referred to as the inlet pressure. A Chandler Quizix precision pump was used to inject brine into the chip for the brine saturation process and also to control the CO_2 flow rate via retracting mode. Outlet pressure was monitored using the sensor on the Quizix system. For experiments involving oil or emulsion (Experiments #3, #4, and #5), fluid injection was performed using a Harvard PHD Ultra syringe pump.

An electronically controlled valve was installed on valve 1, which connected one side to the injection line and the other to atmospheric pressure. This allowed for the creation of a pressure shock by instantaneously opening the system to ambient pressure at a controlled time interval using an arbitrary waveform generator.

Images were captured using a Canon EOS 90D camera equipped with an EF 100mm f/2.8L Macro IS USM lens. The camera system provided a field of view of 22.3 mm $\times$ 14.9 mm and an image resolution of 3.7 µm/pixel. The lens allowed for up to 5:1 magnification, enabling both full-chip imaging and high-resolution visualization of hydrate crystals. A light source was placed below the chip to provide transmitted illumination toward the lens.

3.1.3. Experimental Procedures

The experimental procedures were modified from the experiments conducted by Schellart (2024) and Lifei Yan (2024). The procedures were divided into three main stages: the preparation stage, hydrate formation stage, and hydrate dissociation stage, as described in the flow diagram in Figure 3.6.

Preparation Stage

a) **System Preparation**

During this initial step, all equipment, including the pump, camera, power supply, lighting, cooling system, and data acquisition software, was checked to ensure proper functionality. All necessary fluids were prepared in advance. The brine solution was degassed using a vacuum system to eliminate dissolved air. Valve 4 was set to connect the pump to the effluent line. The Quizix pump was flushed and filled by circulating the degassed brine three times through each cylinder (totaling 60 mL). The microfluidic chip was placed into the chip holder. The camera and lighting were adjusted to achieve optimal image clarity. The chip surface was cleaned using ethanol to remove any dust or fibers. Data-saving paths were set for both pressure and image acquisition. A reference image of the empty chip was taken to be used as a mask for image processing.

b) **CO_2 Leak Test**

The chip was carefully connected to the system, ensuring all fittings were tight. Valve 1 was set to connect the CO_2 line to the chip. CO_2 was introduced into the chip by gradually increasing

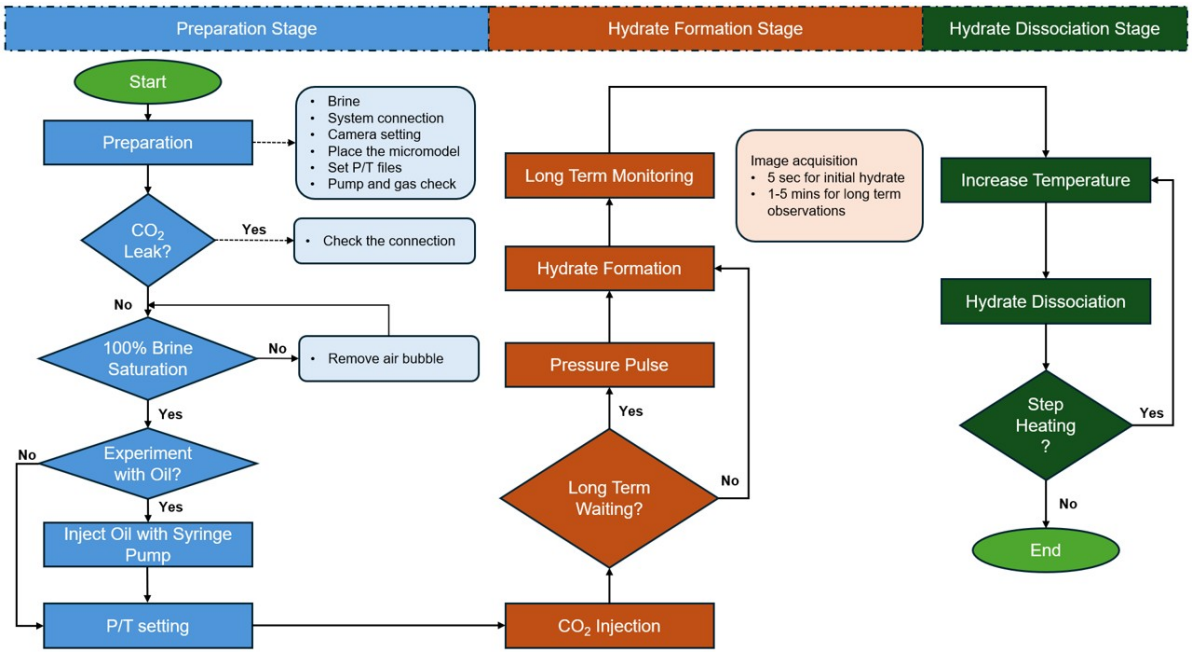

Figure 3.6: Micromodel experimental procedure (modified from (Lifei Yan, 2024))

the pressure using the regulator until the desired pressure condition was reached. The chip was submerged in a water bath to check for leaks. If bubbles were observed, the fittings were re-tightened. The system pressure was monitored for 10 minutes. If stable, the system was considered leak-free. Subsequently, the CO_2 cylinder was closed, and the system was gently depressurized.

c) **Brine Saturation**

This step aimed to replicate reservoir conditions fully saturated with water and to ensure that no air remained in the chip. Brine was injected from the right to the left side of the micromodel. Valve 3 was set to connect the Quizix pump with the chip, and Valve 1 was adjusted to connect the chip to Valve 2. Valve 2 was then opened to expose the chip to atmospheric pressure. Brine was injected using the Quizix pump while the chip was monitored via the camera. Once fully saturated, an image of the chip was captured and saved as the mask for water saturation analysis.

d) **Oil/Emulsion Injection**

This step was performed only for experiments involving oil or emulsion (Experiments #3, #4, and #5). It simulated the condition in which mud or mud filtrate invaded the reservoir. Valve 3 was adjusted to connect the chip to the syringe pump. Oil or emulsion was injected at a low flow rate to ensure that a portion of the brine remained in the chip. After injection, the syringe pump was stopped, and Valve 3 was switched to reconnect the chip with the Quizix pump. For oil injection, a flow rate of 20 μL/min was used. For Experiment #5, due to the high viscosity contrast between water and emulsion, the flow rate was reduced to 1 μL/min to preserve brine presence in the chip. An additional brine injection was performed after the emulsion injection to further increase the water saturation.

e) **Pressure and Temperature Conditioning**

The system was pressurized by closing Valve 2 and gradually increasing the Quizix pump pressure to the desired experimental condition (25 bar). The cooling bath and cooling box were then switched on and maintained until the target temperature was reached and stabilized.

Hydrate Formation Stage

a) **CO_2 Injection Process**

This stage began by injecting CO_2 to displace the liquid, simulating CO_2 injection into the reservoir. The CO_2 pressure was increased to 25 bar by adjusting the pressure regulator. Valve 1 was then set to connect the CO_2 cylinder to the microfluidic chip. The injection rate was controlled using the Quizix pump in retracting mode. During this displacement process, a flow rate of 50–100 μL/min was applied to achieve even distribution across the channels while maintaining sufficient water saturation. For Experiment #5, which involved a high-viscosity emulsion, a higher displacement rate of 200 μL/min was used to effectively displace the emulsion.

During the initial stage of CO_2 injection, images were acquired every 5 seconds to observe how CO_2 displaced the brine and oil. If no significant changes were observed in the CO_2 channels, the image acquisition interval was extended to every 1–2 minutes.

b) **CO_2 Hydrate Formation Monitoring**

After the displacement step was completed, the injection rate was reduced and maintained at a constant 10 μL/min. Extended monitoring of hydrate formation was then performed. This monitoring typically lasted overnight after hydrate crystals began to form. The imaging setting for this process was 2 - 5 minutes/image. Once the hydrate formation behaviour was confirmed, the system proceeded to the dissociation stage.

c) **Applying Pressure Pulse**

Because hydrate formation is a stochastic and often slow process, spontaneous formation could require several days. To accelerate the process, disturbances such as pressure changes or enhanced CO_2–water contact were applied. If no hydrate formation was observed within 1–3 days, a pressure pulse was applied. This was done by activating the waveform generator to switch Valve 1 between the pressurized system and atmospheric pressure for a brief period (typically 0.1–1.0 seconds). This induced a sudden pressure drop, disrupting the fluid interface and potentially promoting hydrate nucleation. Because hydrate formation can occur within a short time after a pressure pulse is applied, the imaging interval for this process was set to 5 seconds per image.

Dissociation Stage

The hydrate dissociation process is generally a deterministic phenomenon. Dissociation occurs when the pressure and temperature conditions fall outside the hydrate stability zone. This can be achieved either by increasing the temperature at constant pressure or by decreasing the pressure at constant temperature.

In this experiment, dissociation was primarily conducted by gradually increasing the temperature in a stepwise manner while maintaining constant pressure, until the hydrate phase was completely dissociated. During the dissociation process, the CO_2 flow was stopped. Temperature increase was achieved by adjusting the setpoints of both the cooling bath and the cooling box. The imaging interval for the dissociation process was set to 1 minute per image.

As an exception, due to a technical issue encountered during Experiment #3, hydrate dissociation was instead achieved by decreasing the system pressure while maintaining a constant temperature.

3.1.4. Experimental Condition

The experimental conditions were designed to replicate the actual reservoir environments in a depleted state, as illustrated in Figure 3.7. A pressure of 25 bar was applied to simulate the pressure typically found in depleted reservoirs. Additionally, a subcooling temperature of 6 °C was maintained during the experiments, following the conditions adopted by M. Aghajanloo et al. (2024) and referencing You et al. (2015), which reported that a cooling of 6.4 °C was required for methane hydrate nucleation in saline pore water.

For the experiment with NaCl-1wt% (Experiment #1), the temperature was set to -1 °C. For the experiment with $CaCl_2$-15wt% (Experiment #2), the temperature was set to -7 °C. In experiments involving dodecane, which does not significantly alter hydrate thermodynamics at low pressure (25 bar) (M.-L. Dai et al., 2020), the experimental conditions followed the brine equilibrium lines. Therefore, in the NaCl-1wt% + dodecane system (Experiment #3), the temperature was also set at -1 °C; while in the $CaCl_2$-15wt% + dodecane system (Experiment #4), the temperature was set at -7 °C.

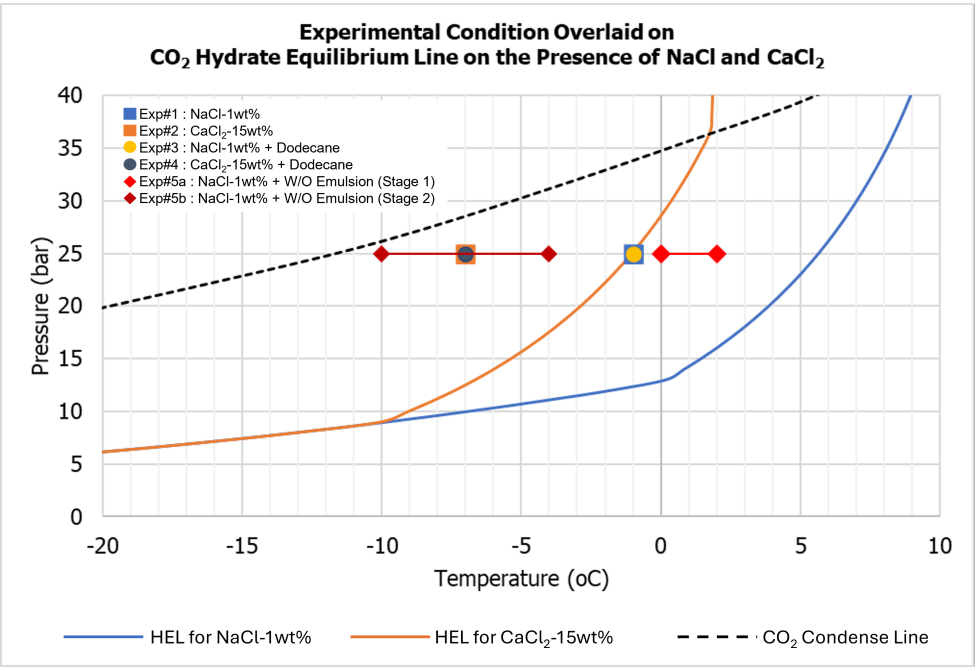

Figure 3.7: CO_2 Hydrate equilibrium line (HEL) in the presence of NaCl and $CaCl_2$ (graph adapted from M. Aghajanloo et al. (2024)). Symbols represent the experimental conditions.

For Experiment #5 (NaCl-1wt% + water-in-oil emulsion), the system contained two different brines: NaCl-1wt% (acting as the free water) and $CaCl_2$-15wt% (as the dispersed phase within the emulsion). Hence, the experiment was conducted in two distinct stages:

- First Stage
  This stage aimed to evaluate hydrate formation originating from the free water (NaCl-1wt%). The temperature was maintained between 0 and 2 °C, a range that lies within the hydrate stability zone (HSZ) for NaCl-1wt% but outside the HSZ for $CaCl_2$-15wt%. The resulting subcooling was approximately 3.6–5.6 °C.
- Second Stage
  This stage focused on hydrate formation from the dispersed water in the emulsion ($CaCl_2$-15wt%). The temperature was set to -7 °C, which corresponded to a subcooling of approximately 6 °C for the $CaCl_2$ system. However, due to technical issues during temperature control, the temperature fluctuated around -7 $\pm$ 3 °C. Despite this variation, the conditions remained within the hydrate stability zone for $CaCl_2$-15wt%, while staying above the CO_2 condensation temperature. Therefore, the conditions were still considered suitable for hydrate formation experiments. The potential impact of these temperature fluctuations was also evaluated.

3.1.5. Image Analysis and Data Processing

Figure 3.8 shows the example of micromodel images from the experiments, starting with the empty chip, followed by the brine saturation process, oil injection, and the stages during CO_2 injection and CO_2 hydrate formation. Hydrate formation's images is shown under three different conditions: (1) when only brine was present, (2) when oil was present, and (3) when a water-in-oil (W/O) emulsion was present. In the images, CO_2 hydrate could be identified by the dark or black regions in the micromodel. The oil phase appeared reddish due to the Oil Red O dye, while CO_2 was visible as a grey color. However, it was difficult to distinguish between the grain and water phases, as they appeared in similar shades. Therefore, image analysis and processing were necessary to accurately differentiate all components and phases within the micromodel.

Due to variations in complexity across different experiments, the image processing methodology was tailored accordingly for each case. In addition, because of limitations in computer RAM, only a subset of images was selected for analysis. However, the selected images were chosen carefully to ensure

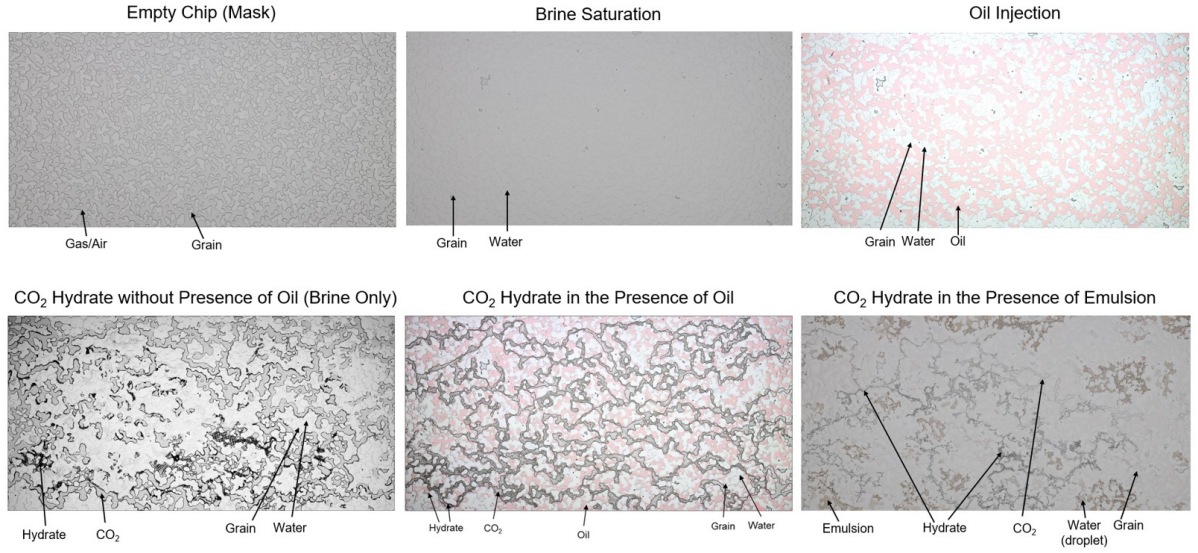

Figure 3.8: Example of images during micromodel experiments.

they were representative of the results and trends.

For the early stages of hydrate formation and the dissociation process, image analysis was conducted at intervals of approximately 3–5 minutes per frame. In contrast, for long-term hydrate monitoring, which could span overnight or several days, images were analyzed at a frequency of approximately 4 to 10 images per hour, depending on the total duration of the monitoring. The image analysis was then synchronized with pressure and temperature data measured by the P1 sensor and the Quizix pump.

Image analysis was conducted in ImageJ software using a thresholding method with programmed macros to distinguish hydrate, water, oil, and CO_2, and to interpret the morphology of the CO_2 hydrate. The saturations of hydrate, water, oil, and CO_2 were determined by calculating their respective areas and dividing by the total pore space area. Figure 3.9 shows the general image analysis procedure used to calculate hydrate saturation, modified from Schellart (2024) and Lifei Yan (2024).

- Loaded the images into ImageJ, created a stacked image set, converted the raw images to 8-bit, and aligned all images. Rotated and cropped the images to the region of interest (ROI).
- Used the *Image Calculator* function to subtract the 8-bit images with the empty chip image (mask).
- Binarized the images by applying an appropriate threshold for hydrate.
- Denoised the images using the *Remove Outliers* function to eliminate noise.
- Calculated the hydrate area in the micromodel using the *Analyze Particles* function and exported the data to an Excel file.
- The % Area calculated from ImageJ is the total area of the hydrate divided by the total area of the micromodel. Therefore, hydrate saturation is calculated by dividing the % Area by the porosity of the micromodel.

Water saturation calculation was performed using a similar procedure to hydrate saturation, but with a different threshold value. In some cases, due to variations in lighting intensity within the micromodel, the images needed to be split into several regions so that a specific threshold could be applied to each region. Subsequently, the images were merged again before calculating hydrate or water saturation.

To calculate oil saturation, the images needed to be split into their color channels before applying the thresholding method. The images were in RGB format before splitting. The *Split Channels* function was used to separate the red, green, and blue channels. The *Image Calculator* function was then used to subtract the green channel from the red channel. After that, thresholding was applied, noise was removed, and oil saturation was calculated following the same procedure as for hydrate and water saturation.

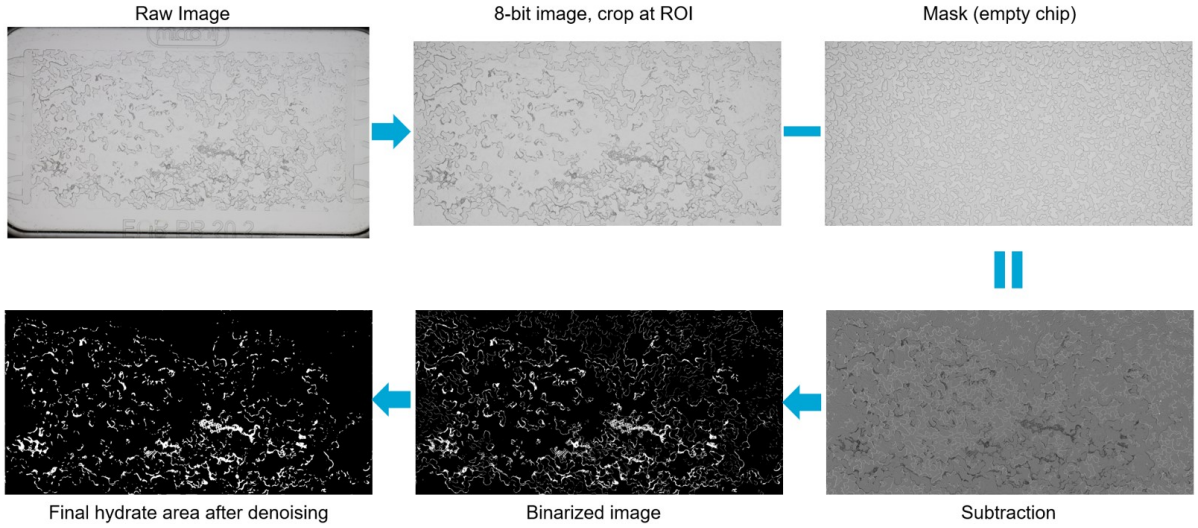

Figure 3.9: Image analysis procedure to calculate hydrate saturation

3.1.6. Water to Hydrate Conversion Factor

The conversion factor represents the percentage of water molecules that converted to hydrate. The conversion factor is calculated by total mass hydrate formation formula (Schellart, 2024) as presented in Equation 3.1.

$$m_H = S_H \cdot PV \cdot \rho_H = f_{\text{conv}} \times n_{H_2O} \left[Mw^{H_2O} + \frac{Mw^{CO_2}}{N_H} \right] \tag{3.1}$$

in this equation, m_H is the mass of the hydrate, S_H the hydrate saturation calculated from image analysis, PV the total pore volume of the micromodel, ρ_H the hydrate density (assume 0.803 g/cm^3 (Mahnaz Aghajanloo, Taghinejad, et al., 2024)), f_{conv} the conversion factor, n_{H_2O} the total number of water moles, Mw^{H_2O} the molecular weight of water (18.015 g/mol), Mw^{CO_2} the molecular weight of CO_2 (44.01 g/mol), and N_H the number of water molecules per CO_2 molecule (hydration number = 6.2 (Mahnaz Aghajanloo, Taghinejad, et al., 2024)).

The total number of water moles n_{H_2O} is defined as

$$n_{H_2O} = \frac{m_{H_2O}}{Mw^{H_2O}} = \frac{(S_w + S_H) \cdot PV \cdot \rho_w}{Mw^{H_2O}} \tag{3.2}$$

where m_{H_2O} is the mass of the water or brine, S_w the water saturation calculated from image analysis, and ρ_w the brine density (1.0056 g/cm^3 for NaCl-1wt% and 1.132 g/cm^3 for $CaCl_2$-15wt%).

By arranging Equation 3.1 and Equation 3.2 the conversion factor f_{conv} can be calculated by Equation 3.3.

$$f_{\text{conv}} = \frac{S_H \cdot \rho_H \cdot Mw^{H_2O}}{(S_w + S_H) \cdot \rho_w \cdot \left(Mw^{H_2O} + \frac{Mw^{CO_2}}{N_H} \right)} \tag{3.3}$$

3.1.7. Assumptions and Limitations

The assumptions and limitations associated with these experiments and analysis are outlined as follows:

- Since the experiment employed a single camera with a fixed focal plane, and images were captured from a top-down view of a horizontally positioned flat micromodel, a two-dimensional (2D) analysis approach was adopted. This approach assumes that fluid saturation is uniformly distributed across the vertical dimension of the chip, with no significant vertical stratification of different fluid phases. Gravitational effects were considered negligible.

- Because the inlet and outlet pressures were not directly measured at the microchip, the observed pressure differential may not be solely attributable to hydrate-induced pore clogging. It is also possible that hydrate formation or icing within the tubing lines contributed to the pressure drop. However, these phenomena could not be directly observed during the experiment, as the tubing was enclosed within a covered cooling box.

3.2. Coupled Wellbore–Reservoir Simulation

The simulation primarily investigates how permeability impairment and the radial extent of formation damage affect the reservoir's pressure and temperature in the near-wellbore region. As a baseline, a reservoir scenario without any damage is established. Subsequently, the effect of permeability damage on near-wellbore pressure and temperature is assessed by varying two key parameters: the damaged-zone permeability K_d and the radius of the damaged zone R_d. Here, K_d denotes the permeability in the invaded zone, while K_0 represents the original undamaged permeability. The radius of damage R_d defines the extent of the invaded zone influenced by the mud filtrate.

Damaged permeability values of $K_d = 0.7K_0$ and $0.4K_0$ were used to represent permeability impairment caused by drilling mud–induced formation damage. Furthermore, since the formation of CO_2 hydrate could lead to additional damage, lower values of $K_d = 0.2K_0$ and $0.1K_0$ were applied for the simulations.

Figure 3.10 provides a schematic illustration of the damage zone, highlighting both K_d and R_d.

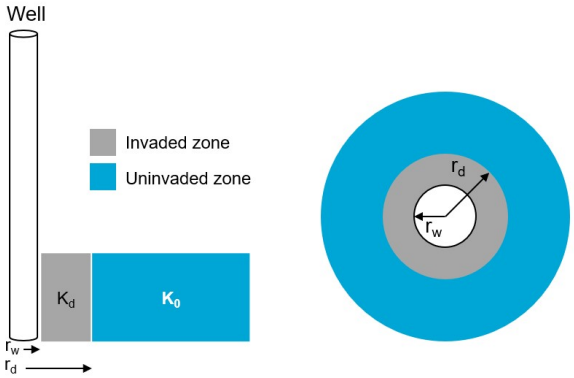

Figure 3.10: Schematic illustration of permeability damage (K_d) and radius of damage (R_d).

The simulation outputs include wellbore pressure and temperature profiles during both the transient and pseudo-steady-state stages. The influence of K_d and R_d on reservoir pressure and temperature is analyzed both across the entire reservoir and specifically within the near-wellbore zone.

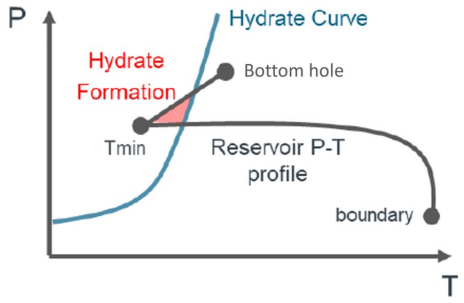

Figure 3.11: CO_2 hydrate risk analysis using the hydrate equilibrium line and reservoir pressure–temperature profile (adapted from Yamada et al. (2024)).

To assess the risk of CO_2 hydrate formation, a phase boundary analysis is conducted by comparing simulation results (pressure and temperature) at each gridblock with the hydrate equilibrium line (HEL). The HEL used in this study corresponds to CO_2 hydrate in the presence of NaCl-1wt% and $CaCl_2$-

15wt% brine, as reported by M. Aghajanloo et al. (2024). An illustration of this approach is shown in Figure 3.11.

The simulation was performed using an open-source coupled wellbore-reservoir numerical model DARTS-well, which is capable of simulating coupled-wellbore reservoir simulations for CO_2 injection in depleted reservoirs (Moslehi and D. Voskov, 2025).

3.2.1. Assumptions and Limitations

The following assumptions and limitations apply to the simulations:

1. The simulations are conducted using a single-component system (CO_2) with two phases: gas and liquid.
2. The initial conditions of both the wellbore and reservoir assume 100% gaseous CO_2.
3. The value of the permeability of the damaged zone is assumed to be constant over time.
4. The current simulation framework utilized a simple phase boundary approach and does not account for the kinetics of hydrate formation or its impact on porosity and permeability alterations.

3.2.2. Reservoir and Wellbore Model

A 1-D radial model was developed for the simulation study. The reservoir, extending 1000 meters in the radial direction, was discretized into 50 gridblocks. To capture detailed flow and thermal behavior near the wellbore, grid refinement was applied, with the innermost block measuring 0.15 meters and subsequent grid sizes increasing logarithmically, as illustrated in Figure 3.12.

The wellbore model adopted a vertical well configuration. The tubing was divided into 60 segments, each 50 meters in length, resulting in a total well length of 3,000 meters. The reservoir and wellbore parameters were set to mimic the typical CO_2 injection in depleted reservoirs, especially in the North Sea area. Table 3.3 summarises the complete set of input parameters for the reservoir and wellbore geometry.

Figure 3.12: Geometry and gridblock structure of the 1-D radial reservoir model, with refined grids near the wellbore.

Table 3.3: Reservoir and wellbore geometry

Reservoir Geometry	Grid type: 1-D radial model
	Radial grid size: 50 gridblocks; innermost block 0.15 meters with logarithmic grid spacing outward
	Thickness: 50 meters (single layer)
	Radius: 1000 meters
	Reservoir top depth: 2950 meters
Wellbore Geometry	Inclination angle: 0° (Vertical wellbore)
	Total length: 3000 meters (60 segments, each 50 meters long)
	Inner diameter: 0.125 meters
	Wall absolute roughness: 2.5×10^{-5} meters

3.2.3. Rock and Fluid Properties

The simulation scenario involves injecting pure CO_2 into a depleted dry gas reservoir. The rock and fluid properties used in this study are adapted from Moslehi and D. Voskov (2025), with several modifications to suit the objectives of this research. Table 3.4 summarizes the key properties of the reservoir and wellbore system.

3.2.4. Initial and Boundary Conditions

The reservoir is initially in a depleted state, characterized by low-pressure conditions. It is assumed to represent an infinite reservoir by applying infinitely large grid blocks at the outer radial boundary cells.

Table 3.4: Rock and fluid properties

Rock Properties	Permeability: 300 mD Porosity: 0.2 Water saturation (S_w) = Irreducible water saturation (S_{wc}) : 0 Rock compressibility: 0 bar^{-1} Rock thermal conductivity : 181.44 kJ/(m·K·day) or 2.1 W/(m·K) Rock heat capacity : 2200 kJ/m^3 or 846 J/(kg·K)
Fluid Properties	Phase behavior: Peng–Robinson Equation of State (PR-EoS) Initial reservoir and wellbore fluid composition: 100% CO_2 Injected fluid composition: Pure CO_2 CO_2 gas and liquid density: Calculated using PR-EoS CO_2 gas and liquid enthalpy: Calculated using PR-EoS CO_2 gas and liquid viscosity: Calculated using Fenghour correlation

CO_2 is injected at a constant rate of 30 kg/s, with the wellhead pressure and temperature maintained at 100 bar and 15 °C, respectively. The initial and boundary conditions used in the simulation are summarized in Table 3.5.

Table 3.5: Initial and boundary conditions

Initial Conditions	Reservoir pressure: 25 bar Reservoir temperature: 84 °C Reservoir initial fluid composition: 100% CO_2 Initial tubing head pressure: 14.7 bar Initial tubing head temperature (ambient): 10 °C
Boundary Conditions	**At wellhead:** Injection rate: 30 kg/s Injection pressure: 100 bar Injection temperature: 15 °C **At reservoir boundaries:** No-flow condition at the top and bottom boundaries Constant pressure at radial boundaries, implemented using infinitely large grid blocks (infinite reservoir assumption)

3.2.5. Simulation Setup

The simulations were conducted over a year. To replicate real startup operations, a ramp-up phase was implemented during the first four minutes to gradually reach the target injection rate of 30 kg/s. The simulation employed progressive time stepping, utilizing high-resolution timesteps during the early period to accurately capture transient behavior in the wellbore, followed by lower-resolution timesteps as the system approached the pseudo-steady-state regime. The complete simulation setup is summarized in Table 3.6.

Table 3.6: Simulation setup

Simulation Setup	Duration: 1 year Injection ramp-up period: 4 minutes Simulation timestep (ts): - t = 0 – 1 minute: ts = 0.0001 s, ts multiplier = 2, max ts = 2 s - t = 1 – 5 minutes: max ts = 5 s - t = 5 – 10 minutes: max ts = 10 s - t = 10 minutes – 1 hour: max ts = 1 minute - t = 1 hour – 1 day: max ts = 1 hour - t = 1 – 365 days: max ts = 1 hour

4

Micromodel Experiment Results

Five main microfluidic experiments were conducted as part of this thesis. Since hydrate formation is a stochastic process and its onset time is unpredictable, a pressure pulse was applied in most cases to accelerate nucleation. Almost all experiments utilized pressure pulses, except for the experiment #2 involving $CaCl_2$-15wt%, in which hydrate formation occurred naturally after approximately 13.7 hours of CO_2 injection without the need for external stimulation. Hydrate also formed spontaneously, without the application of a pressure pulse, during the second stage of Experiment #5, following the breakdown of the water-in-oil emulsion.

The results presented in this chapter focus on the primary findings from each experiment. Repeated trials conducted to support and validate these observations are documented separately in the Appendix.

4.1. Experiment #1 : Microfluidic Experiment using NaCl-1wt%

The first experiment conducted used NaCl-1wt%. This experiment was designed as the baseline for the series of experiments. In addition, it represented a low-salinity formation fluid.

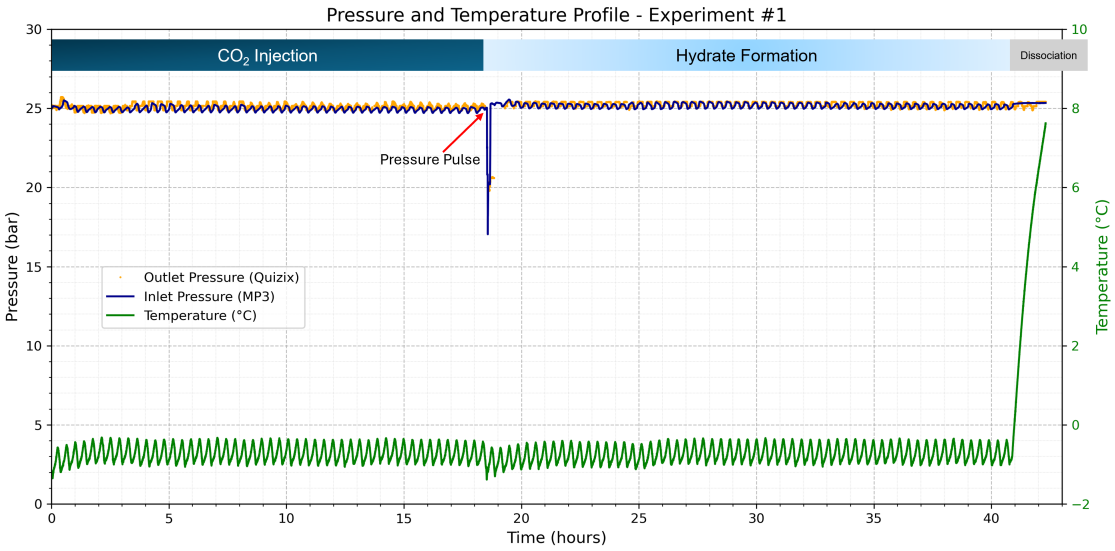

Figure 4.1: Pressure and Temperature Profile of Experiment #1.

Figure 4.1 shows the pressure and temperature profiles of the experiment over time. The experimental conditions were set at 25 bars and -1 $\pm$ 0.5°C. CO_2 was injected at a constant rate of 10 μL/min. After 18.5 hours of injection, no hydrate formation was observed. Subsequently, a 0.3-second pressure

pulse was applied to accelerate the hydrate formation process. Following the pulse, hydrate formation occurred rapidly. The initial hydrate appeared in the inlet area of the micromodel, followed by progressive formation within the pore spaces throughout the micromodel.

At time 18.5 hours, shortly after the pressure pulse was applied and the hydrate formed, a significant pressure drop was observed, followed by a return to the initial pressure of 25 bars. The pressure in the Quizix pump also decreased to 20 bars and subsequently increased gradually back to 25 bars. This behavior was likely caused by a partial blockage at the inlet tubing of the micromodel.

After 22 hours of hydrate formation observation, the dissociation stage was initiated by gradually increasing the temperature from -1°C to 7°C.

Figure 4.2 shows micromodel images captured at various stages of the experiment, starting from the application of the pressure pulse, followed by the initial hydrate formation in the micromodel, the hydrate growth observed after 22 hours of experimentation (prior to dissociation), and finally the hydrate dissociation phase.

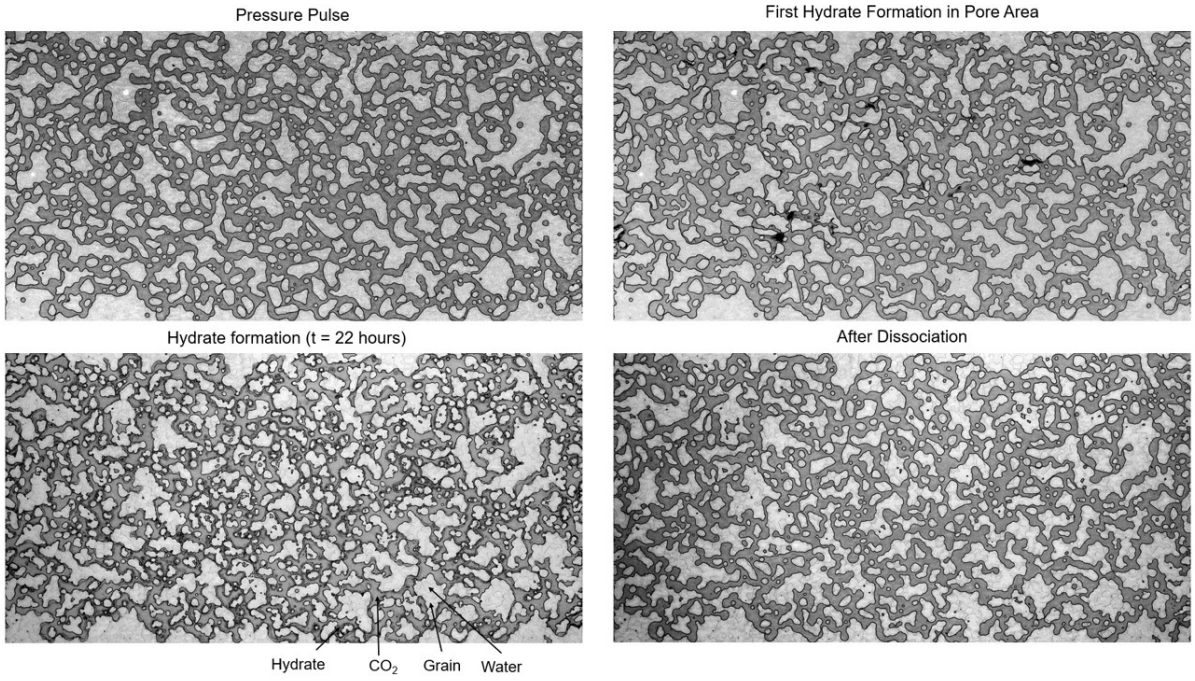

Figure 4.2: Micromodel images captured at various stages of the experiment.

The hydrate morphology and hydrate saturation during the formation and dissociation phases are described in the following sections. For the image analysis, a total of 145 images were selected to evaluate hydrate and water saturation profiles. During the first hour, images were analyzed at a frequency of 6-minute intervals. For long-term hydrate monitoring, images were analyzed at 12-minute intervals, and during the dissociation phase, image analysis was conducted at 3-minute intervals.

4.1.1. Hydrate Morphology

Figure 4.3a shows a representative image from the micromodel during the experiment. In the image, black regions indicate hydrate, while gray regions represent CO_2. The water and grain phases appear in similar white tones but are separated by dark interface lines, which delineate the boundaries between water and grain surfaces.

To enable clearer identification of each phase, image segmentation was performed in ImageJ by setting a different colour for each phase after thresholding was applied, as shown in Figure 4.3b. The segmentation allows for clear visualization of hydrate, water, CO_2, and grain distribution within the micromodel. Hydrate formation in this experiment predominantly occurred near the grain surfaces, eventually surrounding the solid grain structures. This morphology is characteristic of grain-coating hydrate, as schematically illustrated in Figure 4.3c.

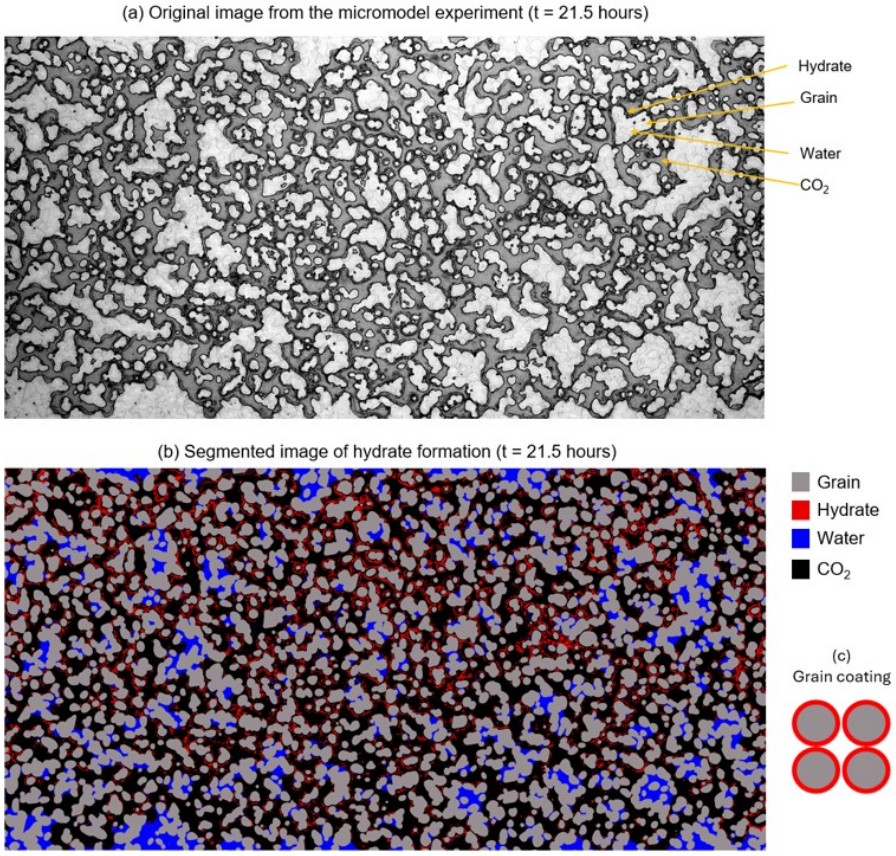

Figure 4.3: (a) Original image from the micromodel experiment; (b) segmented image showing the distribution of grain, hydrate, water, and CO_2 phases; (c) schematic illustration of grain-coating hydrate morphology.

4.1.2. Hydrate Formation

Figure 4.4 shows the profiles of hydrate and water saturation after the application of a pressure pulse. The time reference on the graph begins at the moment the pressure pulse was applied. Due to fluctuations in lighting intensity during the experiment, a smoothed version of the hydrate saturation curve was generated to highlight the trend, with verification conducted using the original raw images to ensure accuracy.

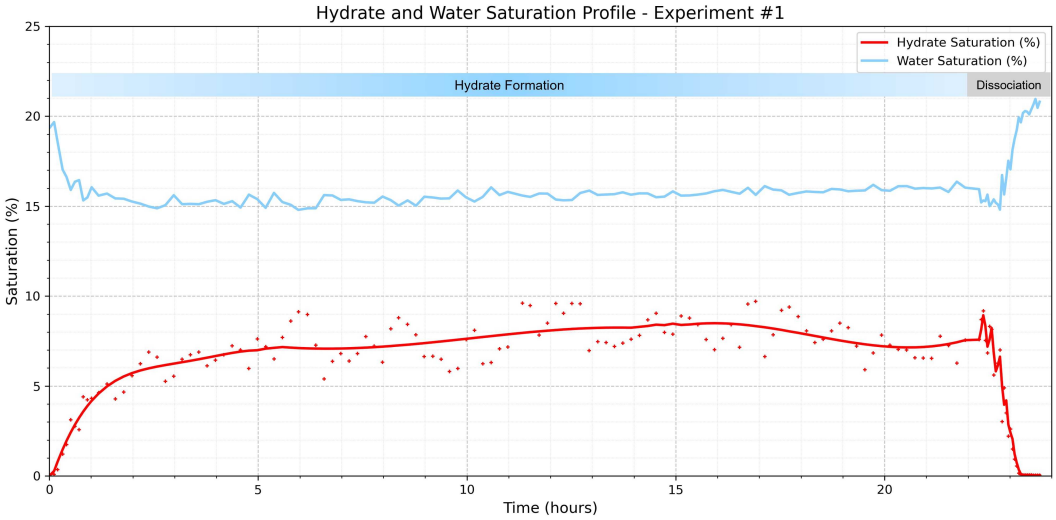

Figure 4.4: Hydrate and water saturation profiles during hydrate formation and dissociation in Experiment #1 (NaCl-1wt%).

Following the pressure pulse, the initial water saturation was approximately 20%. Hydrate formation began immediately after the pulse. During the first 1.5 hours, hydrate growth was rapid, with hydrate saturation exceeding 5%. During this period, water saturation also decreased significantly to around 15%, indicating the conversion of water into hydrate.

After the initial 1.5 hours, hydrate formation continued at a slower rate, stabilizing at a saturation level of approximately 7–8%. Meanwhile, water saturation remained relatively stable at around 15–16%. This behavior may be attributed to increased CO_2 consumption as hydrate formation progressed. When hydrate dissociation occurred, the hydrate converted back into water, resulting in a rise in water saturation to around 20%.

The conversion factor during this experiment was approximately 18 - 20 %.

4.1.3. Dissociation Process

Figure 4.5 highlights the hydrate and water saturation profiles during the dissociation process. The dissociation phase began after approximately 22 hours of hydrate formation observation. Dissociation was initiated by gradually increasing the system temperature until the hydrate was fully dissociated.

The onset of dissociation was identified by a significant decrease in hydrate saturation and a corresponding increase in water saturation. At t = 22.75 hours, a sharp decline in hydrate saturation was observed, accompanied by a sudden rise in water saturation. This behavior indicates that dissociation started at a temperature of approximately 3°C. While the hydrate was fully dissociated at a temperature of 5.8 °C.

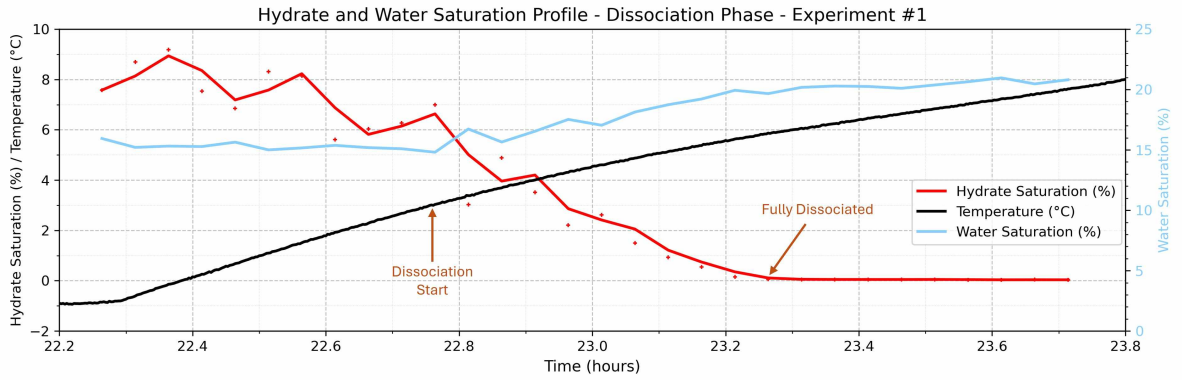

Figure 4.5: Hydrate and water saturation profiles during the dissociation phase in Experiment #1. The onset of dissociation occurred at approximately 3°C.

4.2. Experiment #2: Microfluidic Experiment using $CaCl_2$-15wt%

The second experiment was conducted using $CaCl_2$-15wt% brine. This experiment was designed to simulate the influence of high-salinity brine, which is commonly used as dispersed fluid in oil-based mud and may represent one type of mud-filtrate present in the near-wellbore region.

Figure 4.6 shows the pressure and temperature profiles recorded throughout the experiment. The experimental conditions were maintained at 25 bars and -7.3 $\pm$ 0.3°C. CO_2 was injected at a constant rate of 10 μL/min. The initial water saturation in the micromodel was approximately 48%. After 13.7 hours of continuous CO_2 injection, hydrate formation in the micromodel was observed. Following 30 hours of hydrate formation monitoring, the dissociation phase was initiated by gradually increasing the temperature in a stepwise manner from -7.3°C to 7°C.

A decrease in outlet pressure was observed before the onset of hydrate formation in the micromodel. This condition may have been caused by a partial blockage in the outlet tubing of the micromodel. After hydrate formation occurred, a decrease in outlet pressure happened over a longer duration, which may have been caused by hydrate accumulation both within the micromodel and in the downstream tubing.

Figure 4.7 shows micromodel images captured at various stages of the experiment, starting from the

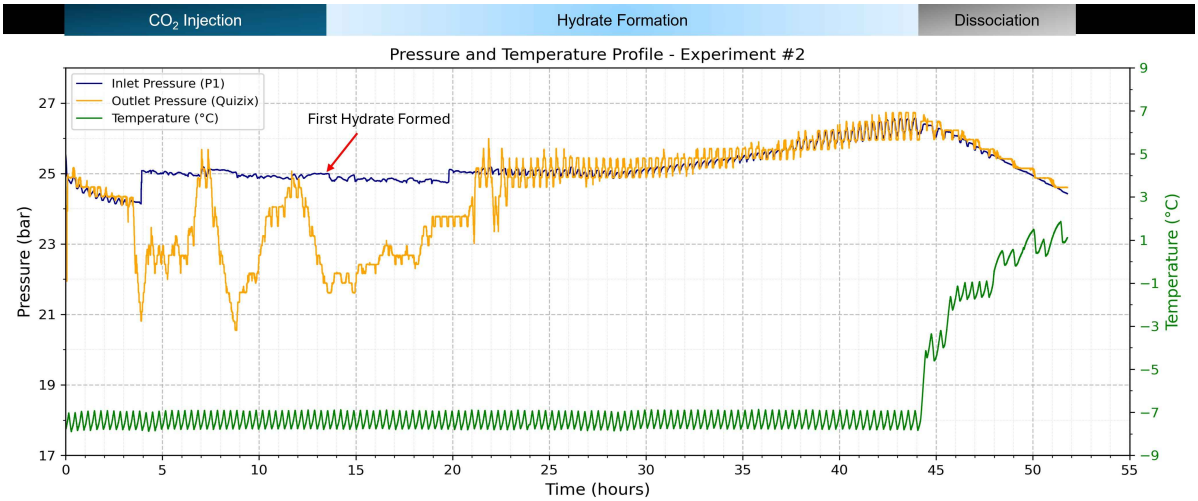

Figure 4.6: Pressure and temperature profiles of Experiment #2.

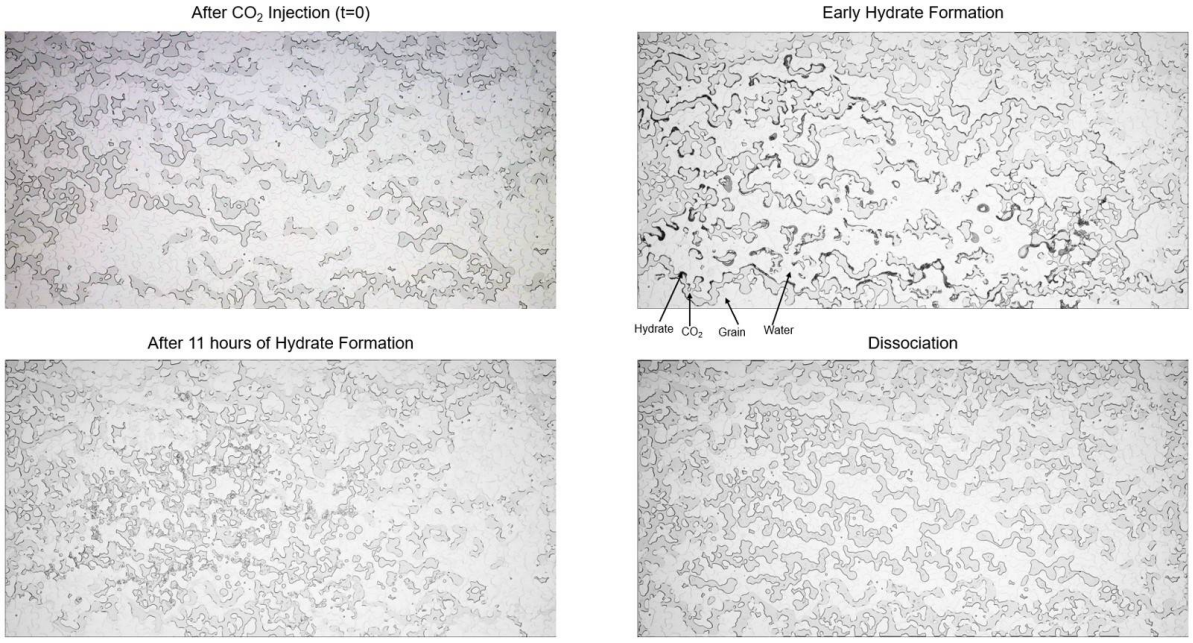

Figure 4.7: Micromodel images captured at various stages of Experiment #2.

CO_2 injection process, followed by the early hydrate formation in the micromodel, the hydrate growth observed after 11 hours of hydrate formation, and finally the hydrate dissociation phase.

The detailed analysis of hydrate saturation profile and associated morphological characteristics will be presented in the following section. Subsequently, the dissociation process will be discussed, with a focus on evaluating the hydrate dissociation temperature during the experiment. For the image analysis, a total of 223 images were selected to evaluate hydrate saturation profiles. During the first six hours, images were analyzed at 5-minute intervals. For long-term hydrate monitoring, images were analyzed at 20-minute intervals, while during the dissociation phase, image analysis was conducted at 6-minute intervals.

4.2.1. Hydrate Formation

Figure 4.8 shows the profiles of hydrate saturation, pressure, and temperature during hydrate formation and dissociation. The letters a–f in Figure 4.8 correspond to the timestamps of six key images used to

analyze hydrate behavior, as visualized in Figure 4.9.

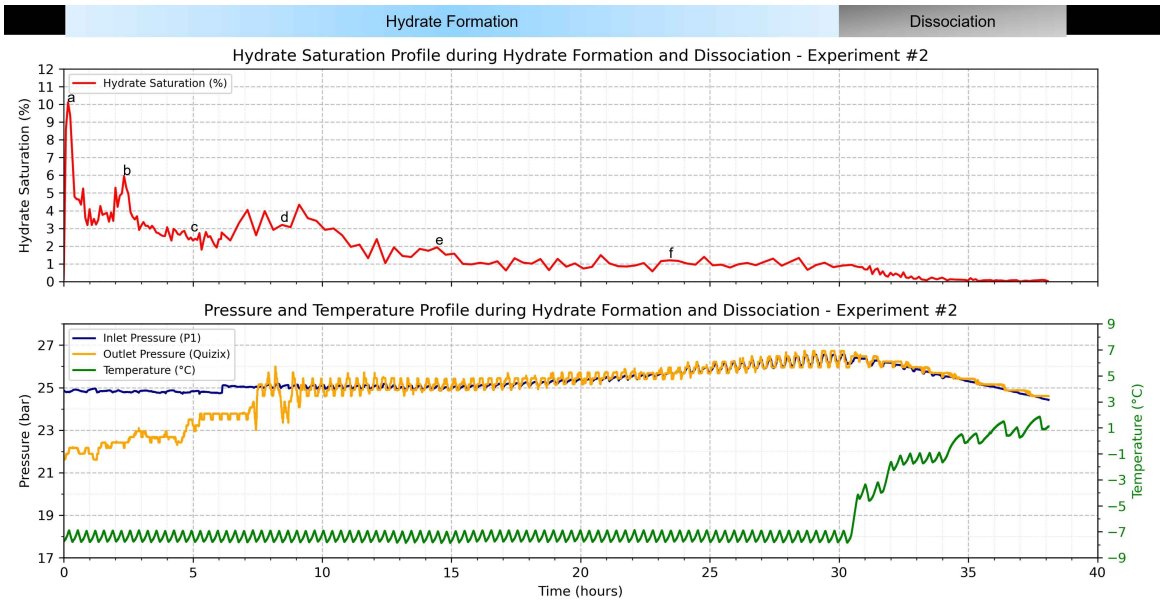

Figure 4.8: Hydrate saturation, pressure, and temperature profiles during hydrate formation and dissociation in Experiment #2.

At t = 10 minutes, hydrate formation was detected with a notably high initial saturation of 10.1%. This was followed by a rapid decline in saturation to approximately 3% within the first hour. Subsequently, the hydrate saturation increased again, reaching 6% at t = 2.3 hours, before gradually decreasing to between 2–3% by t = 10 hours. After approximately 15 hours, hydrate saturation stabilized at around 1%. The conversion factor during this experiment was approximately 1.4 - 11.5%.

Corresponding changes in outlet pressure mirrored the dynamic fluctuation in hydrate saturation. Decreases in hydrate saturation were often accompanied by increases in outlet pressure, suggesting a correlation between hydrate blockage in the micromodel and pressure drop across the system. However, it is worth noting that the pressure drop might not only be caused by the hydrate clogging in the micromodel, but also by hydrate blockage in the tubing line of the system, which could not be visibly observed during the experiment.

Figure 4.9 illustrates changes in both the location and saturation of hydrate over time. In the images, black regions represent hydrate, while gray regions correspond to CO_2. The water and grain phases appear in similar white tones but are separated by distinct interface lines that delineate water–grain boundaries. These images demonstrate that hydrate can continuously form and dissociate even during the formation phase. Moreover, the spatial distribution of hydrate was observed to change significantly over time, indicating a dynamic and localized growth behavior.

To further analyze this phenomenon, the images were segmented into five distinct areas to investigate local variations in hydrate and water saturation during the formation process, as shown in Figure 4.10. The corresponding local saturation profiles of hydrate and water for each area are presented in Figure 4.11.

The left-hand graph in Figure 4.11 illustrates the proportion of local hydrate saturation in five different areas of the micromodel over time, along with the corresponding trend in total hydrate saturation. The right-hand graph presents the proportion of water saturation in each area, together with the total water saturation trend.

Initially, before the hydrate formed, water saturation in the system was approximately 48%. During the early stage of hydrate formation (t = 10 minutes), the total hydrate saturation reached 10%, with most of the hydrate concentrated in areas 3 and 4, while area 5 contained less hydrate. Meanwhile, the water saturation was around 35%, with most of the water distributed in area 5.

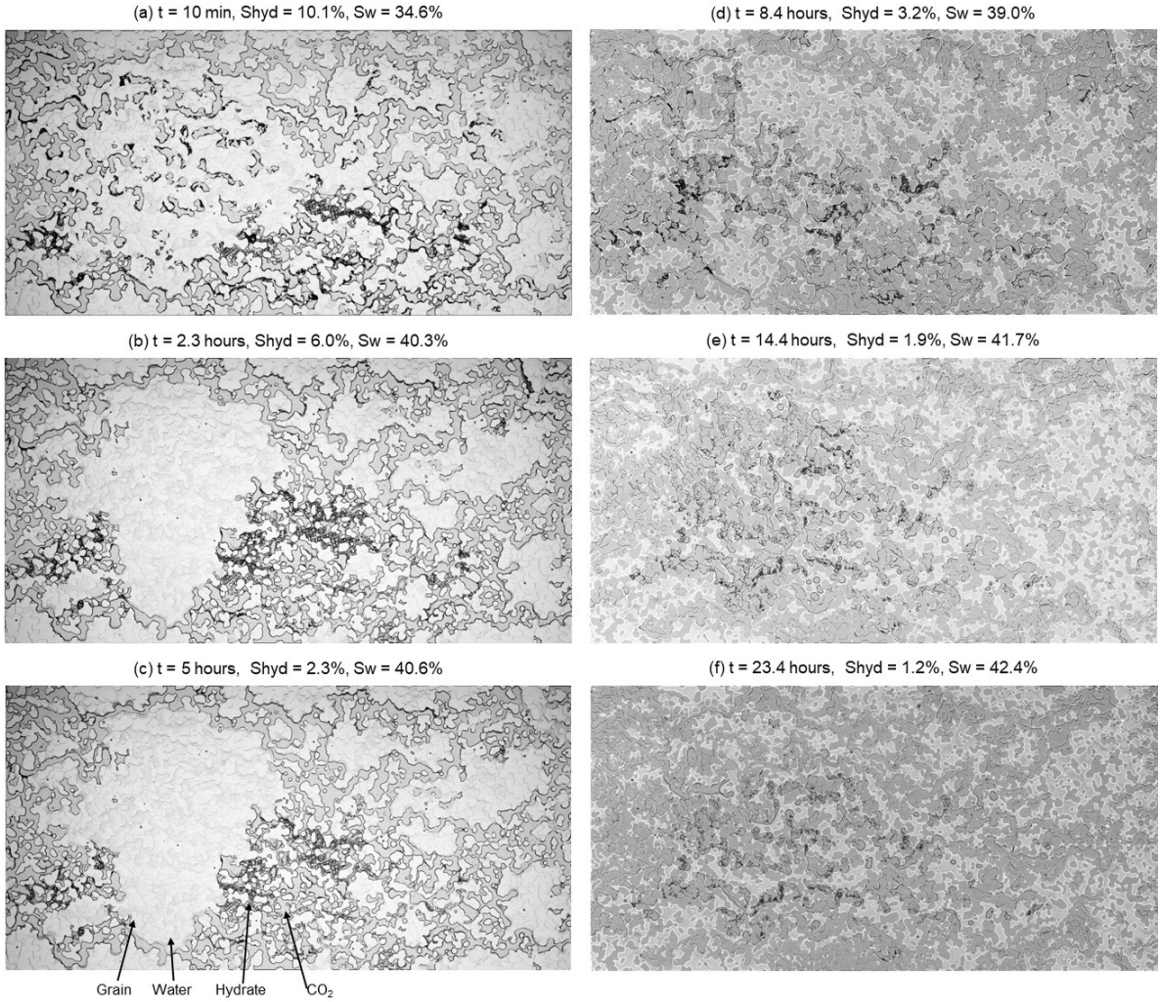

Figure 4.9: Selected key images to visualize the hydrate behaviour during hydrate formation in Experiment #2.

At t = 2.3 hours, total hydrate saturation decreased significantly to 6%, while water saturation increased to 40%. A clear drop in hydrate saturation was observed in Areas 1, 2, and 4, particularly in Area 2, where hydrate saturation dropped from 2% to 0.4%, while water saturation simultaneously increased from 7.6% to 15.4%. This indicates substantial hydrate dissociation in Area 2, resulting in increasing water saturation. In contrast, hydrate saturation in Area 3 remained relatively stable, although its distribution became more localized toward the central region of the area rather than being spread out vertically as in the initial stage.

At t = 5 hours, hydrate saturation further decreased to 2.3%, with reductions occurring in all areas, and a slight increase in total water saturation, especially in Area 2, suggesting that dissociation was still ongoing at this stage.

At t = 8.4 hours, a notable change in saturation occurred, particularly in Area 2. Hydrate saturation increased in both Areas 1 and 2, resulting in a total hydrate saturation increase of 2.3%. At the same time, water saturation in Area 2 dropped dramatically from 16.3% to 8.3%. Water saturation became more evenly distributed across all areas.

By t = 14.4 hours (within the interval from 11.5 to 15 hours), total hydrate saturation decreased slightly to 1.9%, mainly due to hydrate reduction in almost all areas, except for a slight increase in Area 2. The hydrate in Areas 4 and 5 had nearly fully dissociated, as indicated by very low hydrate saturation and increased water saturation.

At t = 23.4 hours (spanning 15.5 to 30 hours), hydrate saturation further decreased to 1.2%, with

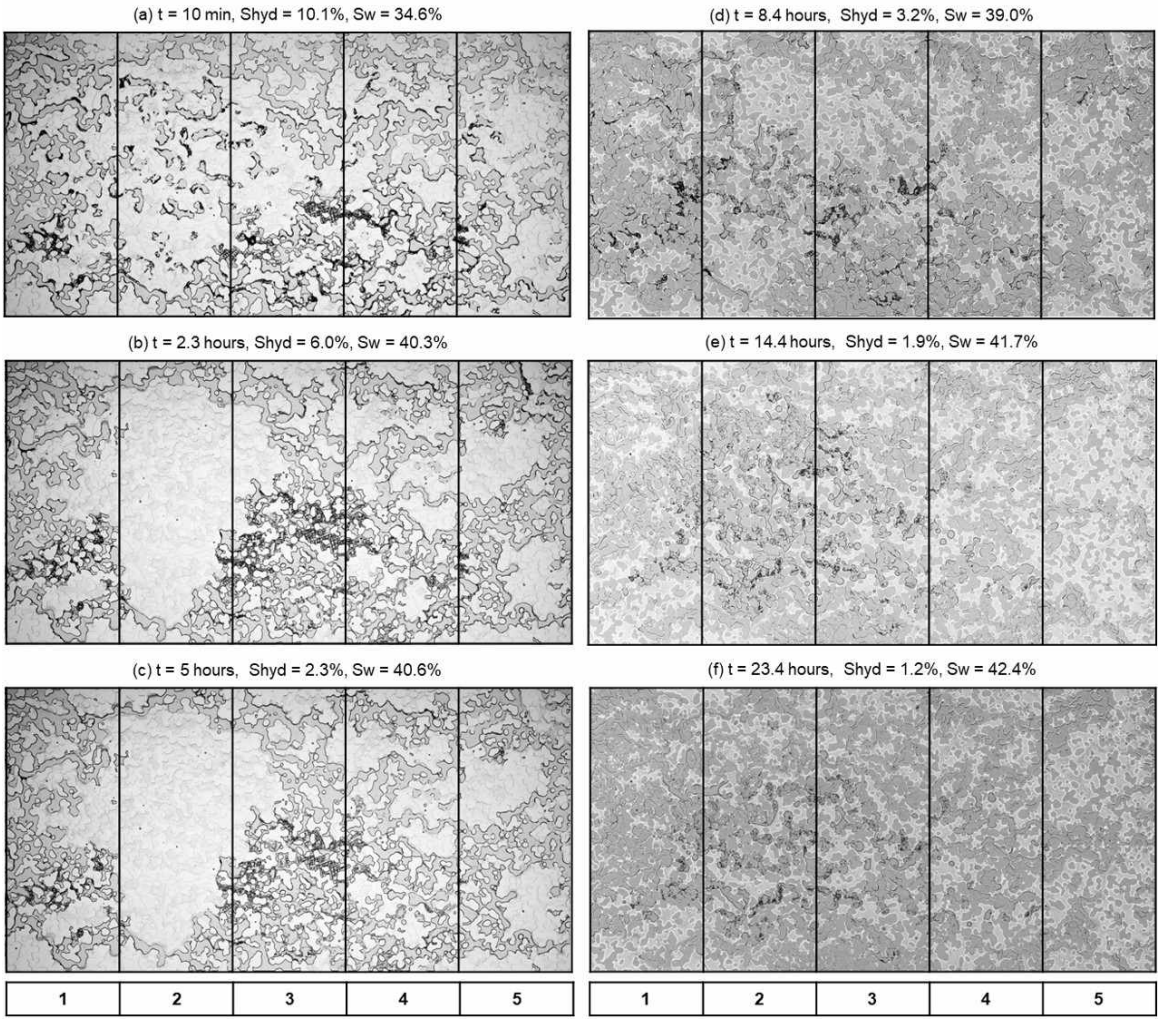

Figure 4.10: Division of key images into five regions to visualize the localized hydrate formation behavior in Experiment #2.

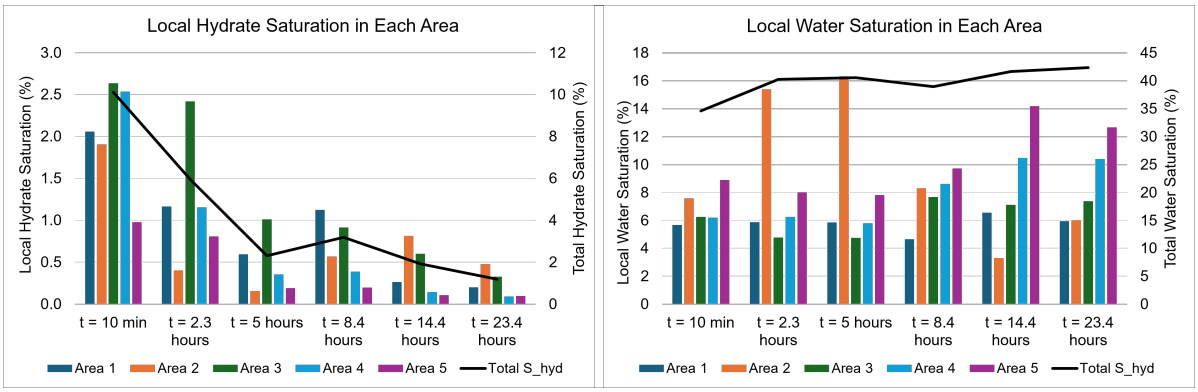

Figure 4.11: Local hydrate saturation (left) and local water saturation (right) profiles in Experiment #2.

hydrates predominantly located in Areas 2 and 3. The hydrate saturation remained relatively stable throughout the following 15-hour observation period.

These spatial and temporal variations in saturation suggest that hydrate formation and dissociation can occur simultaneously, even during the hydrate formation phase. However, the distribution was sparse and did not have a clear pattern. This might be because the hydrate formation is a random and stochastic process.

The phenomenon of simultaneous hydrate formation and dissociation during the formation process can be explained by the Labile Cluster Theory (LCT), which states that hydrate formation is not a straightforward process but involves the formation of unstable, temporary clusters that continuously assemble and disassemble before reaching the critical size required for stability (Gambelli, Filipponi, and Rossi, 2022). Furthermore, Ostwald ripening and sintering theory describe how smaller hydrate particles can dissolve and redeposit onto larger ones, gradually reducing overall saturation despite ongoing nucleation (Xu and Konno, 2025). This behaviour is evident in the changing local hydrate saturation from Figure 4.10a to Figure 4.10b, where the hydrate in area 2 dissolves and redeposits in the middle of area 3. In systems containing $CaCl_2$, ion pairing above 10 wt% reduces water activity and hinders hydration, potentially promoting local dissociation (Lida Yan and Balasubramanian, 2023). Finally, the salinity-buffered mechanism highlights that salt exclusion during hydrate formation can increase local salinity, driving the system toward a three-phase equilibrium (gas, water, hydrate), and thereby limiting further hydrate growth (You et al., 2015). These combined effects contribute to a dynamic system in which CO_2 hydrate formation and dissociation can occur simultaneously.

It is worth noting that brightness differences in the images are due to varying lighting intensities. Because of challenges in analyzing the entire image set for water saturation, analysis was limited to six selected images. The results show an inverse relationship between water and hydrate saturation. When hydrate saturation increases, water saturation tends to decrease, and vice versa. Furthermore, the sum of water and hydrate saturation in these selected images ranges from 42% to 46%, which is reasonably consistent with the initial water saturation of approximately 48%.

4.2.2. Hydrate Morphology

The hydrate morphology observed in this experiment is initially visible in Figure 4.9. However, to more clearly illustrate the morphological features, a magnified view is provided in Figure 4.12. Several types of hydrate morphology were identified, including pore-filling, grain-coating, and patchy structures. Interestingly, a distinct ”sheet-like” hydrate structure was also observed. This structure, which has previously been reported during CO_2 hydrate formation in demineralized water by Schellart (2024), is rarely documented in the literature.

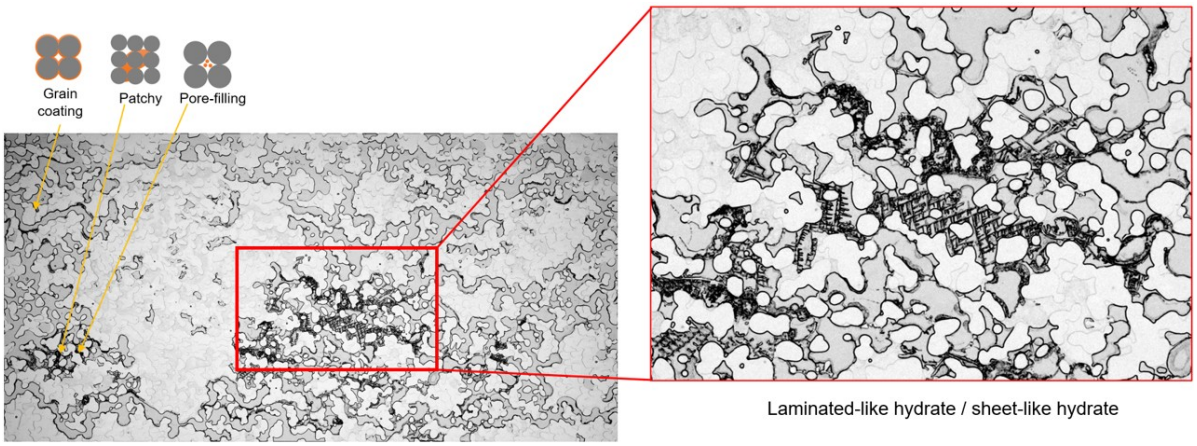

Figure 4.12: CO_2 hydrate morphology in Experiment #2, highlighting pore-filling, grain-coating, patchy, and rare sheet-like structures.

4.2.3. Dissociation Process

After 30 hours of hydrate formation observation, the dissociation process was initiated. Dissociation was carried out by gradually increasing the temperature in four stepwise stages: from -7°C to -4°C, then to -1°C, followed by 0°C, and finally to 1°C. Figure 4.13 shows the hydrate saturation and temperature profiles during the dissociation phase.

The onset of dissociation was identified by a significant drop in hydrate saturation corresponding to the temperature. It was observed that the hydrate began to dissociate at a temperature of approximately -4°C. The hydrate was fully dissociated at a temperature of around 1°C.

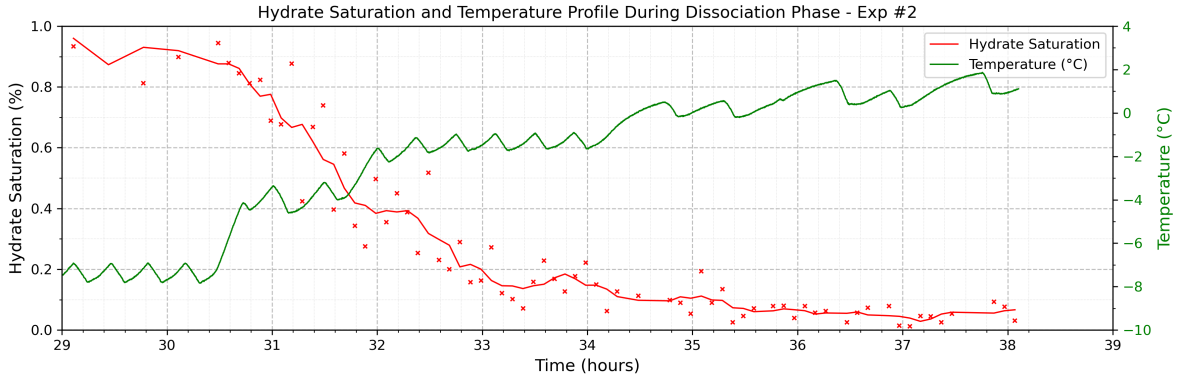

Figure 4.13: CO_2 hydrate saturation and temperature profiles during dissociation in Experiment #2.

4.3. Experiment #3: Microfluidic Experiment using NaCl-1wt% and Dodecane

The third experiment was conducted using NaCl-1wt% and dodecane. In this experiment, NaCl-1wt% represents low-salinity formation water, while dodecane simulates the oil-based mud (OBM) filtrate originating from the base oil. To distinguish between the brine and oil phases in image analysis, 0.05 wt% of Oil Red O was added to the dodecane, giving the oil phase a red coloration.

The experiment began with full saturation of the micromodel using NaCl-1wt%. Dodecane was then injected to simulate mud filtrate invasion into the reservoir. The system pressure was maintained at 25 bars to simulate depleted reservoir conditions, and the temperature was set to -1 $\pm$ 0.5°C to ensure that the experimental conditions remained within the hydrate stability zone. Subsequently, CO_2 was injected at a constant rate of 10 μL/min.

Figure 4.14 shows the pressure and temperature profiles during the experiment, starting from the CO_2 injection phase. After 23.5 hours of injection, no hydrate formation was observed. A 0.3-second pressure pulse was then applied to promote hydrate formation. Following the pulse, hydrate formation occurred rapidly.

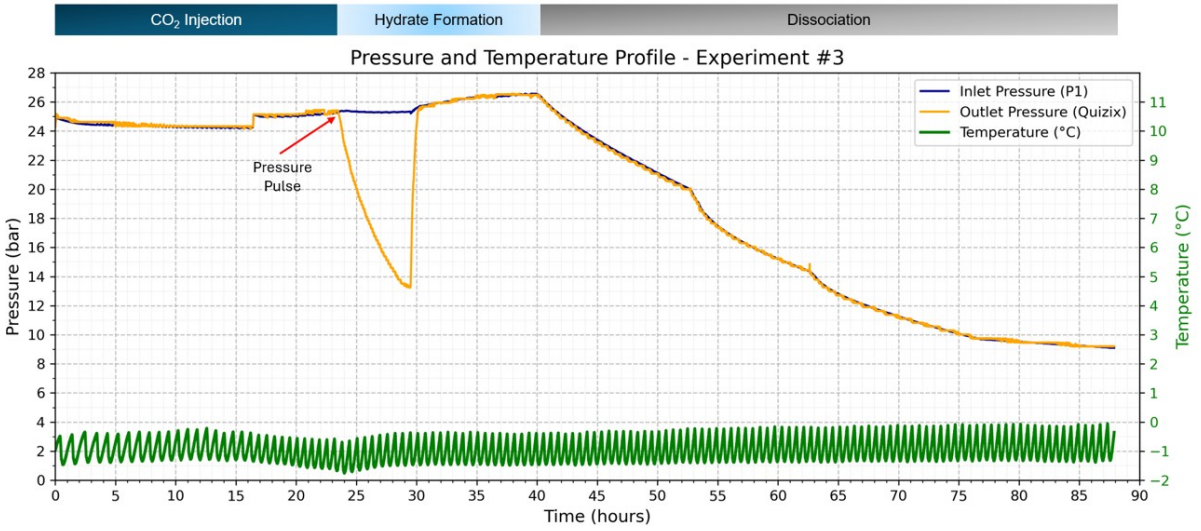

Figure 4.14: Pressure and temperature profiles during Experiment #3.

Due to an operational issue during the experiment, a pressure decline occurred after 16 hours of hydrate formation (t = 40 hours). This was caused by the temporary closure of the CO_2 source for safety reasons, as the laboratory became inaccessible. Despite this, the duration of hydrate monitoring was

sufficient to meet the experimental objectives. The pressure decline could also drive the hydrate dissociation process, which occurs at constant temperature. This confirmed that the observed structures were indeed hydrates, as they dissociated when the pressure–temperature conditions shifted outside the hydrate stability zone.

Figure 4.15 shows micromodel images captured at various stages of the experiment, starting from the image after CO_2 injected in the micromodel, application of the pressure pulse, an image during hydrate formation in the micromodel, and the hydrate dissociation phase.

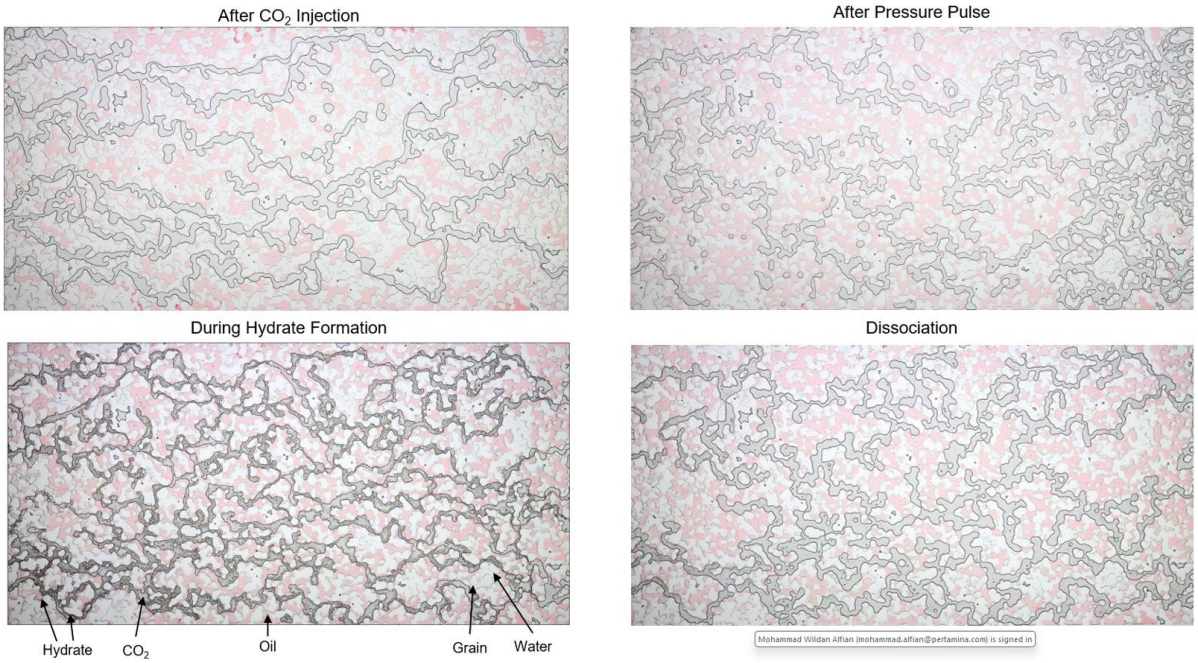

Figure 4.15: Micromodel images captured at various stages of the experiment #3.

The detailed analysis of hydrate formation behavior, associated morphological characteristics, and the dissociation process will be presented in the following sections. The image analysis primarily focused on the hydrate formation phase. A total of 75 images were selected to analyze hydrate formation behavior after the application of the pressure pulse, with particular emphasis on hydrate and oil saturation profiles. In contrast, water and CO_2 saturation were analyzed only for selected images that exhibited significant changes in hydrate and oil saturation. Additionally, image analysis during the dissociation phase was conducted solely to verify whether hydrate dissociation occurred after pressure and temperature conditions shifted outside the hydrate stability zone.

The experiment was then repeated with a focus on investigating the dissociation behavior by increasing the temperature while maintaining the pressure constant at 25 bars. The profile of the repeated experiment is presented in the Appendix C.

4.3.1. Hydrate Morphology

Figure 4.16 shows a representative image from the micromodel during the hydrate formation process. The red color represents oil, the gray color indicates CO_2, while the water and grain phases appear in similar white tones but are separated by dark interface lines, delineating the boundaries between water and grain surfaces. The black color represents hydrate. Hydrate formation within the CO_2 channel was identified by the presence of black features in those regions.

Compared to the experiment using only water or brine, distinct hydrate features were observed when oil was present in the system. Hydrate not only forms at the CO_2-water interface, but also within the CO_2 pathway itself. In this experiment, the hydrate formation was predominantly located inside the CO_2 channels. Additionally, the width of these CO_2 pathways appeared narrower compared to those observed in the experiments without oil.

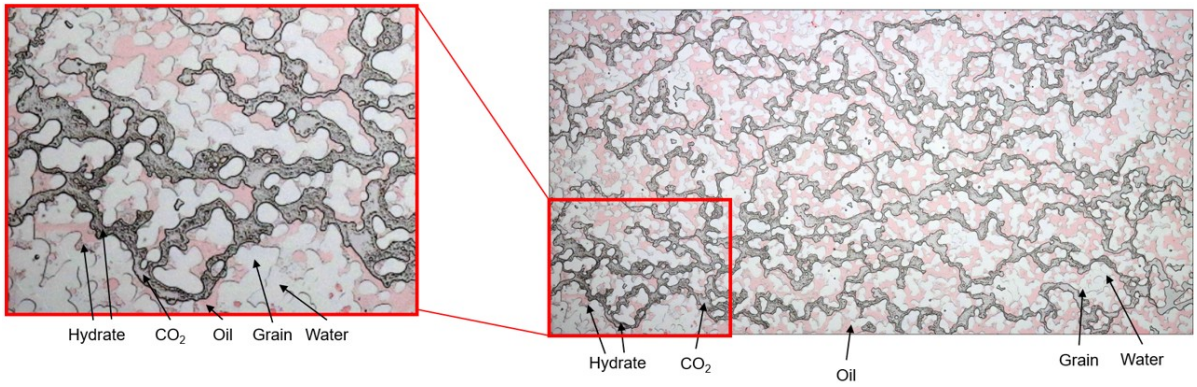

Figure 4.16: CO_2 hydrate morphology in Experiment #3.

4.3.2. Hydrate Formation

Following 23.5 hours of continuous CO_2 injection, there was no visible indication of hydrate formation within the micromodel. This observation was also supported by the lack of any notable increase in differential pressure between the inlet and outlet, suggesting an absence of flow obstruction typically caused by hydrate accumulation. During this period, the water saturation remained relatively steady in the range of 15–17%, reinforcing the inference that hydrate formation did not occur under these conditions.

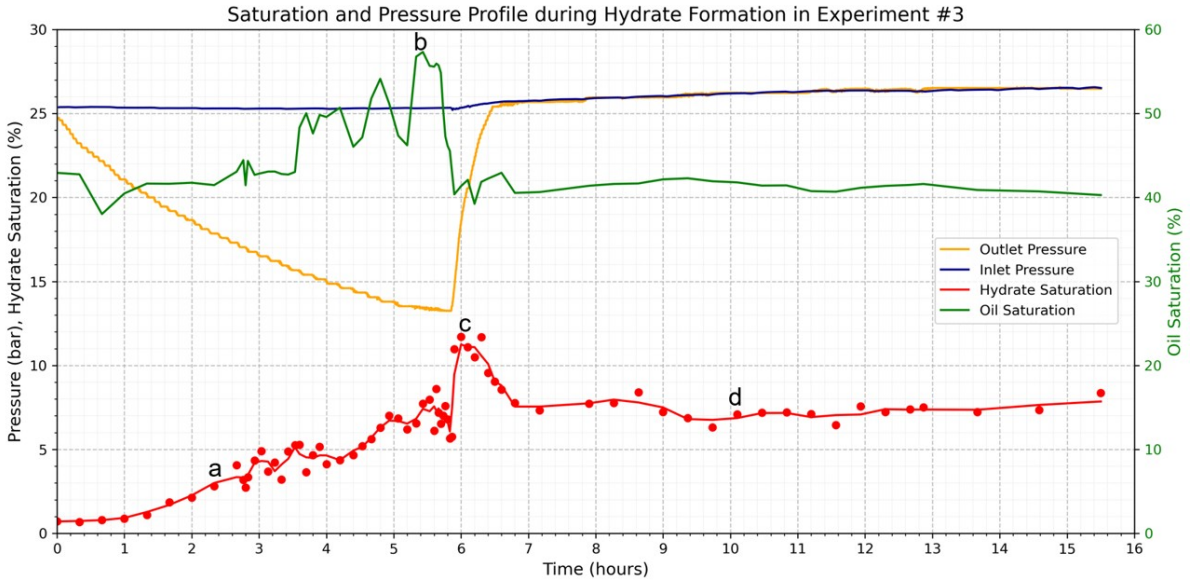

Figure 4.17: Saturation and Pressure Profile during Hydrate Formation in Experiment #3.

To stimulate hydrate nucleation, a 0.3-second pressure pulse was applied, introducing a disturbance in the system. This intervention successfully triggered hydrate formation. Figure 4.17 presents the evolution of hydrate and oil saturation, superimposed with inlet and outlet pressure profiles over time. The t = 0 in this figure refers to the time after the pressure pulse is applied. Throughout the observation, the temperature was maintained at -1 $\pm$ 0.5°C After the pressure pulse, the water saturation stabilized around 6–7%, as depicted in Figure 4.18.

As illustrated in Figure 4.17, hydrate saturation gradually increased to approximately 7–8% over the first 5.9 hours. This growth was accompanied by poor connectivity of the CO_2 pathway from inlet to outlet, indicating flow resistance of CO_2, which also well correlated with a decline in the outlet pressure or rising pressure drop across the domain.

Oil saturation initially remained stable at 42–43% until approximately 3.5 hours, after which it increased

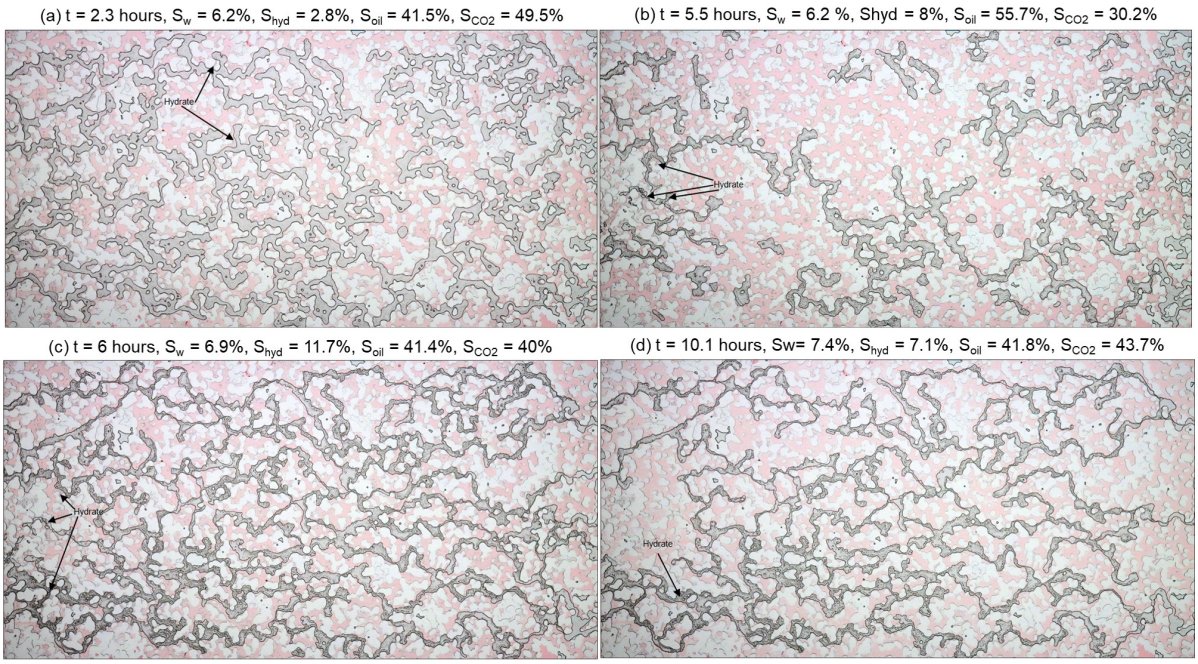

Figure 4.18: Selected images to visualize the hydrate behaviour during hydrate formation in Experiment #3.

significantly, reaching a peak of 56% at t = 5.6 hours. This increase in oil saturation may be attributed to oil expansion caused by the pressure decrease along the domain. Subsequently, after the pressure dropped to 13 bars at t = 5.85 hours, the hydrate saturation slightly decreased, then suddenly jumped to 11%, coinciding with a significant increase in outlet pressure. This may indicate that 13 bars is the hydrate dissociation pressure for the system, which is also aligned with the hydrate equilibrium line presented in Figure 3.7. Once this thermodynamic condition was reached, some of the hydrate likely dissociated. This dissociation may have triggered a sudden disturbance in the system, similar to a pressure pulse, which in turn induced a notable redistribution of fluids in the micromodel, as evidenced by the significant changes between Figure 4.18b and Figure 4.18c, along with the sharp increase in hydrate saturation. From t = 6.8 hours onward, both hydrate and oil saturations stabilized at 7% and 41%, respectively, with minimal pressure difference, indicating a quasi-equilibrium state. The conversion factor during this experiment was approximately 28 - 36%.

These observations underscore the complexity of hydrate formation when oil is present in the system. The dynamic processes of oil expansion and thermodynamic conditions both influence hydrate formation and dissociation within the system. However, several experimental limitations must be acknowledged. The use of a single camera limited the ability to capture vertical phase layering among CO_2 gas, oil, and water. The pressure drop might not only be caused by the hydrate clogging in the micromodel, but also by hydrate blockage in the tubing line of the system, which could not be visibly observed during the experiment. Additionally, since pressure changes were controlled at the outlet side using a Quizix pump, hydrate dissociation could occur when pressure decreased. In real operations, however, the outlet side acts as a pressure reservoir and does not experience significant pressure drops; instead, pressure variations primarily occur at the bottom-hole (inlet) side of the reservoir system.

4.3.3. Dissociation Process

The dissociation process in this experiment occurred unintentionally due to a drop in pressure while maintaining a constant temperature. The objective of the analysis in this section is to confirm whether the hydrate-like feature observed within the CO_2 channel indeed dissociates when conditions fall outside the hydrate stability zone (HSZ).

As shown in Figure 4.19, when the system reached 9.75 bars at -1°C, which is the conditions that lie outside the HSZ, the hydrate feature within the CO_2 channel was no longer visible. This confirms that the previously observed structure was indeed hydrate.

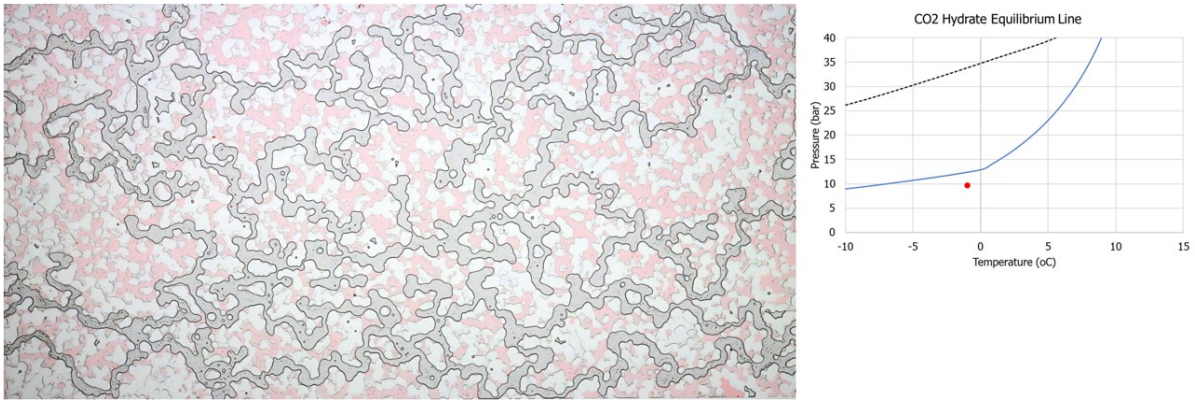

Figure 4.19: Micromodel image at 9.75 bars and -1°C during the dissociation process, showing hydrate dissociation when pressure and temperature conditions are outside the hydrate stability zone.

A repeat experiment for Experiment #3 was also conducted, focusing specifically on the dissociation process by increasing the temperature while maintaining constant pressure. The results of this dissociation experiment are presented in the Appendix. Based on the observations, the estimated dissociation temperature was approximately 5.1 - 5.6°C.

4.4. Experiment #4: Microfluidic Experiment Using $CaCl_2$-15wt% and Dodecane

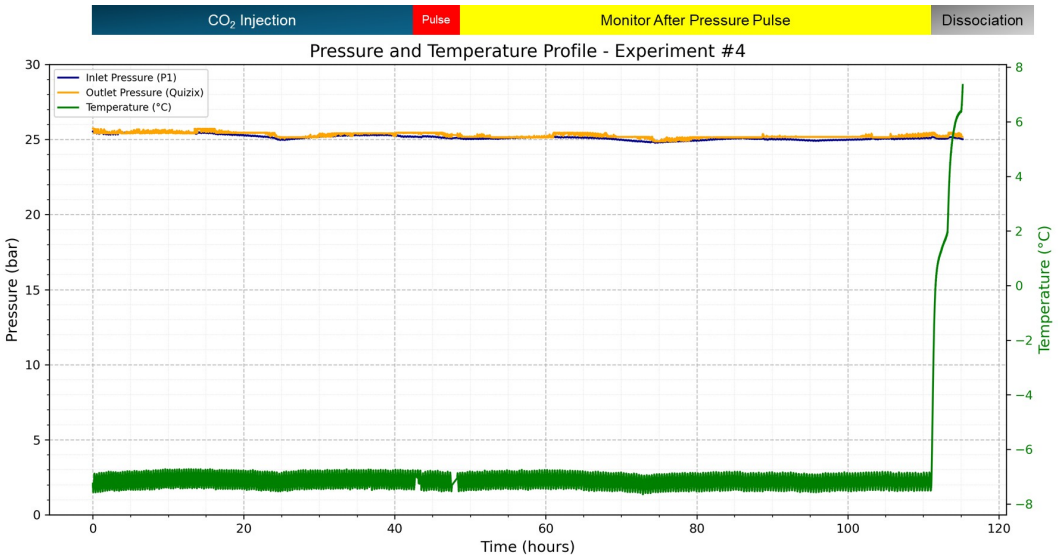

Figure 4.20: Pressure and temperature profile during Experiment #4.

As OBM typically consists of a base oil (continuous phase) and brine (dispersed phase), this experiment aimed to investigate the effect of these fluids by simulating them as separate OBM filtrates. Dodecane was used to represent the mud filtrate from the base oil, while $CaCl_2$-15wt% brine represented the filtrate from the dispersed aqueous phase.

During the experiment, CO_2 was injected at a rate of 10 µL/min. The system pressure was maintained at approximately 25 bars and temperature at -7 ± 0.5°C to ensure that conditions remained within the hydrate stability zone, with a subcooling of approximately 6°C from the equilibrium temperature as simulated in Hydraflash by M. Aghajanloo et al. (2024).

Figure 4.20 presents the pressure and temperature profile throughout the experiment, starting from the CO_2 injection phase. At the early stage of CO_2 injection, the saturation values for CO_2, oil, and water

were 33.8%, 25.4%, and 40.7%, respectively, as illustrated in Figure 4.21. As in Experiment #3, oil appears red, CO_2 is gray, and water has similar white tones with the grain matrix, distinguished by dark interface lines.

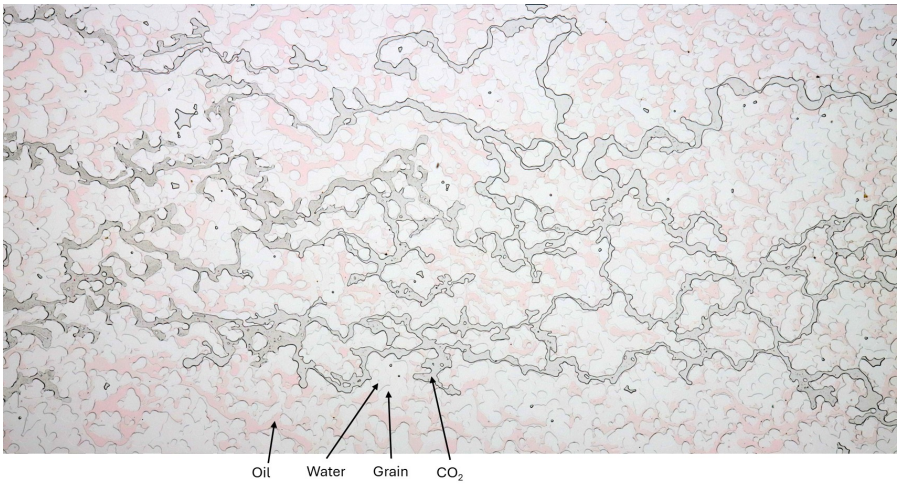

Figure 4.21: Micromodel image during CO_2 injection at the early stage of Experiment #4.

After 43 hours of continuous CO_2 injection, no hydrate formation was observed. Likewise, there was no noticeable change in the pressure differential between the inlet and outlet. To promote hydrate formation, pressure pulses were applied starting with a 0.2-second pulse. However, no hydrate formation was detected even after 4 hours of subsequent monitoring.

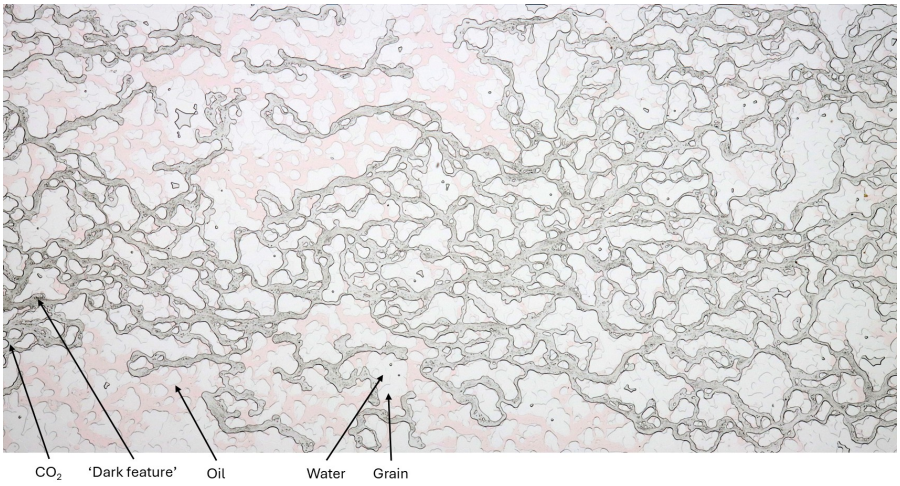

Figure 4.22: Micromodel image after pressure pulses in Experiment #4.

Additional pulses of 0.25 seconds and 0.3 seconds were applied, but still no hydrate was formed. After these pulses, the CO_2, oil, and water saturations were approximately 58.2%, 21.1%, and 20.7%, respectively as shown in (Figure 4.22). A prolonged observation phase was then initiated to monitor potential hydrate formation.

After 63 hours of monitoring, no hydrate formation was evident. Instead, a 'dark feature' was observed within the CO_2 pathway, resembling a blob-like structure, but it lacked the distinct morphology associated with hydrate features as seen in Experiment #3.

To investigate further, a dissociation process was conducted by gradually increasing the temperature from -7°C to 7°C. Throughout the heating process, the 'dark feature' remained unchanged, suggesting that it was not hydrate. This observation was supported by the stable inlet and outlet pressure profiles, which showed no signs of hydrate-induced flow resistance.

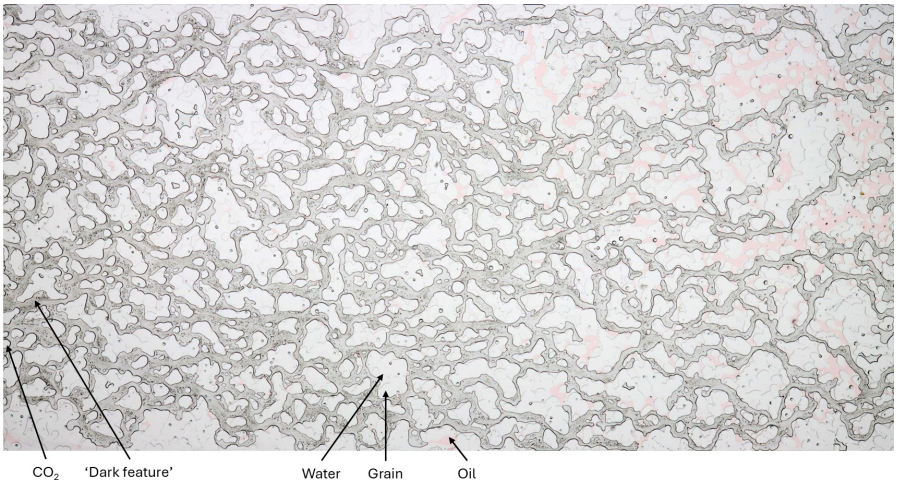

Figure 4.23: Micromodel image during dissociation at 7.3°C and 25 bars in Experiment #4.

A repeat of Experiment #4 was conducted to verify the reliability of the observations. CO_2 injection and several pressure pulses, up to 0.5 seconds, were applied, but no hydrate was formed. The same 'dark feature' appeared within the CO_2 phase, and dissociation heating up to 9°C did not affect its morphology or presence.

These results confirm that no hydrate formation occurred in the presence of $CaCl_2$-15wt% brine and dodecane. The high brine salinity and low post-pulse water saturation (21%) likely cause the difficulties in hydrate formation. Additionally, the presence of oil may have further limited interaction between water and CO_2, thus hindering nucleation and growth of hydrates.

4.5. Experiment #5: Microfluidic Experiment Using NaCl-1wt% and Water-in-Oil Emulsion

Experiment #5 was designed to simulate the impact of oil-based mud, represented by a simplified water-in-oil (W/O) emulsion. The emulsion was composed of dodecane as the base oil, $CaCl_2$-15wt% as the dispersed aqueous phase, and Span 80 as the emulsifying agent. To visually distinguish the emulsion, 0.1 wt% of Oil Red O dye was added to the dodecane, resulting in a red-colored emulsion. The oil-to-water ratio (OWR) was maintained at 50:50. Separately, NaCl-1wt% brine was used to represent the formation water in reservoirs.

Figure 4.24 presents the pressure and temperature profiles throughout the experiment, starting from the CO_2 injection phase. The experiment was conducted in two distinct stages: the first stage aimed to evaluate hydrate formation from the free water phase (NaCl-1wt%), while the second stage focused on hydrate formation from the dispersed aqueous phase within the emulsion ($CaCl_2$-15wt%). Detailed observations and analysis for each stage are provided in the following sections.

4.5.1. First Stage: Hydrate Formation Originating from the Free Water (NaCl-1wt%).

Stage 1 of Experiment #5 investigated the potential for hydrate formation from free water (NaCl-1wt%) in the presence of a water-in-oil emulsion. This stage was repeated in two separate trials. In the initial trial, the emulsion injected at 20 μL/min rapidly displaced the brine due to its higher viscosity, resulting in very low residual water saturation ($\sim$5%). A second trial implemented a lower emulsion injection rate of 1 μL/min combined with brine re-injection, which improved water saturation but remained insufficient for hydrate nucleation. During CO_2 injection, a high flow rate (200 μL/min) was required to displace the emulsion, creating a large pressure differential (approximately 24 bars) between inlet and outlet, followed by a sharp recovery upon CO_2 breakthrough. After 6.5 hours of CO_2 injection, the pressure pulse was applied to accelerate hydrate formation. Subsequently, the prolonged CO_2 injection was performed for more than 40 hours. However, no hydrate formed during the process. It was most likely due to the critically low availability of free water in the system.

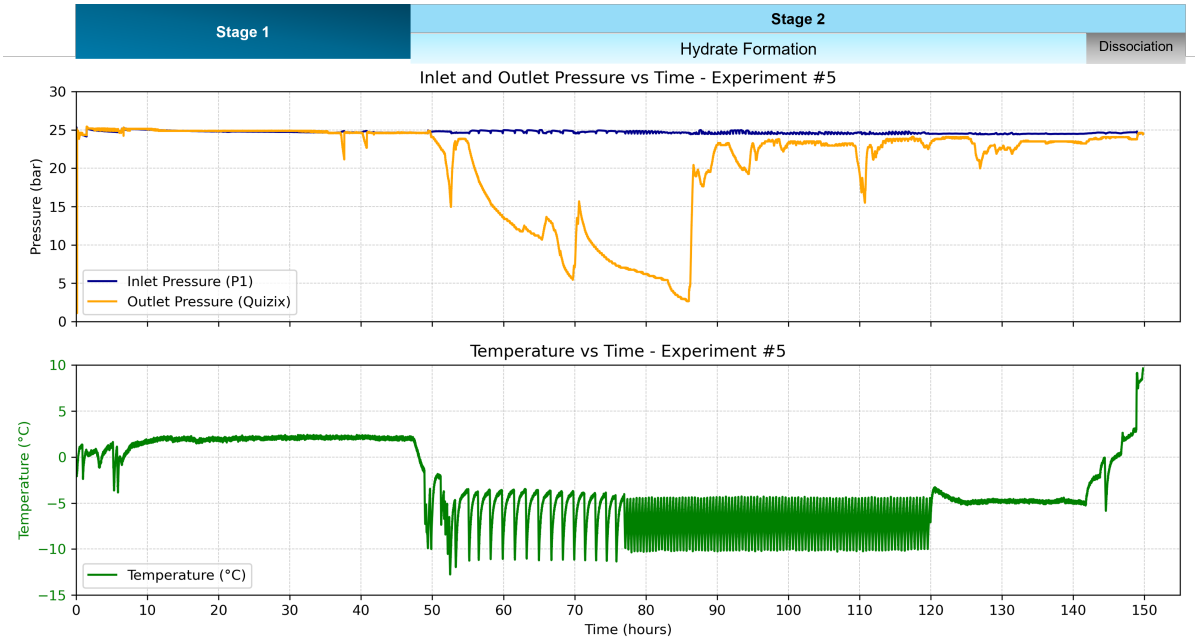

Figure 4.24: Pressure and temperature profile in Experiment #5

Visual and pressure responses indicated that CO_2 dissolved into the emulsion, as evidenced by progressive whitening of the emulsion phase and a gradual decline in inlet pressure. The CO_2 predominantly flowed through previously water-filled channels, while water remained primarily near the grain surfaces due to the water-wet nature of the micromodel. In addition, distinct blob-like gas structures and narrow flow channels were observed in the CO_2 pathways, resembling the similar phenomena reported in earlier oil-filled micromodels in experiment #3 and #4.

The following observations briefly explain the key findings from the experiment:

1. **Emulsion Displacement Efficiency during Emulsion Injection Stage – First Trial.**

   During the first trial of Stage 1, the displacement behavior of the emulsion was examined. As shown in Figure 4.25, the emulsion demonstrated a high displacement efficiency, rapidly displacing the NaCl-1wt% brine from the micromodel within seconds of injection. Despite being injected at a relatively low flow rate of 20 μL/min, the emulsion was able to penetrate and occupy the pore space effectively.

   This behavior was attributed to the significantly higher viscosity of the emulsion compared to brine, which resulted in a strong sweep of the aqueous phase. By t = 15 s, nearly the entire porous structure was filled with the emulsion, leaving only minimal regions of residual water. As a consequence, the water saturation in the system was insufficient to support hydrate formation, and the trial was subsequently considered unsuccessful.

2. **Low-Rate Emulsion Injection Strategy – Second Trial.**

   To overcome the brine displacement issue observed in the first trial, the second trial employed a low-rate injection strategy. The emulsion was injected at a significantly reduced flow rate of 1 μL/min in order to minimize sweeping and enhance water retention within the micromodel. Following the emulsion injection, additional brine was reinjected into the micromodel to further increase the water content. As illustrated in Figure 4.26, this approach was intended to preserve residual brine in the pore space and improve water saturation prior to CO_2 displacement.

   The resulting image revealed regions with varying brightness levels within the emulsion phase, which may indicate partial mixing or dilution between NaCl-1wt% brine and the emulsion.

3. **CO_2 Injection and Pressure Response.**

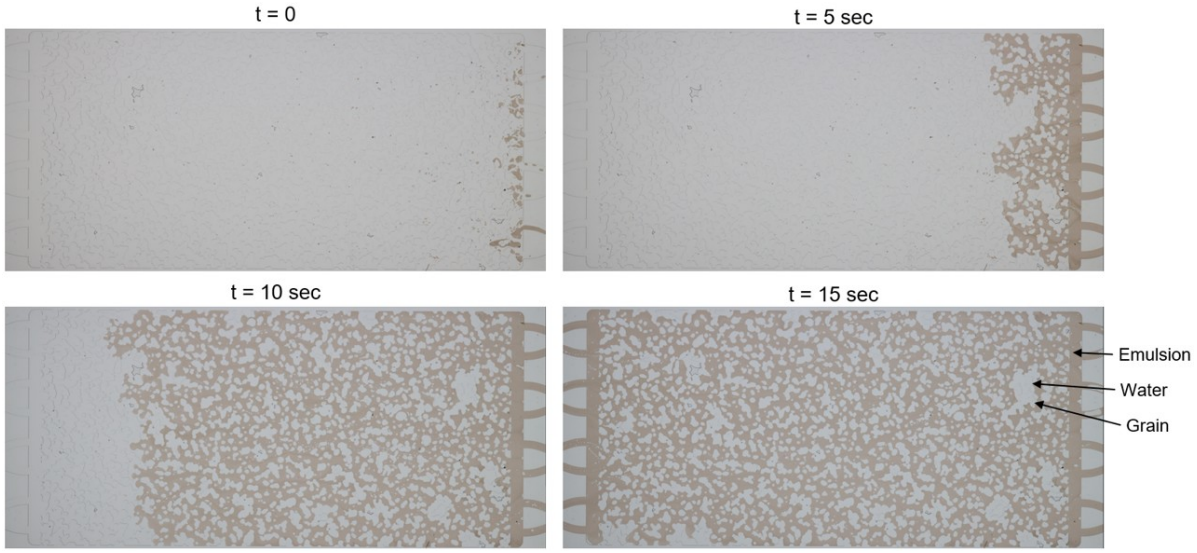

Figure 4.25: Emulsion displaced NaCl-1wt% brine during the first trial at a flow rate of 20 μL/min. Images show emulsion front progression at different time intervals. Flow direction from right to left.

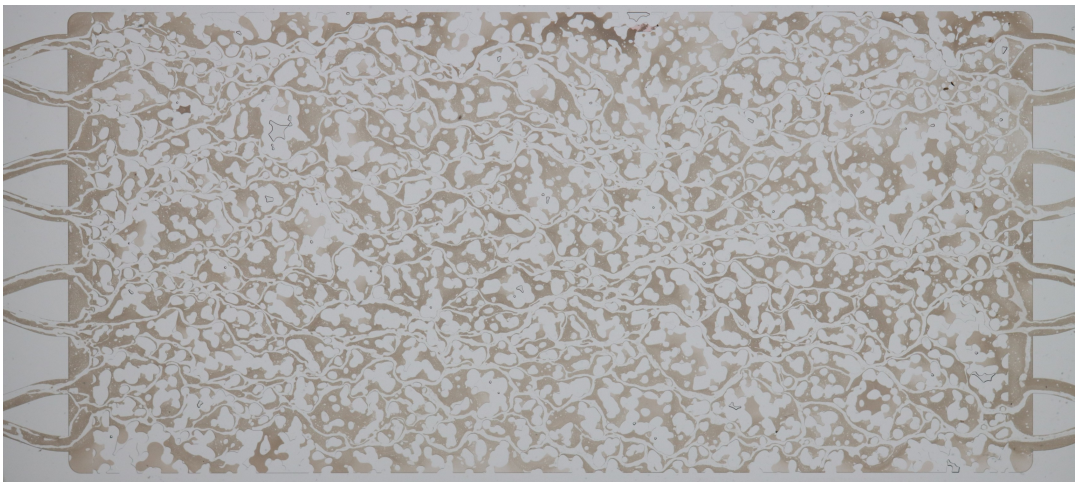

Figure 4.26: Pore-scale distribution of emulsion injected at a low flow rate (1 μL/min) in the second trial. Variations in emulsion brightness suggest potential dilution with NaCl-1wt% brine.

An interesting visual and pressure-based observation was noted as the emulsion became lighter in color during the CO_2 injection, accompanied by a drop in inlet pressure. This phenomenon indicates potential CO_2 dissolution into the emulsion phase.

The CO_2 displacement phase was initiated after emulsion injection and water re-injection were completed. As shown in Figure 4.27, the CO_2 injection began at a low rate of 10 μL/min, which was gradually increased to 50 μL/min and subsequently to 100 μL/min. Despite this increase, the displacement effect remained minimal due to the emulsion's high viscosity.

A significant displacement was only observed when the flow rate was further increased to 200 μL/min. At this point, CO_2 began penetrating the micromodel and displacing the emulsion phase. The pressure response revealed a strong differential between inlet and outlet pressures, with the outlet pressure dropping sharply to approximately 1 bar (Point A), while the inlet pressure was maintained around 25 bars. This indicates a strong flow resistance caused by the emulsion phase. Once the CO_2 front advanced and partially displaced the emulsion, the outlet pressure rapidly recovered to approximately 25 bars (Point B). This sudden pressure drop might resemble a disturbance or a pressure pulse for the system. Figure 4.27 shows the pressure response and the

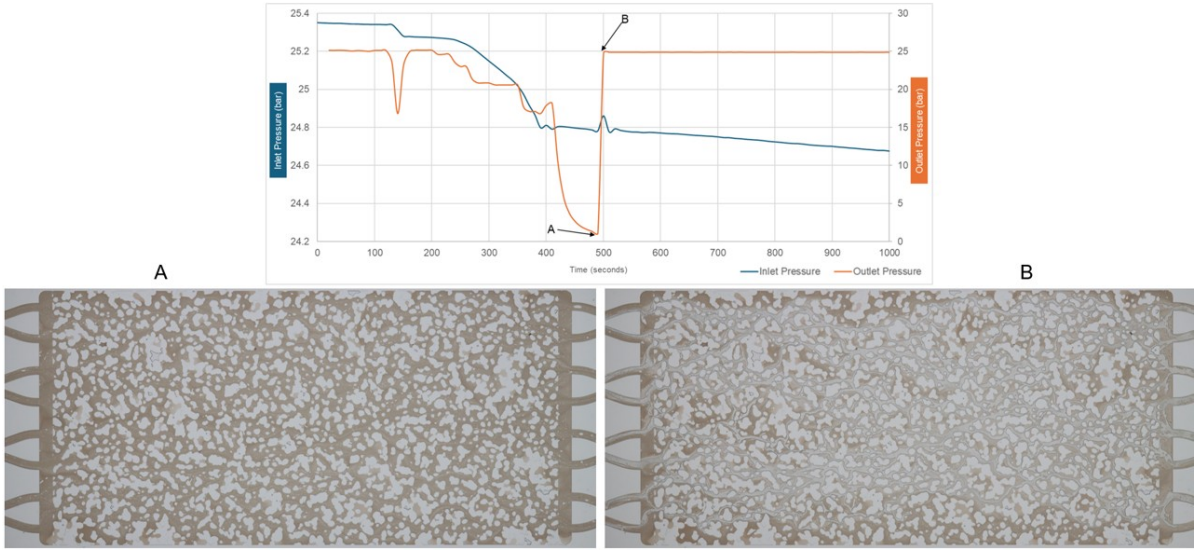

Figure 4.27: (Top) Pressure response during CO_2 injection at varying flow rates. Inlet and outlet pressures diverge significantly at Point A, followed by rapid recovery at Point B. (Bottom) Micromodel snapshots showing fluid configuration before (A) and after (B) CO_2 breakthrough.

micromodel snapshot during CO_2 injection.

4. **Low Water Saturation**

   Following the emulsion injection and CO_2 injection stages, the system exhibited low water saturation, as depicted in Figure 4.28. The brine was observed to remain only in localized regions near the grain surfaces. This behavior is attributed to the strong viscosity contrast between the emulsion and the aqueous phase, which allowed the emulsion to efficiently displace the brine during CO_2 injection. The water-wet nature of the micromodel also promoted preferential wetting near the solid surfaces, leading to the thin brine films observed along the grain boundaries.

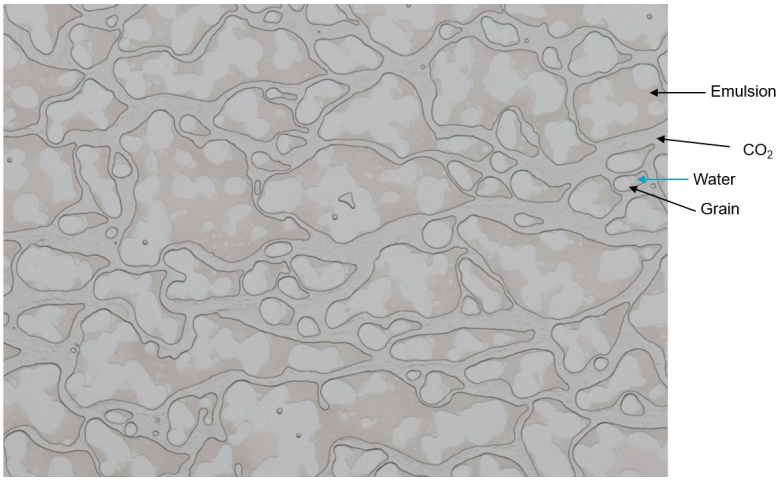

Figure 4.28: Pore-scale fluid configuration showing low water saturation after CO_2 displacement.

Additionally, during the CO_2 injection process, CO_2 preferentially flowed through the main pore channels, which were previously filled by water, as shown in Figure 4.29. This displacement behavior limited the available water phase volume necessary for hydrate formation, further contributing to the absence of hydrates observed during this stage of the experiment.

5. **Emulsion Color Change and CO_2 Dissolution**

   A notable visual change was observed following CO_2 injection, as illustrated in Figure 4.30. Over

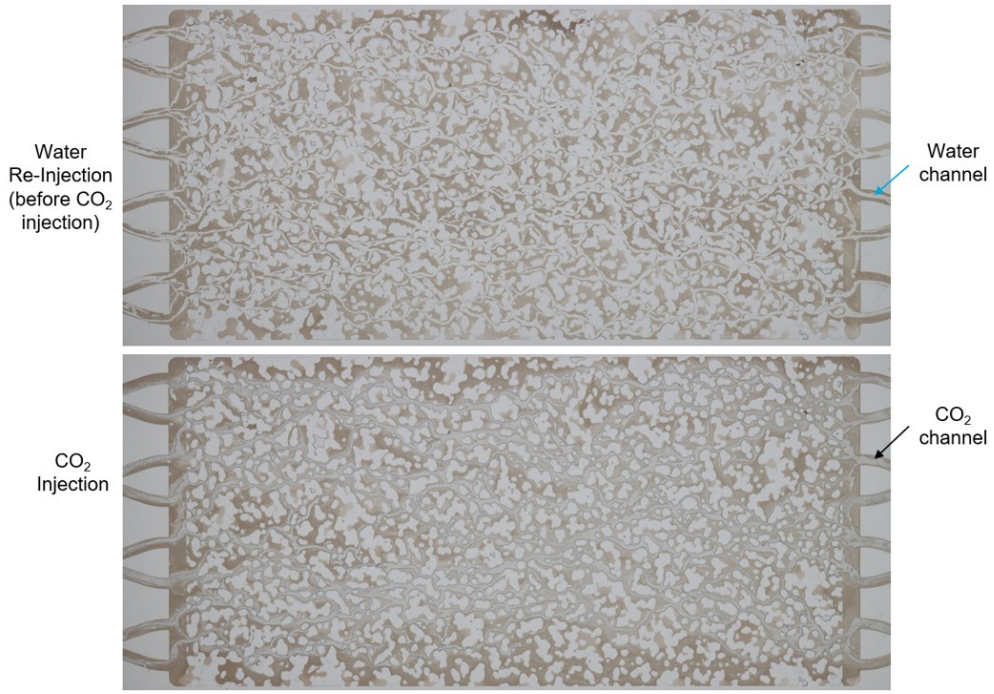

Figure 4.29: CO_2 tended to occupy the main pathways and channels that were initially filled with water during re-injection.

time, the emulsion phase exhibited a progressive whitening, particularly in regions adjacent to the CO_2 channels. This whitening occurred sequentially, with areas closer to the CO_2 flow path turning white earlier than regions farther away.

The whitening of the emulsion was accompanied by a gradual decrease in inlet pressure (P1), as shown in the pressure profile in Figure 4.31. This correlation between visual and pressure responses suggests that CO_2 gradually dissolved into the emulsion phase.

After 8 hours of continuous CO_2 injection, no hydrate formation was observed in the micromodel. To promote hydrate nucleation, a pressure pulse of 0.2 seconds was applied using the automated valve system. Interestingly, similar to the behavior observed during the CO_2 injection process, the emulsion phase continued to undergo visual whitening following the pressure pulse. This whitening effect, indicative of CO_2 dissolution into the emulsion, was consistent with prior observations, as shown previously in Figure 4.30.

6. **Blob Feature in the CO_2 Channel and Narrow Channel Width.** Within the CO_2 channels, 'blob'-like structures and narrow flow paths were observed, resembling behaviors previously reported in dodecane-based micromodel studies. Additionally, the channel appeared to be relatively narrow. This feature was also consistently observed after the pressure pulse, as shown in Figure 4.32.
7. **No hydrate was observed during this stage of the experiment.**

   After 6.5 hours of continuous CO_2 injection, no hydrate formation was observed. A 0.2-second pressure pulse was then applied in an attempt to accelerate hydrate nucleation. Subsequently, a constant CO_2 injection rate of 10 μL/min was maintained for an extended period to monitor potential hydrate formation. However, even after 40 hours of injection, no hydrate was formed. This outcome may be attributed to the very low saturation of free water (i.e., almost no free water remaining), which was likely insufficient to support CO_2 hydrate formation.

4.5.2. Second Stage: Hydrate Formation from Dispersed Water in Emulsion

Stage 2 of Experiment #5 focused on evaluating the potential for hydrate formation from the dispersed brine phase within a water-in-oil (W/O) emulsion, specifically $CaCl_2$-15wt%. Unlike Stage 1, where free water (NaCl-1wt%) served as the primary hydrate-forming phase, this stage aimed to determine whether hydrate crystals could nucleate and grow from water droplets suspended in the emulsion.

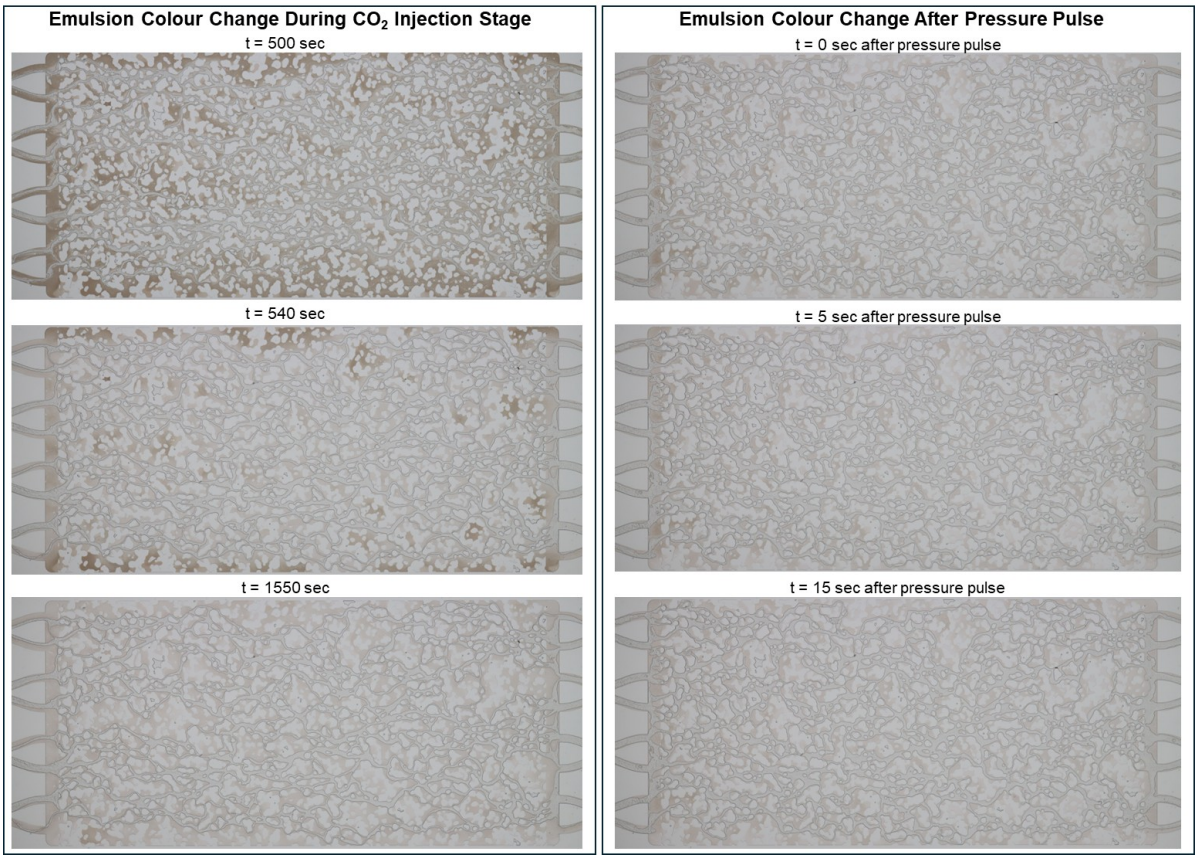

Figure 4.30: Progressive whitening of the emulsion phase observed over time during CO_2 injection stage (left) and after pressure pulse (right), indicating CO_2 dissolution.

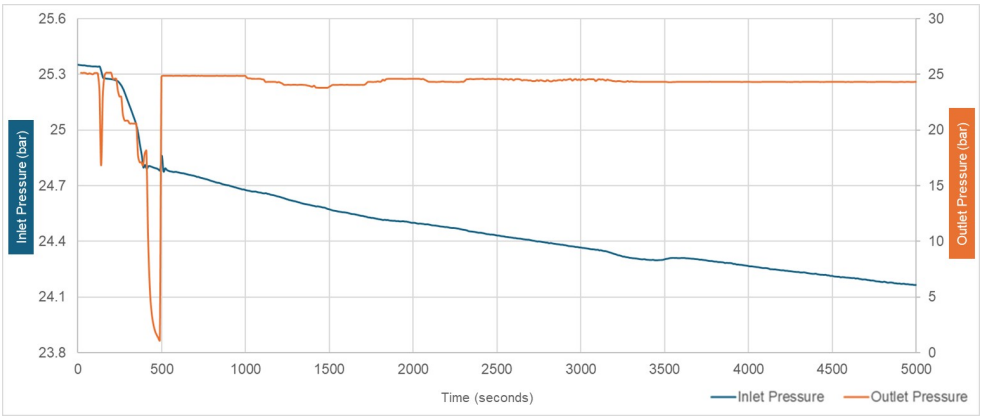

Figure 4.31: Pressure profile shows a corresponding decrease in inlet pressure during CO_2 injection stage.

The experiment was conducted under conditions designed to achieve a subcooling of approximately 6 °C, with the system temperature controlled at around -7 °C. However, due to technical issues, temperature fluctuations of up to ±3 °C were observed during the experiment. Despite these variations, the system remained within the hydrate stability zone for $CaCl_2$-15wt% and above the CO_2 condensation threshold, ensuring valid conditions for hydrate formation.

Figure 4.33 summarizes the key findings from this stage. Upon CO_2 injection, the gas was observed to dissolve into the emulsion, gradually destabilizing its structure. This was likely due to changes in interfacial tension and the impact of gas solubility on droplet integrity. As a result of this destabilization, droplet coalescence occurred. These conditions favored hydrate nucleation as the surface area of

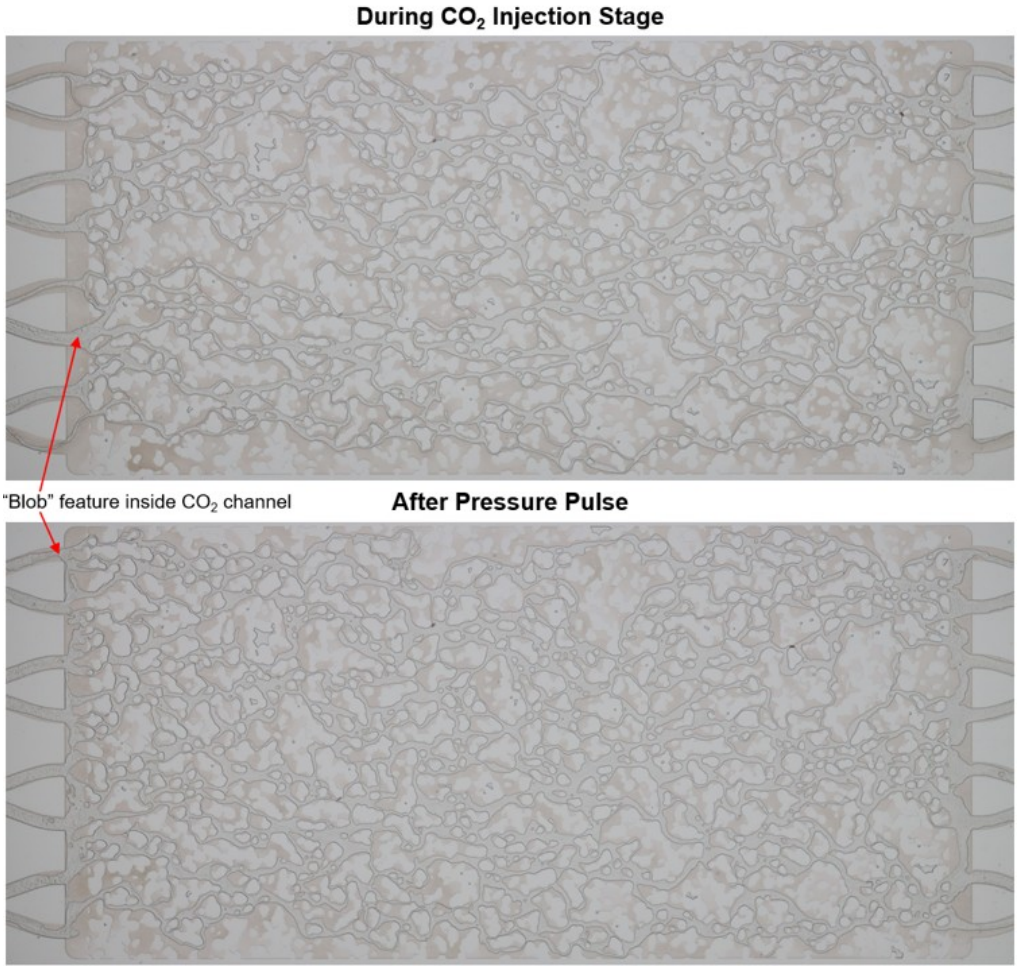

Figure 4.32: Blob Feature in the CO_2 Channel and Narrow Channel Width during CO_2 injection stage and after pressure pulse.

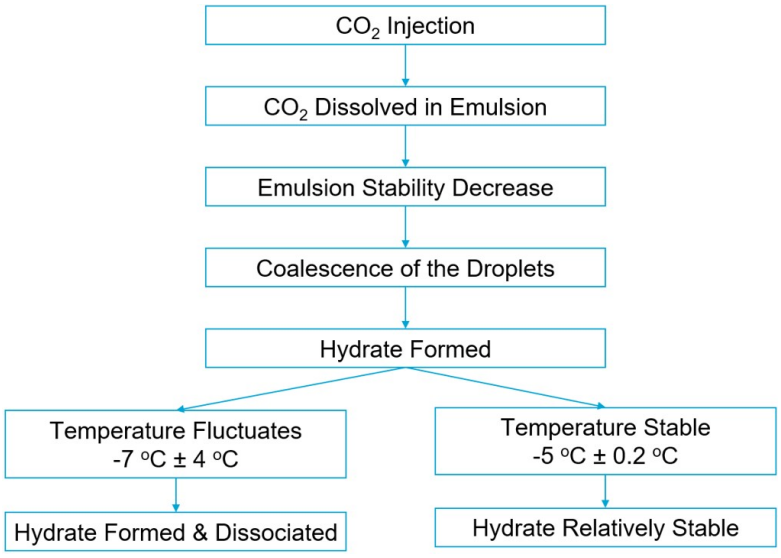

Figure 4.33: Key findings from the second stage of Experiment #5.

water increased, and hydrate formation was confirmed under these circumstances.

However, the stability of the formed hydrate was highly sensitive to thermal variations. When the

system experienced substantial temperature fluctuations (e.g., -10°C $\pm$ -4°C), hydrate formation was often followed by dissociation events, indicating instability. In contrast, when the temperature was maintained more consistently at -5°C $\pm$ 0.2°C, the hydrate remained relatively stable over time.

CO_2 Dissolution in the Emulsion, Emulsion Instability, and CO_2 Hydrate Formation

A consistent phenomenon observed during this stage was the progressive whitening of the emulsion, similar to the behavior noted in the first stage. This color change began near the CO_2 flow pathways and gradually spread outward to more distant regions. It is well established that CO_2 solubility in both oil and water increases as temperature decreases. Consequently, it leads to the destabilisation of the emulsion.

As the emulsion became increasingly unstable, coalescence of the dispersed water droplets was observed. This coalescence resulted in the formation of larger droplets and ultimately led to emulsion breakdown as shown in Figure 4.34d and Figure 4.35a, where the aqueous phase began to separate from the continuous oil phase.

Figure 4.34 illustrates this transition. Images A, B, and C show the progressive whitening of the emulsion due to increasing CO_2 dissolution. In Image D and Figure 4.35a, clear signs of emulsion breakdown are evident, including a shift to a darker tone and the visible separation of the continuous and dispersed phases. Following this phase separation, CO_2 hydrate formation was initiated. The hydrate phase is identifiable by the appearance of black regions, particularly near the micromodel inlet and along the interfaces between the CO_2 channels and the emulsion regions.

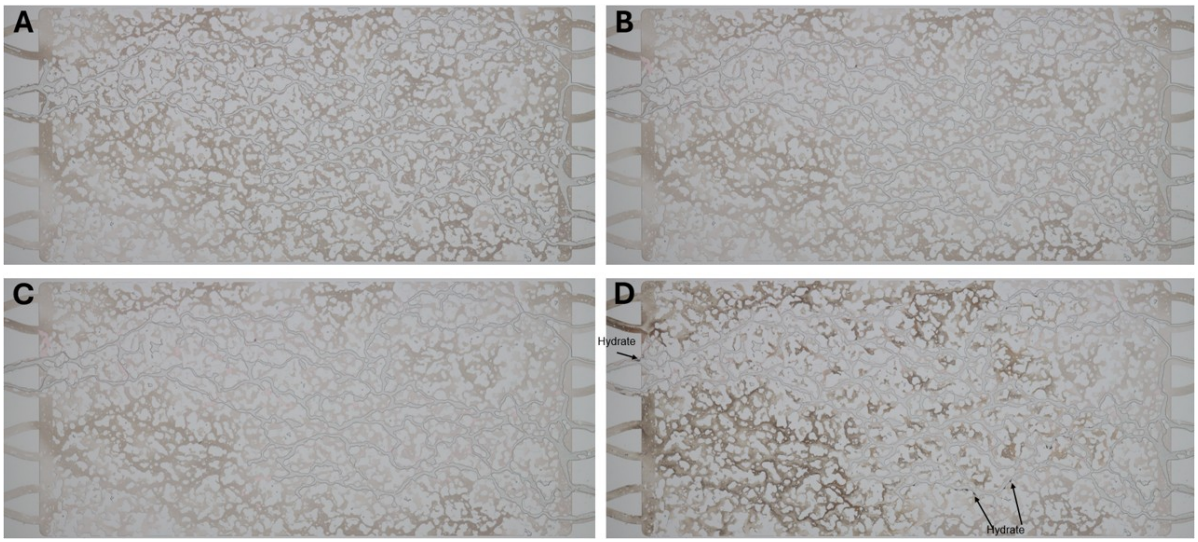

Figure 4.34: CO_2 dissolution in the emulsion, resulting in emulsion instability and hydrate formation. Images A, B, and C show progressive whitening of the emulsion. Image D illustrates emulsion breakdown, followed by hydrate formation (black regions) near the micromodel inlet and at the CO_2–emulsion interface.

Emulsion Features during CO_2 Hydrate Formation

Following the onset of emulsion destabilization, individual water droplets began to emerge from the emulsion matrix. These liberated droplets facilitated direct contact between CO_2 and water, promoting conditions favorable for hydrate formation. The presence of numerous water droplets effectively increased the interfacial surface area available for CO_2 interaction, further enhancing the potential for hydrate nucleation and growth.

Figure 4.35 presents the evolution of the emulsion features during hydrate formation. Figures Figure 4.35a and Figure 4.35b show the emulsion in the early stages of hydrate formation, where dispersed water droplets remain relatively large and sparsely distributed. In contrast, Figures Figure 4.35c and Figure 4.35d depict the emulsion after three days, highlighting increased instability and a noticeable reduction in droplet size.

This progressive droplet size reduction over time not only signifies ongoing emulsion breakdown but also contributes to a greater cumulative water–CO_2 interface area. Such a condition is favorable for

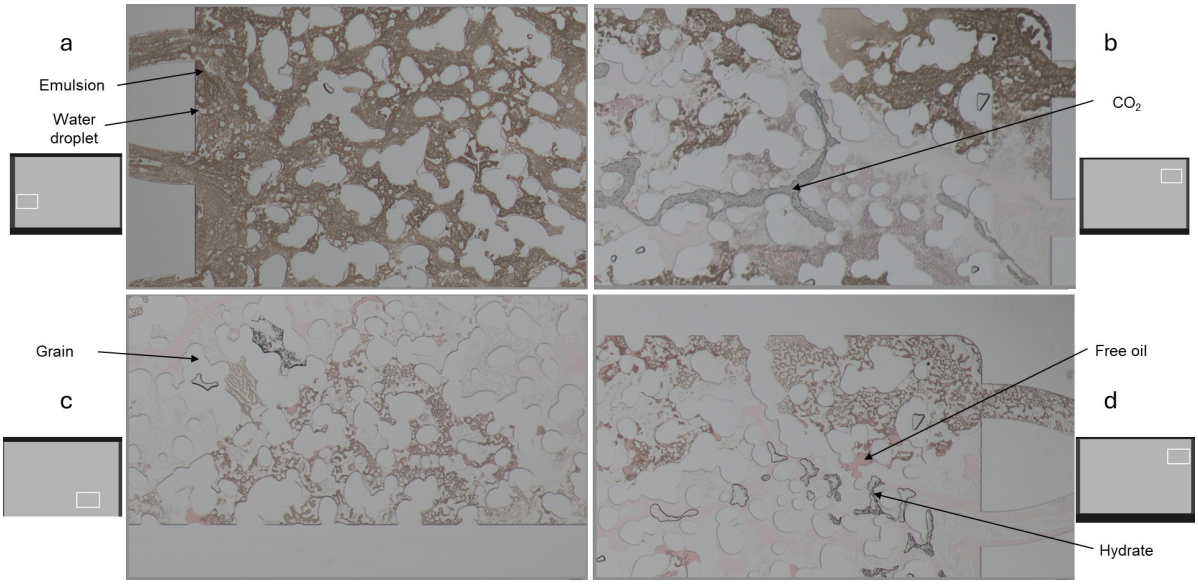

Figure 4.35: Features of the emulsion during CO_2 hydrate formation. (a, b) Early-stage emulsion characteristics with relatively large water droplets. (c, d) Emulsion after 3 days, showing increased instability and reduced droplet sizes.

continued hydrate formation, reinforcing the interplay between emulsion dynamics and gas–water interfacial processes.

CO_2 Hydrate Morphology

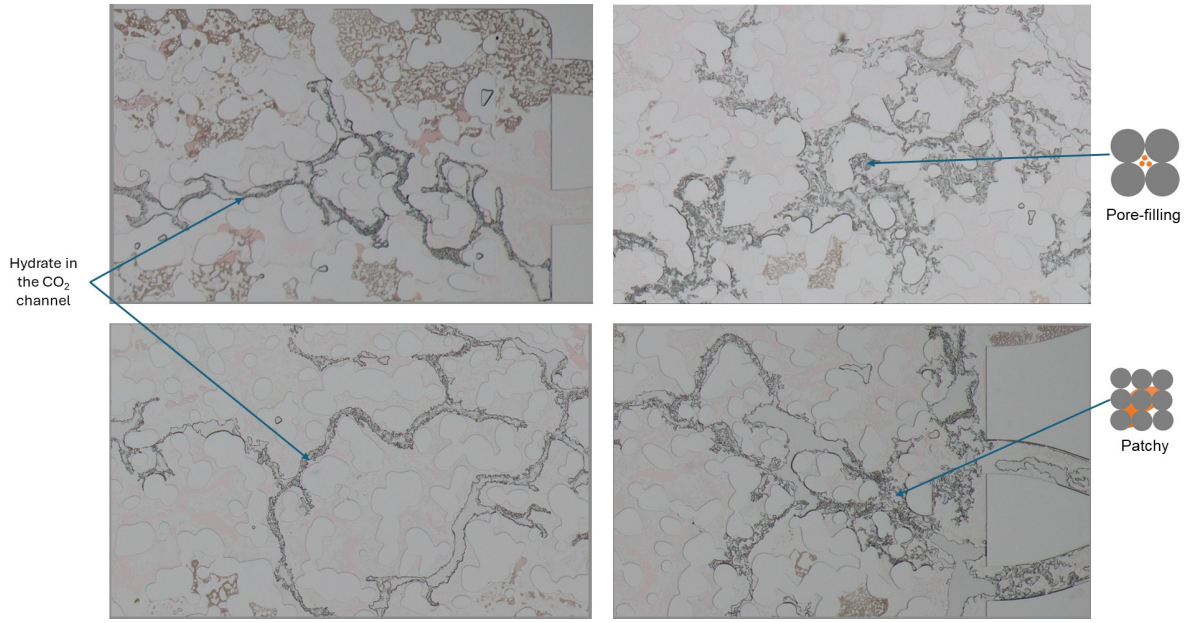

Figure 4.36: CO_2 hydrate morphology in Experiment #5.

Figure 4.36 illustrates the typical morphology of CO_2 hydrates observed during Experiment #5. The hydrate structures exhibited a combination of morphologies, including pore-filling, patchy accumulation, and crystal formation within the CO_2 channels. This combination closely resembled the hydrate morphologies seen in Experiment #3.

In Experiment #5, the hydrate crystals appeared more clearly defined compared to those in Experiment #3. This crystal structure may be attributed to the water droplets in the emulsion, which provided a higher surface area for hydrate nucleation. Additionally, the CO_2 channels in this experiment were narrower than those in the previous experiments.

CO_2 Hydrate Behaviour during Significant Temperature Fluctuation Conditions

A 9-hour segment of the experiment, spanning from t = 83.8 to 93.8 hours (as shown in Figure 4.24), was analyzed to investigate CO_2 hydrate behavior under extreme temperature fluctuations. Figure 4.37 presents the hydrate saturation, pressure, and temperature profiles, while Figure 4.38 illustrates the dramatic changes occurring within the micromodel. These changes include simultaneous hydrate formation and dissociation, as well as significant shifts in the local distribution of hydrate regions.

The temperature during this period ranged from -4.3 to -10.3 °C. According to the hydrate equilibrium line for $CaCl_2$-15wt% reported by M. Aghajanloo et al. (2024), these conditions remained within the hydrate stability zone and above the CO_2 condensation threshold. Nevertheless, the extreme temperature fluctuations resulted in continuous hydrate formation and dissociation. This behavior highlights that hydrate stability is dependent on thermal consistency.

Additionally, temperature fluctuations may influence the CO_2 dissolution dynamics within the oil phase and emulsion. The thermal fluctuations and gas solubility dynamics may contribute to the hydrate instability in this stage of the experiment.

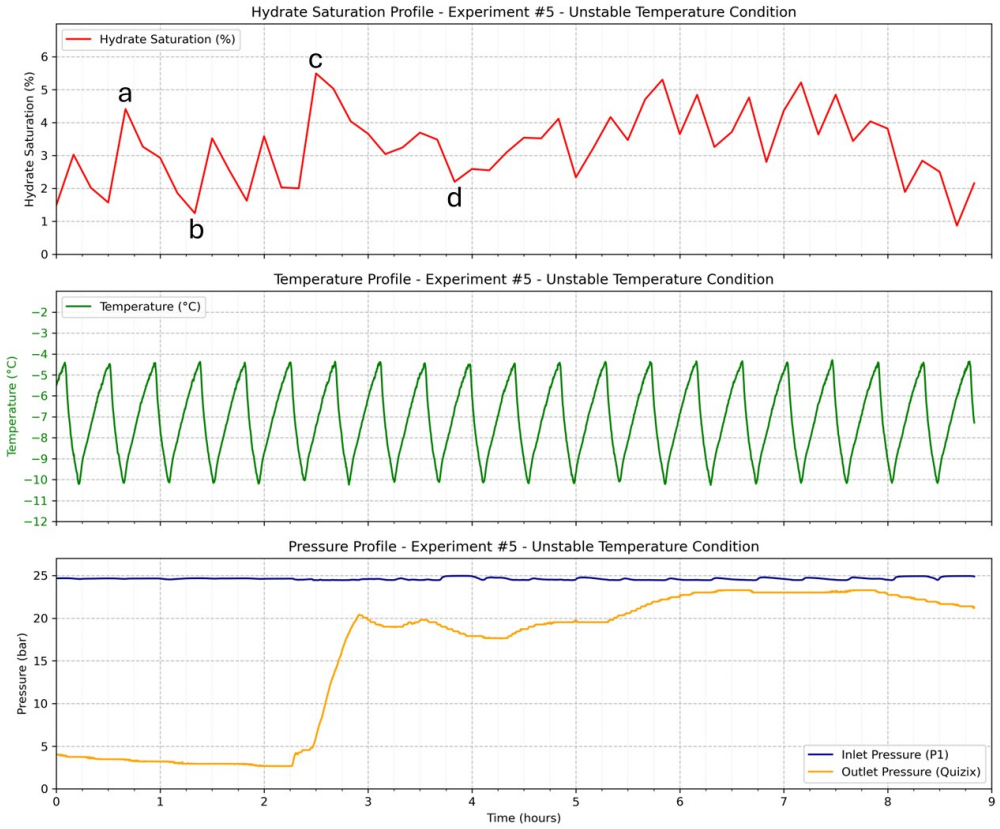

Figure 4.37: Hydrate saturation, pressure, and temperature profiles during significant temperature fluctuation in the second stage of Experiment #5.

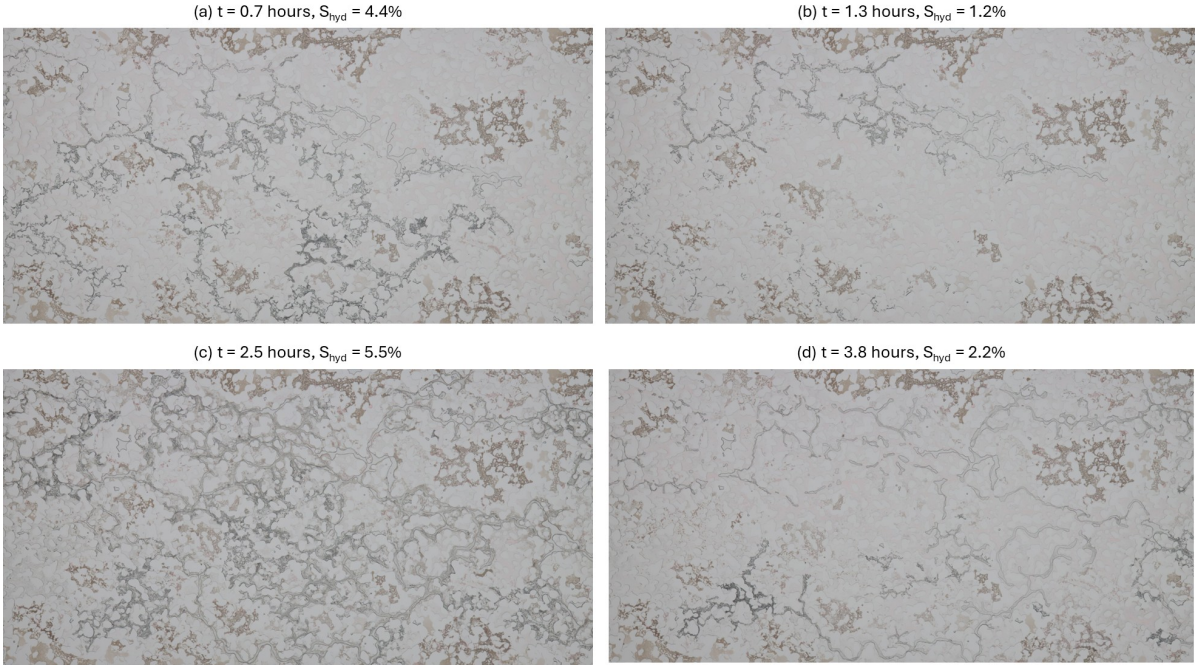

Figure 4.38: Visualization of hydrate formation and dissociation during significant temperature fluctuation in the second stage of Experiment #5.

CO_2 Hydrate Behaviour during Stable Temperature Conditions

To investigate CO_2 hydrate behavior under thermally stable conditions, the experimental setup was adjusted to minimize temperature fluctuations by fine-tuning the cooling system. This adjustment successfully maintained the temperature at approximately -5 °C throughout the monitoring period.

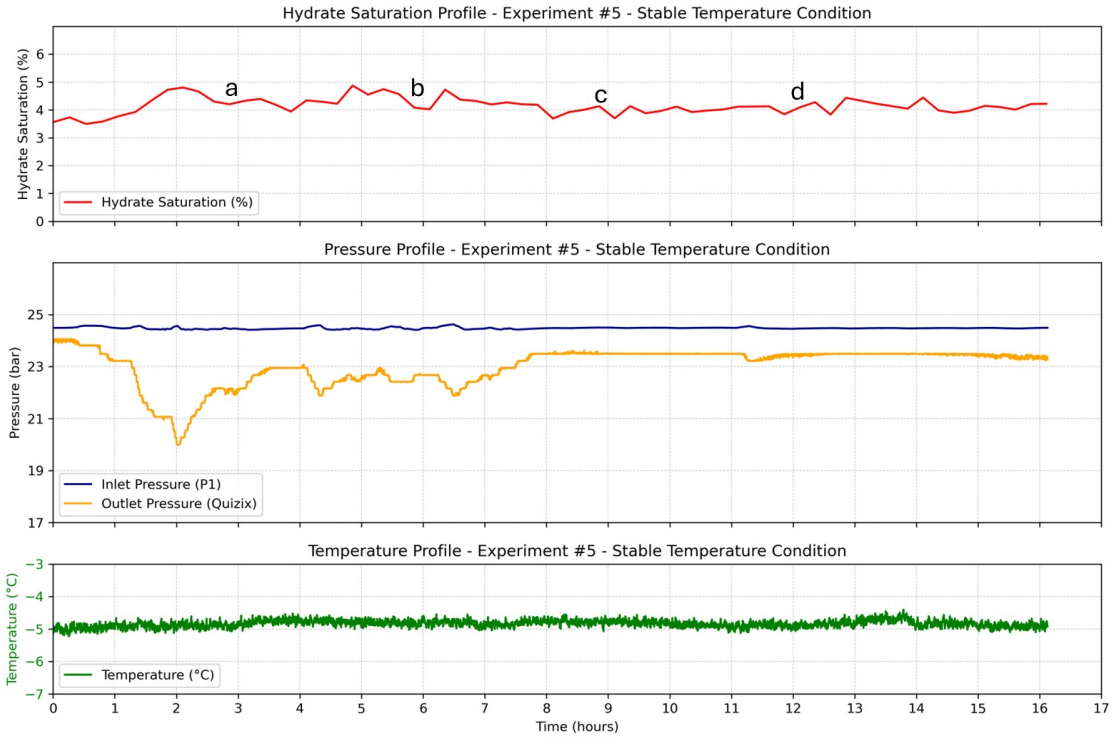

Figure 4.39: Hydrate saturation, pressure, and temperature profiles during stable temperature conditions in the second stage of Experiment #5.

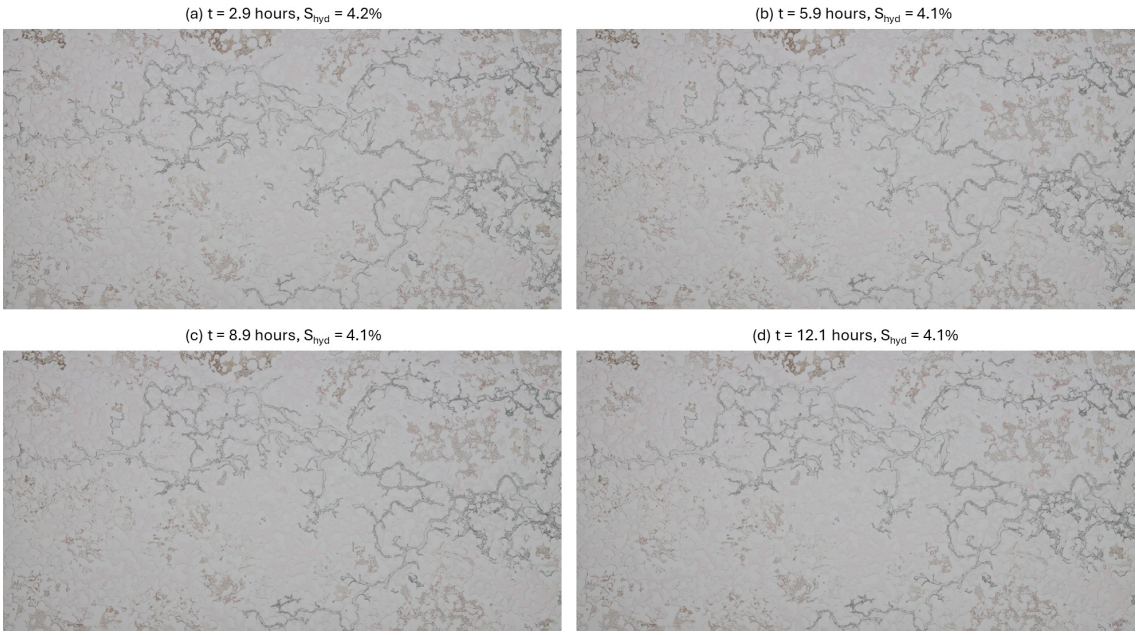

Figure 4.40: Visualization of the hydrate distribution in the micromodel under stable temperature conditions in the second stage of Experiment #5.

Figure 4.39 displays the hydrate saturation, pressure, and temperature profiles during this stable phase. Under these controlled thermal conditions, hydrate saturation remained relatively constant at around 4%. Additionally, the pressure differential between the inlet and outlet was significantly lower than that observed during temperature-fluctuating periods.

Figure 4.40 provides visual confirmation of the hydrate phase distribution within the micromodel under stable temperature. The hydrate phase remained spatially consistent, with no significant signs of new nucleation or dissociation events.

Since calculating water saturation directly was challenging, the water saturation during the experiment was estimated using the calculation for emulsion saturation. Given that the oil-to-water ratio (OWR) in the emulsion was 50:50, the water saturation was assumed to be similar to the saturation of emulsion and oil. Under stable temperature conditions, the water saturation was approximately 9%, and the conversion factor ranged from 14% to 17%.

CO_2 Hydrate Dissociation Stage

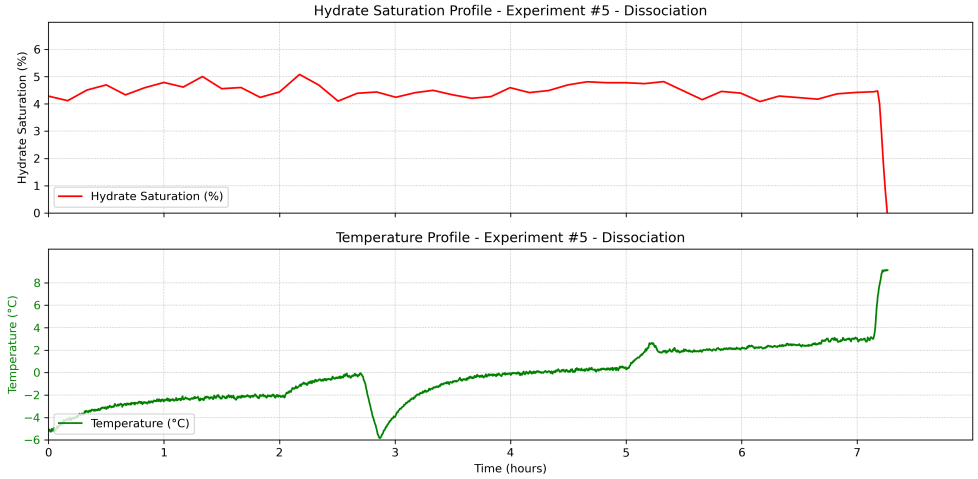

Figure 4.41: Hydrate saturation and temperature profiles during the dissociation process in the second stage of Experiment #5.

Following 17 hours of hydrate monitoring under stable thermal conditions, the dissociation phase was initiated. Dissociation was induced by incrementally increasing the temperature from -5 °C to 9 °C while maintaining a constant pressure of 25 bars, as illustrated in Figure 4.41.

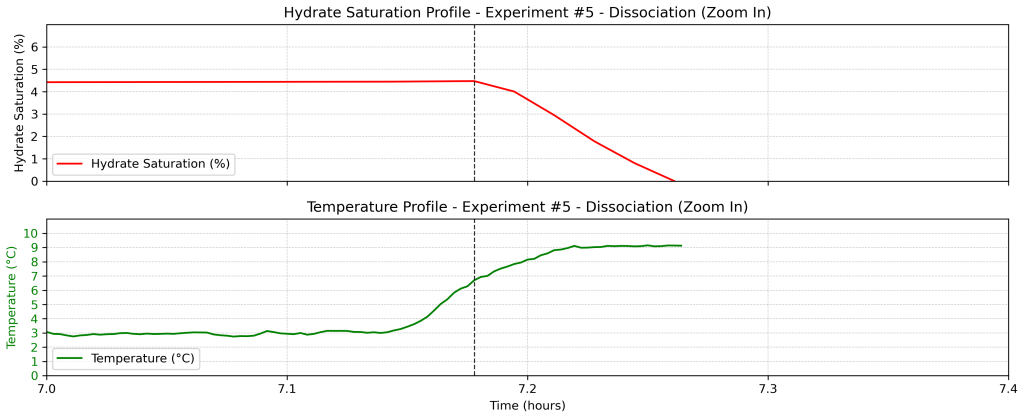

Figure 4.42: Zoomed-in view of hydrate saturation and temperature profiles during the dissociation process in the second stage of Experiment #5.

As shown in Figure 4.42, hydrate dissociation began at approximately 6.9 °C and the hydrate was fully dissociated at 9 °C. This temperature is significantly higher than the expected dissociation temperature for hydrates formed solely from $CaCl_2$-15wt%. The elevated dissociation temperature may be attributed to two key factors: (1) partial dilution of the emulsion phase by NaCl-1wt% brine introduced during the earlier stage, and (2) the presence of oil surrounding the hydrate. The presence of oil increased the dissociation temperature.

4.6. Summary of Micromodel Experiments Results

Table 4.1 provides a summary of the micromodel experiment results, highlighting the key observations from each test.

Table 4.1: Summary of the Micromodel Experiment Results

No	Experiment	Pressure Pulse	S_w	S_{hyd}	Conversion Factor	Hydrate Morphology	Max Delta Pressure	Equilibrium Temp (Ref. Literature)	Dissociation Temp (Experiment)
#1	NaCl-1wt%	0.3 sec	20%	7 - 8%	18 - 20%	Grain coating	Low (negligible)	5.6 °C	3 – 5.8 °C
#2	$CaCl_2$-15wt%	N/A	48%	1 – 10% (stable at 1%)	1.4 – 11.5%	Sheet-like, pore-filling, load-bearing, patchy, grain coating	3 bars	-1 °C	-4 – 1 °C
#3	NaCl-1wt% + Dodecane	0.3 sec	Before pulse : 15-17% After pulse 6-8%	1 – 11% (stable at 7%)	28 – 36%	Hydrate inside the CO_2 channel, grain-coating, pore-filling	12 bars	5.6 °C	5.1 – 5.6 °C
#4	$CaCl_2$-15wt% + Dodecane	0.2 – 0.5 sec	Before pulse : 41% After pulse : 21%	-	0	No hydrate	Negligible	-1 °C	Heating up to 9 °C, No dissociation
#5a	NaCl-1wt% + Emulsion (1st stage : to evaluate free water)	0.2 sec	Very low (~5%)	-	0	No hydrate	Negligible	-1 °C	Heating was not performed
#5b	NaCl-1wt% + Emulsion (2nd stage : to evaluate emulsion)	N/A	OWR 50:50 (Sw ~9%)	2 – 5% (temperature fluctuates) 4 – 5% (stable temperature)	14-17%	Hydrate inside the CO_2 channel, patchy, pore-filling	22 bars (temperature fluctuates) 5 bars (stable temperature)	-1 °C (ref. $CaCl_2$-15wt%) 5.6 °C (ref. NaCl-1wt%)	6.9 – 9 °C

5

Coupled Wellbore–Reservoir Simulation Results

The purpose of the simulations are to analyze the impact of the permeability of the damaged zone (K_d) and the radius of the damaged zone (R_d) on the pressure and temperature in the near-wellbore region and the associated risk of CO_2 hydrate formation. As a base case, the reservoir condition without any formation damage is analyzed. Sensitivity analyses are then performed to evaluate the effects of varying K_d and R_d values. Damaged permeability values of $K_d = 0.7K_0$ and $0.4K_0$ is used to represent permeability impairment caused by drilling mud–induced formation damage. Furthermore, since the formation of CO_2 hydrate could cause additional damage, lower values of $K_d = 0.2K_0$ and $0.1K_0$ are also applied in the simulations. For the radius of the damaged zone (R_d), the sensitivity analysis is performed using values of 0.5 m, 1 m, 3 m, and 5 m.

The results are presented in three parts. First, the wellbore simulation results are analyzed, with a focus on parameters that influence bottom-hole conditions. Second, the reservoir behavior is evaluated, particularly the effects of pressure and temperature changes resulting from CO_2 injection. Finally, a hydrate risk analysis is conducted using a phase diagram approach to assess the potential for CO_2 hydrate formation. The hydrate equilibrium lines (HEL) for NaCl–1wt% and $CaCl_2$–15 wt% were used to represent the reservoir fluid and the dispersed fluid in the W/O emulsion (OBM filtrate), respectively, as also used in the micromodel experiments. The HEL used in this study refer to hydraflash simulation as reported by M. Aghajanloo et al. (2024).

5.1. Base Case Analysis

This section analyzes the base case simulation response of the coupled wellbore-reservoir model without any damage to the wellbore zone.

5.1.1. Wellbore Analysis

Figure 5.1 presents pressure, temperature, CO_2 gas saturation, and CO_2 gas density profiles along the wellbore during the early stage of CO_2 injection, illustrating transient behavior during the startup phase. Figure 5.2 – Figure 5.5 show line plots of the evolution of these parameters along the wellbore (left panels), and their respective values at the bottom hole (right panels), which serve as the input and feedback for reservoir simulation.

Initially, the wellbore is filled with 100% CO_2 gas, with a wellhead pressure of 14.7 bars. When CO_2 is injected in the liquid phase at 100 bars and 15 °C, rapid expansion causes phase change and significant Joule-Thomson (JT) cooling. As injection starts, pressure increases along the entire wellbore, while the upper section experiences intense cooling, with temperature dropping below -20 °C due to the extreme pressure drop between the wellhead and the wellbore, which is associated with expansion.

CO_2 reaches the bottom hole at approximately t = 300 seconds ($\sim 3 \times 10^{-3}$ days). Upon reaching the

reservoir interface, a flow regime transition occurs, causing compression and thus increasing bottom hole pressure and temperature. At this stage, the fluid in the wellbore is predominantly in a two-phase CO_2 system, while the fluid in the bottom hole is in single-phase gas.

Subsequently, as CO_2 enters the reservoir, cooling occurs and the bottom hole temperature gradually stabilizes around t $\approx$ 0.03 days ($\sim$ 2600 seconds), as illustrated in Figure 5.1 and Figure 5.3. This results in a phase transition and a drop in gas saturation, as shown in Figure 5.4.

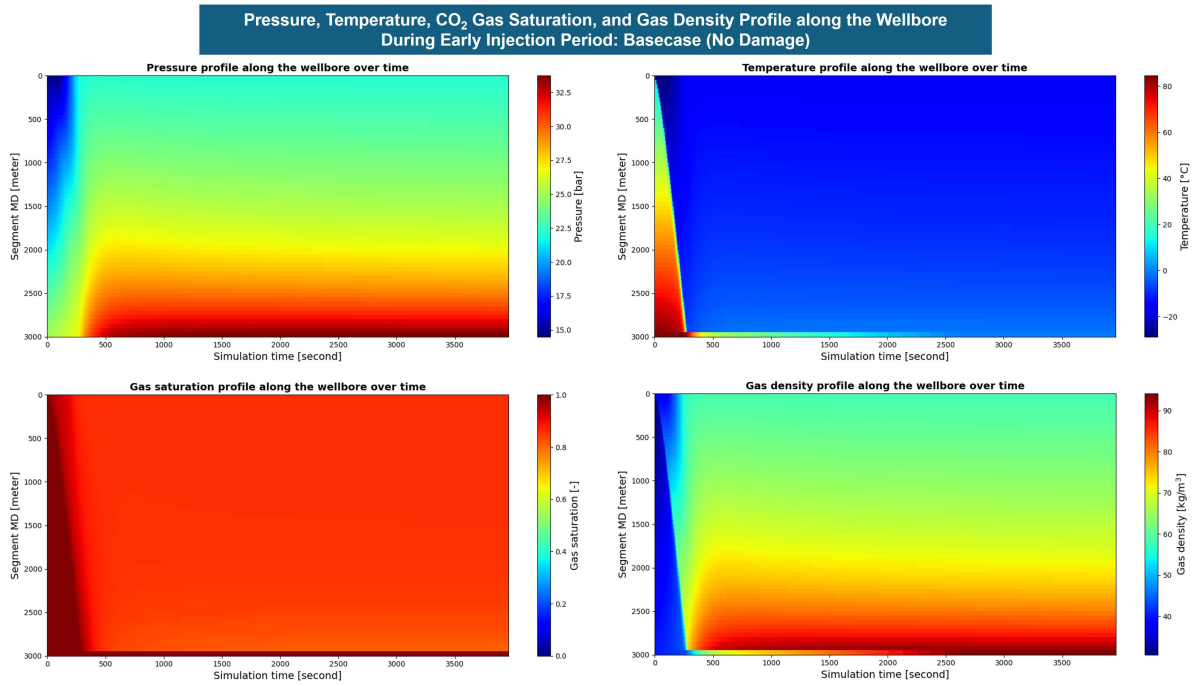

Figure 5.1: Pressure, temperature, CO_2 gas saturation, and CO_2 gas density profiles along the wellbore during early CO_2 injection, visualized as heat maps.

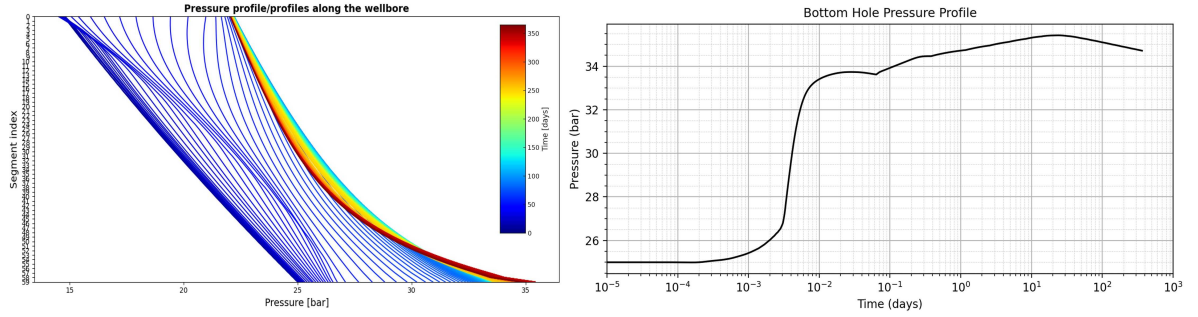

Figure 5.2: Pressure profile along the wellbore over time.

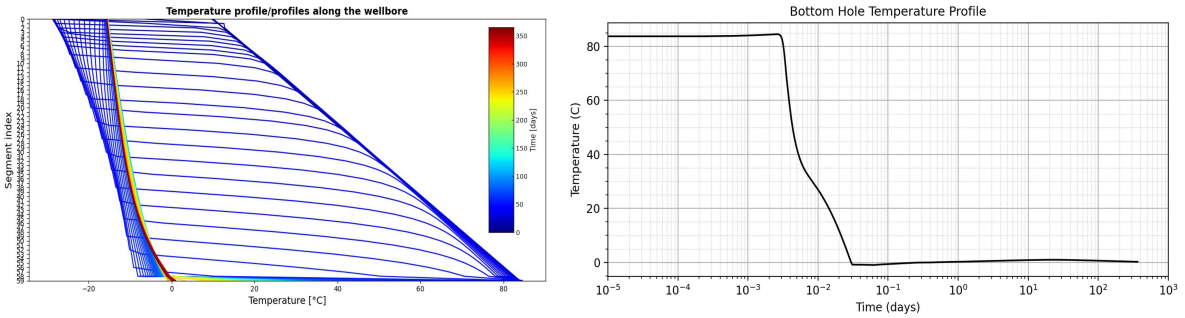

Figure 5.3: Temperature profile along the wellbore over time.

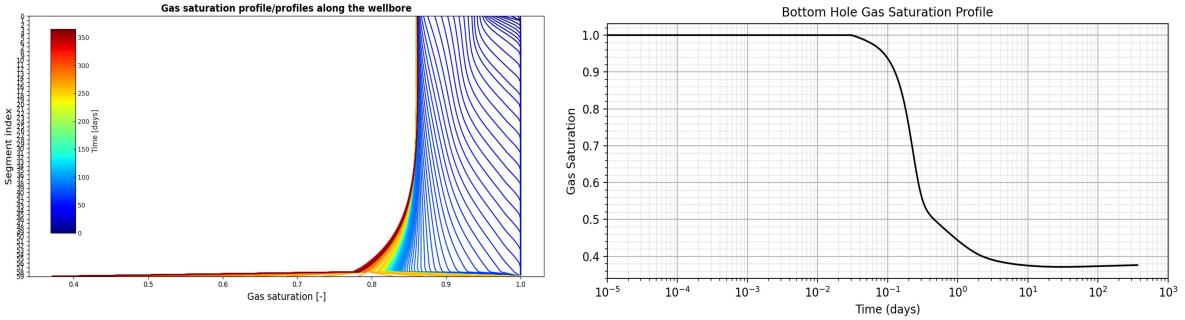

Figure 5.4: CO_2 gas saturation profile along the wellbore over time.

Over time, bottom hole pressure increases due to reservoir pressurization by the CO_2 injection in the reservoir. After approximately 20 days, the bottom hole pressure begins to decline, likely due to changes in fluid properties and reservoir behavior, as indicated by the evolution of gas density at the bottom hole in Figure 5.5.

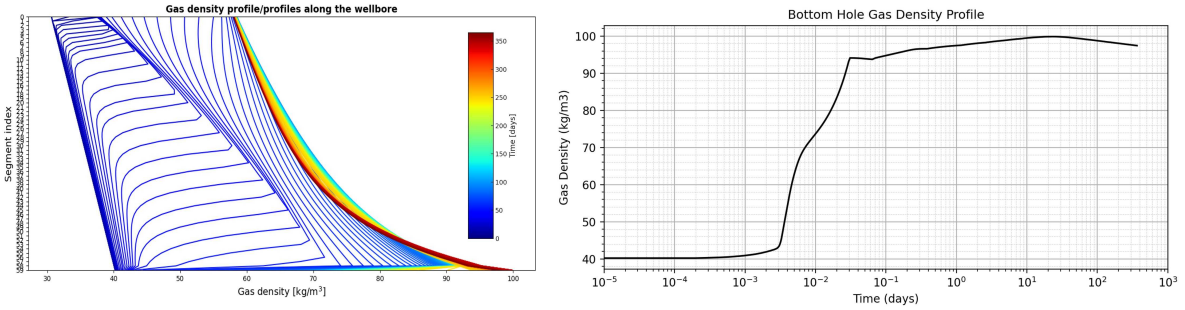

Figure 5.5: CO_2 gas density profile along the wellbore over time.

5.1.2. Reservoir Analysis

Figure 5.6 shows the temperature and pressure profiles in the reservoir at four different time steps: 10 days, 30 days, 100 days, and 365 days after CO_2 injection. Meanwhile, Figure 5.7 presents the corresponding profiles of gas saturation and liquid saturation along the reservoir.

As shown in Figure 5.6, a cooling effect is observed in the near-wellbore region. Over time, the cooling front propagates further into the reservoir and becomes more pronounced, indicating increasing thermal penetration. Pressure near the wellbore also changes over time, especially within the first 10 meters from the well, due to variations in bottom-hole pressure and CO_2 fluid density, as previously described in Figure 5.2. At t = 10 days, the bottom-hole pressure is 35.2 bars. By t = 30 days, the bottom-hole pressure increases slightly by approximately 0.1 bars. At a radius of 2.5 meters, the pressure difference

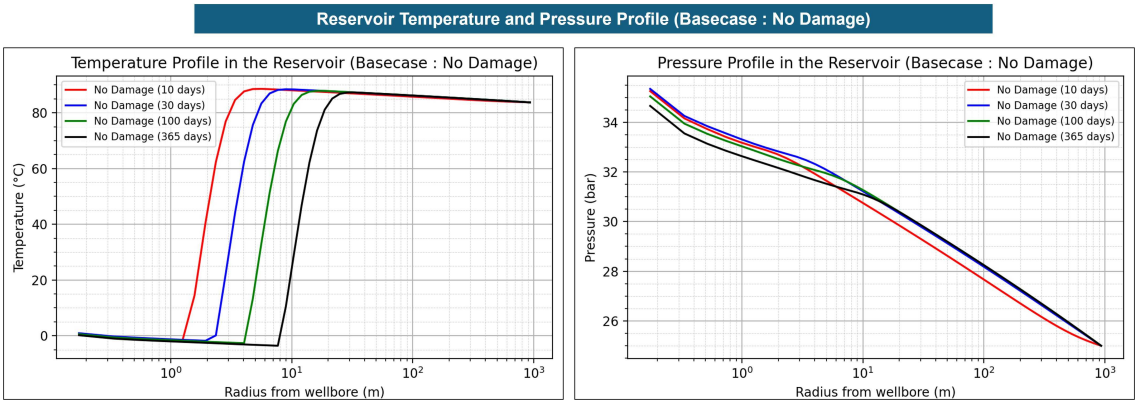

Figure 5.6: Temperature and pressure profiles in the reservoir at t = 10, 30, 100, and 365 days.

between t = 10 days and t = 30 days becomes more pronounced. Subsequently, at t = 100 days, the pressure drops below the previous time step, and by t = 365 days, the pressure in the near-wellbore region further decreases.

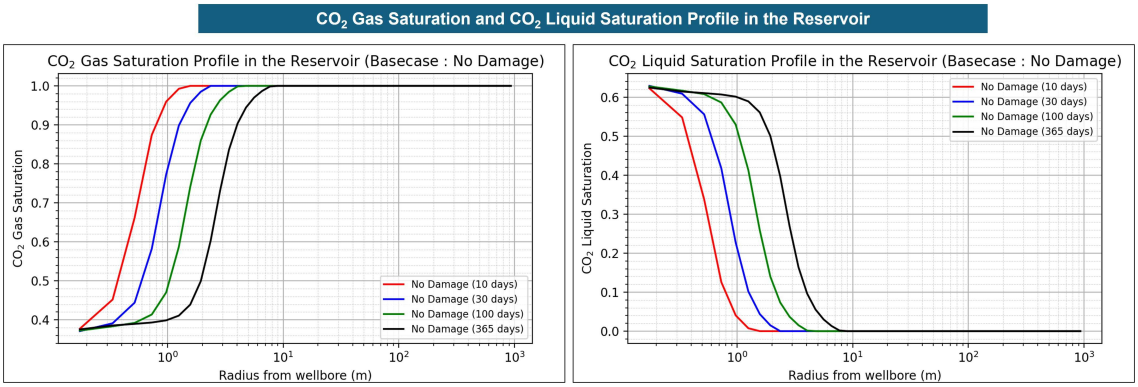

Figure 5.7: Gas saturation and CO_2 liquid saturation profiles in the reservoir at t = 10, 30, 100, and 365 days.

In contrast, in the far-field region, pressure increases from day 10 to day 30, then stabilizes. Beyond 30 days, there is no significant change in pressure at the outer boundary (radius = 1000 m), indicating the system has reached a pseudo-steady-state regime. This is consistent with the assumption of an infinite reservoir, where the pressure at the outermost boundary remains constant at 25 bars.

Over time, the CO_2 liquid saturation near the wellbore increases, and the two-phase flow zone expands radially outward. This transition from single-phase to two-phase flow becomes more dominant in the near-wellbore region and progresses further into the reservoir, as illustrated in Figure 5.7. The formation of two-phase flow is driven by the thermodynamic conditions caused by pressure and temperature changes, resulting in partial condensation of injected CO_2.

Figure 5.8 provides a 3D visualization of temperature, pressure, and CO_2 liquid saturation distributions at t = 365 days. The cooling effect and the presence of CO_2 liquid are concentrated near the wellbore. This visual representation confirms that thermal and phase behavior changes due to CO_2 injection are spatially localized around the injection point. This finding highlights the importance of evaluating near-wellbore fluid (mud filtrate) and formation damage when assessing the risk of CO_2 hydrate formation in depleted reservoirs.

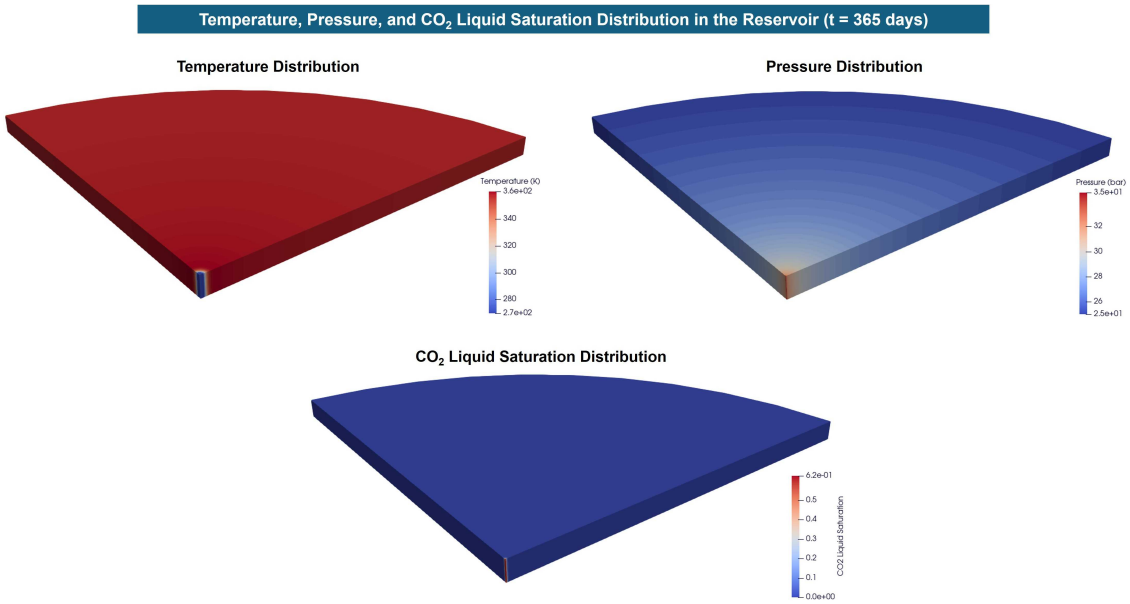

Figure 5.8: 3D visualization of temperature, pressure, and CO_2 liquid saturation distribution in the reservoir at t = 365 days.

5.1.3. The Risk of CO_2 Hydrate Formation

The risk of CO_2 hydrate formation is evaluated using the phase diagram approach. Figure 5.9 presents that the risk of hydrate formation in the near wellbore for the base-case scenario is high, as all of the near wellbore zone is in the hydrate stability zone. The hydrate risk is also more pronounced over time as the pressure declines in the near wellbore and the cooling propagates radially in the reservoir.

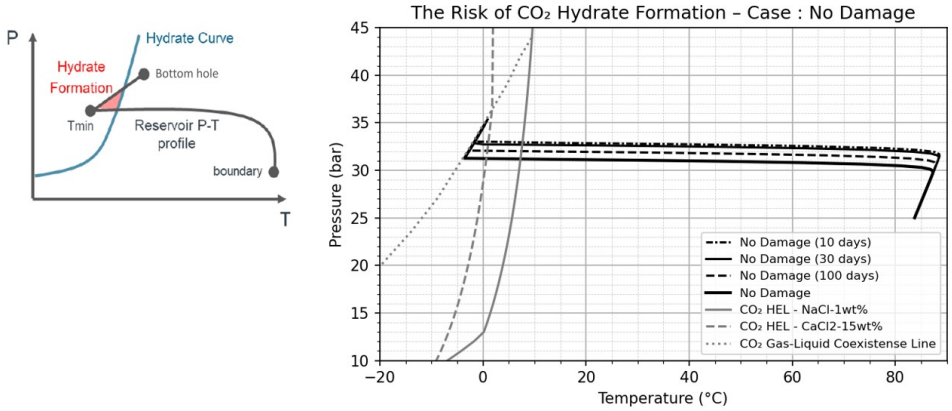

Figure 5.9: The risk of CO_2 hydrate formation - basecase (no damage)

5.2. Impact of Permeability of the Damaged-Zone (K_d)

The impact of permeability impairment is evaluated by simulating the following values of K_d.

- $K_d = 0.7K_0 = 210$ mD (low permeability impairment due to drilling mud–induced formation damage),
- $K_d = 0.4K_0 = 120$ mD (high permeability impairment due to drilling mud–induced formation damage),
- $K_d = 0.2K_0 = 60$ mD (additional damage due to hydrate formation),
- $K_d = 0.1K_0 = 30$ mD (additional damage due to hydrate formation, higher impairment).

For the K_d sensitivity analysis, the radius of damage is assumed to be $R_d = 1$ meter.

5.2.1. Wellbore Analysis

Figure 5.10 presents the bottom-hole pressure, temperature, CO_2 gas density, and CO_2 liquid saturation over time, illustrating the impact of various K_d values. It is observed that bottom-hole pressure increases as near-wellbore permeability decreases. This is because, to achieve a similar injection rate, a higher pressure is required for the fluid to enter the reservoir with lower near-wellbore permeability. As bottom-hole pressure increases, the pressure drawdown along the wellbore decreases, thereby reducing the JT cooling effect or even triggering a compression effect that causes heating.

At $t \approx 3 \times 10^{-3}$ days, when CO_2 first contacts the reservoir, a sudden increase in bottom-hole temperature occurs. This is attributed to the compression effect resulting from a sharp increase in bottom-hole pressure as CO_2 transitions from flowing through the wellbore to entering the porous medium with lower permeability. The lower the K_d value (the greater the permeability impairment), the more pronounced the heating effect at the bottom hole.

It can thus be concluded that higher permeability impairment in the near-wellbore region leads to elevated bottom-hole pressure, which subsequently induces higher bottom-hole temperature. Additionally, the higher pressure at the bottom hole increases CO_2 liquid saturation. These findings demonstrate that near-wellbore permeability damage significantly influences pressure, temperature, and phase behavior at the bottom hole.

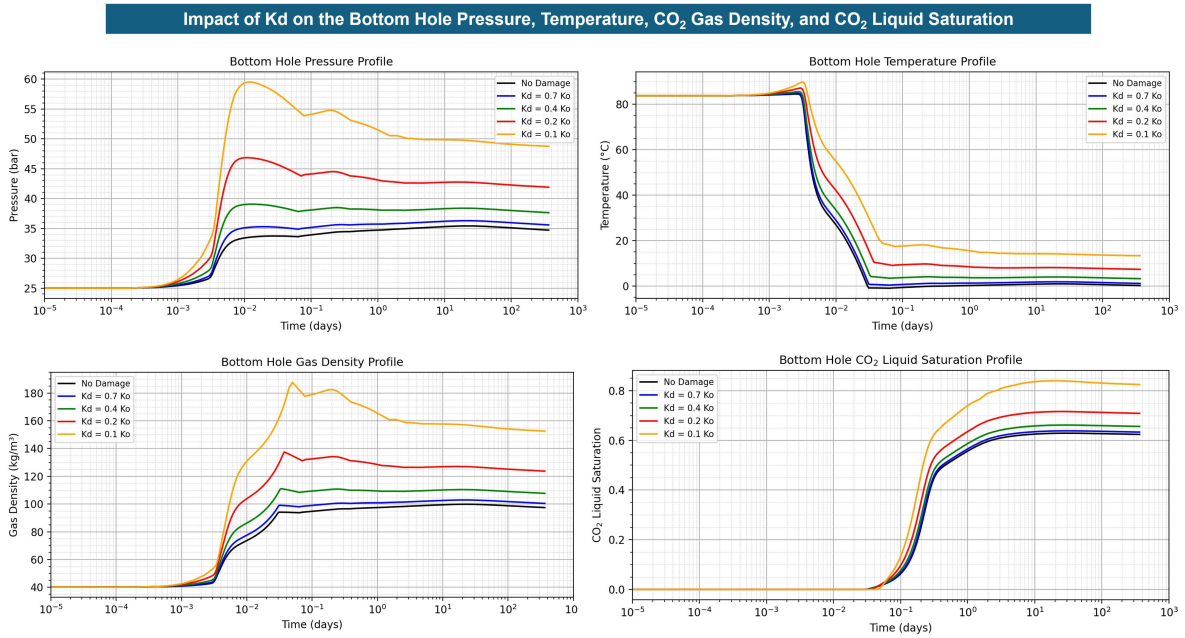

Figure 5.10: Bottom-hole pressure, temperature, CO_2 gas density, and CO_2 liquid saturation as a function of various K_d values.

5.2.2. Reservoir Analysis

Figure 5.11 demonstrates the reservoir temperature, pressure, and CO_2 liquid saturation profiles as a function of various K_d values at t = 30 and 365 days. The results confirm that lower near-wellbore permeability leads to an increase in pressure and temperature in the reservoir. This outcome arises from the coupled nature of the wellbore–reservoir simulation, where the bottomhole pressure and temperature, described in the previous section, serve as thermodynamic inputs for the reservoir model. As such, any change in wellbore conditions directly affects the near-wellbore reservoir region. Since the radius of damage is assumed to be 1 meter, the influence of pressure and temperature is primarily confined within this damaged zone.

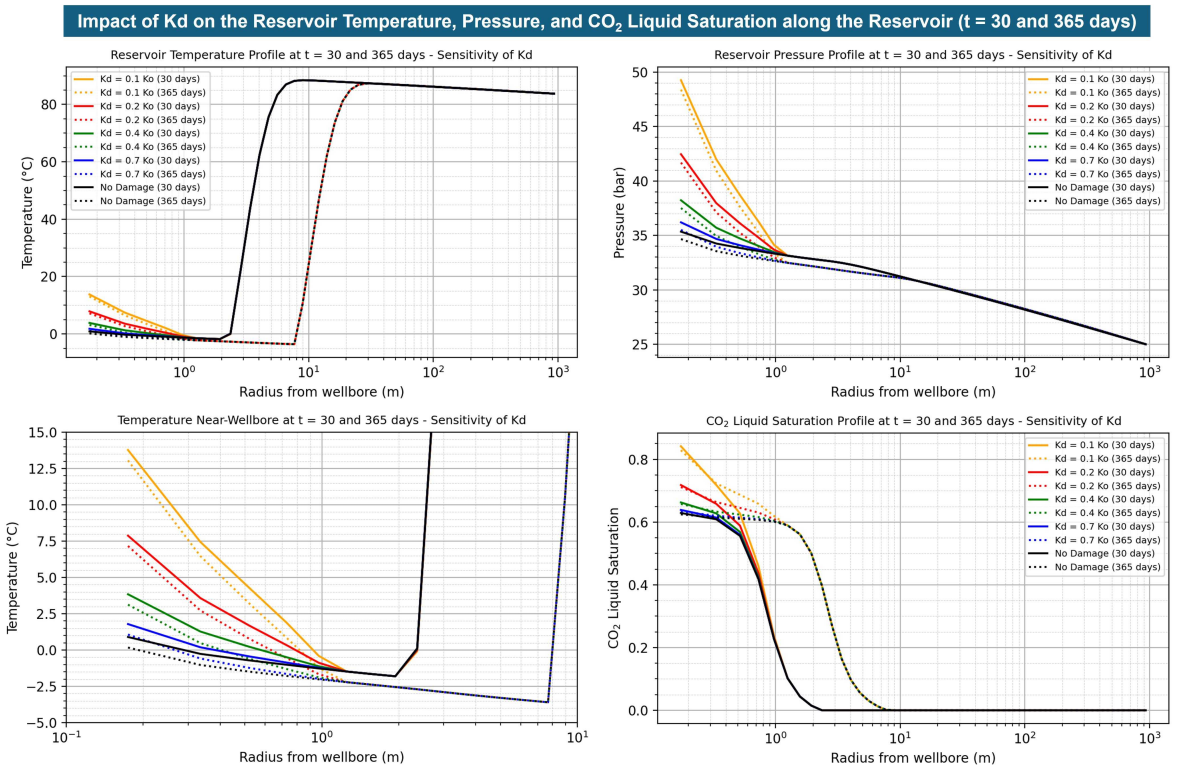

Figure 5.11: Reservoir temperature, pressure, and CO_2 liquid saturation profile along the reservoir as the impact of various K_d values at t = 30 and 365 days.

5.2.3. The Risk of CO_2 Hydrate Formation

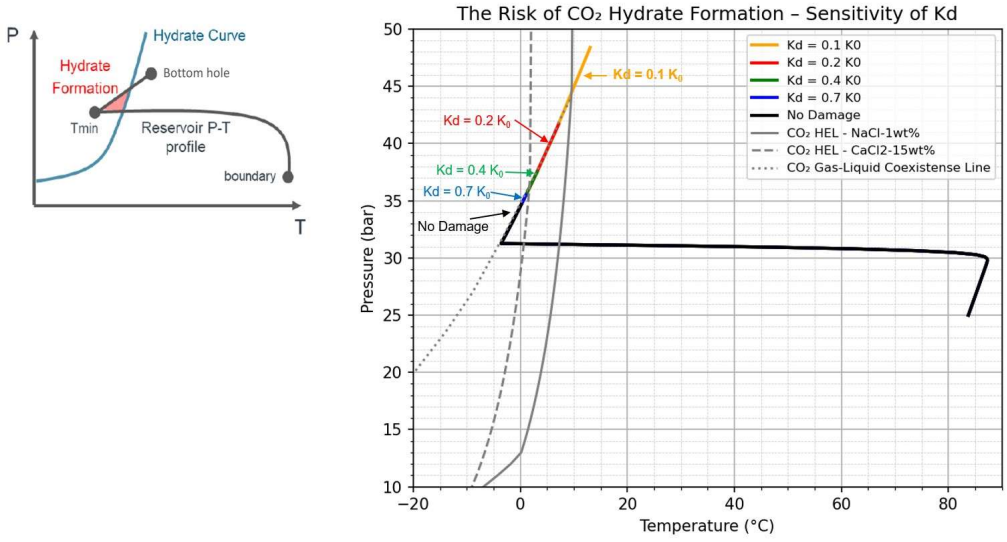

Figure 5.12: The risk of CO_2 hydrate formation as the impact of various K_d values (t = 365 days).

Figure 5.12 presents the risk of CO_2 hydrate formation for various K_d values. Under low permeability impairment conditions, such as $K_d = 0.7K_0$, the bottomhole conditions fall within the hydrate stability zones for both NaCl-1wt% and $CaCl_2$-15wt% systems, indicating a risk of hydrate formation. As the permeability impairment increases ($K_d = 0.4K_0$) and there is an additional permeability impairment due to hydrate at $K_d = 0.2K_0$, the bottomhole conditions move outside the hydrate stability zone for $CaCl_2$-15wt%, but hydrate formation remains possible if the local salinity is lower. In the case of additional permeability impairment due to severe hydrate formation ($K_d = 0.1K_0$), the bottomhole conditions are

outside the hydrate stability zone both for $CaCl_2$-15wt% and NaCl-1wt%. The detailed radial extent of the area at risk of hydrate formation is shown in Figure E.3 in Appendix E.

These results suggest that greater permeability impairment in the near-wellbore region leads to lower hydrate formation risk, due to the associated increase in bottomhole pressure and temperature, which shifts the thermodynamic state away from the hydrate stability zone.

5.3. Impact of Radius of the Damaged-Zone (R_d)

To examine the effect of the radius of the damage zone, the following values of R_d are tested:

- R_d = 0.5 m (shallow invasion),
- R_d = 1 m (medium invasion),
- R_d = 3 m (deep invasion),
- R_d = 5 m (extreme invasion).

In the R_d sensitivity scenarios, a constant permeability reduction of K_d = 0.4 K_0 is applied.

5.3.1. Wellbore Analysis

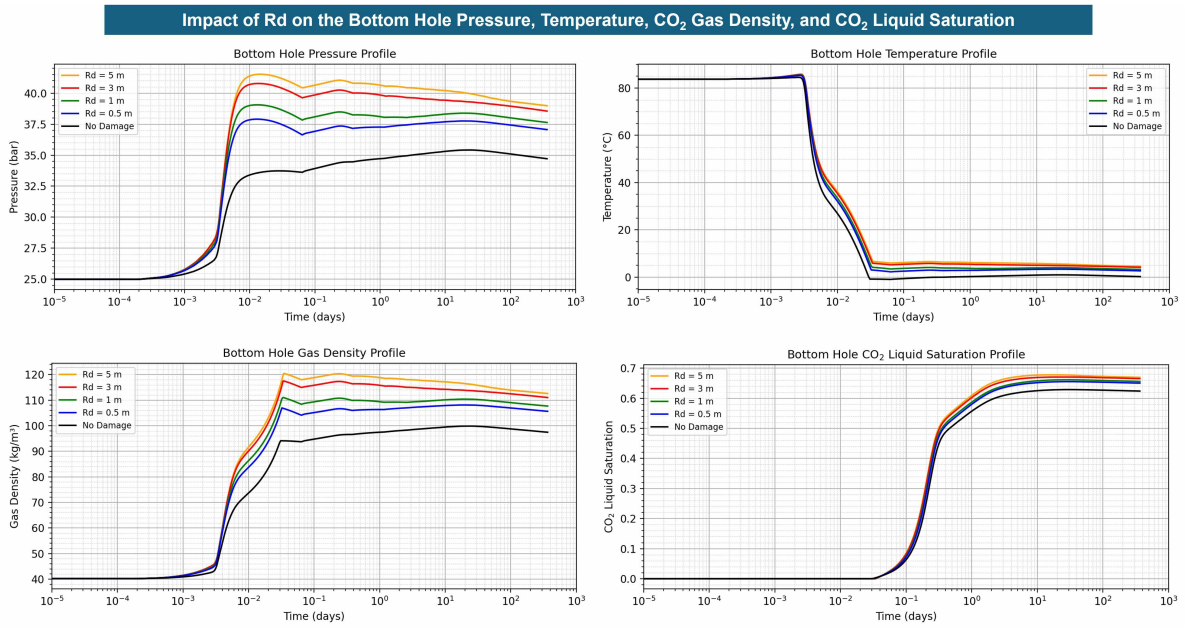

Figure 5.13: Bottom-hole pressure, temperature, CO_2 gas density, and CO_2 liquid saturation as a function of various R_d values.

Figure 5.13 displays the evolution of bottom-hole pressure, temperature, CO_2 gas density, and CO_2 liquid saturation as a function of different R_d values over time. The results indicate that increasing the radius of the damaged zone leads to a rise in bottom-hole pressure and temperature. This occurs due to the larger resistance encountered by the injected fluid, which requires higher pressure to maintain the same injection rate. Consequently, the resulting compression effect leads to elevated temperatures. Additionally, an increase in bottom-hole CO_2 liquid saturation is observed with larger R_d, consistent with the increase in bottom-hole pressure.

5.3.2. Reservoir Analysis

Figure 5.14 demonstrates the reservoir temperature, pressure, and CO_2 liquid saturation profiles for various R_d values at t = 30 and 365 days. The results indicate that a larger radius of the damaged zone leads to slightly elevated pressure and temperature in the near-wellbore region. However, the overall influence of increasing R_d is relatively modest when compared to the pronounced effects observed from permeability reduction (K_d) in the damaged zone. This suggests that while R_d contributes to reservoir

behavior, the extent of permeability impairment plays a more dominant role in governing pressure and thermal dynamics.

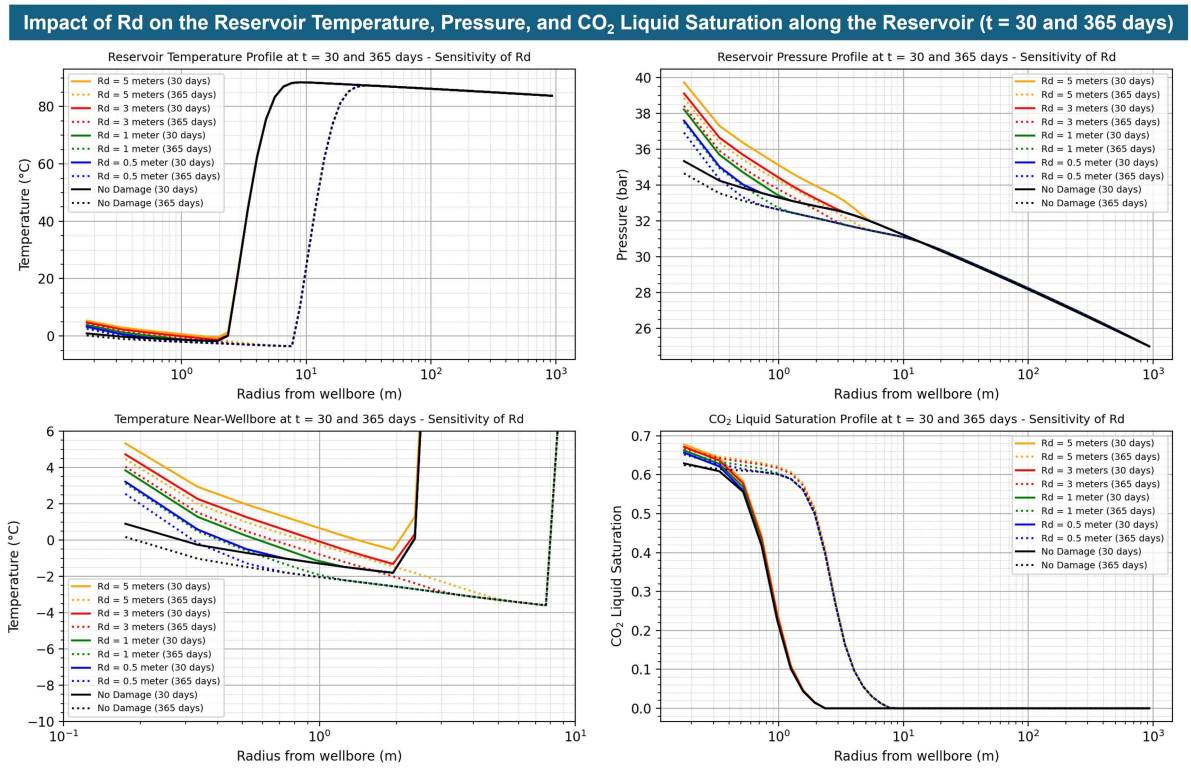

Figure 5.14: Reservoir temperature, pressure, and CO_2 liquid saturation profile along the reservoir as the impact of various R_d values at t = 30 and 365 days.

5.3.3. The Risk of CO_2 Hydrate Formation

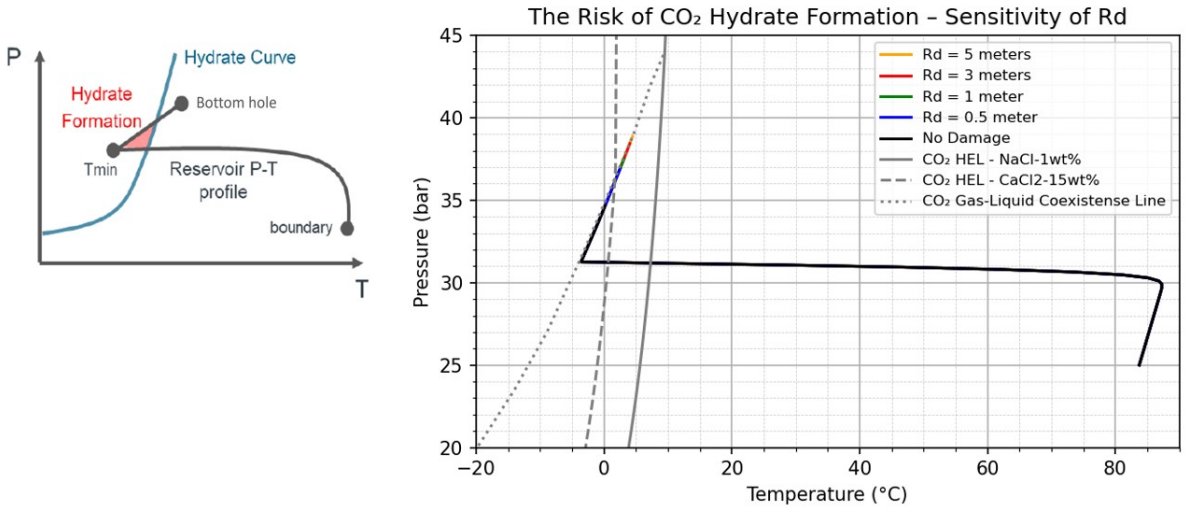

Figure 5.15: The risk of CO_2 hydrate formation as the impact of various R_d values.

Figure 5.15 illustrates the risk of CO_2 hydrate formation for various R_d values. A damage radius of 0.5 m shifted the bottomhole condition outside of the HEL for the $CaCl_2$–15wt% system. Beyond this point, increasing R_d resulted in only a modest rise in bottomhole temperature and pressure, with the magnitude of the effect remaining relatively limited. As a result, in all cases evaluated, the bottom-hole and near-wellbore conditions remain within the hydrate stability zone for NaCl-1wt%.

6

Discussions

The chapter is structured into two parts: the first part discusses the micromodel experiment results along with their limitations, and the second part presents the simulation results and their associated limitations.

6.1. Micromodel Experiments

This section is divided into three parts. The first part focuses on discussing the morphology of CO_2 hydrate in the presence of OBM filtrate components. The second part evaluates the CO_2 hydrate saturation profile influenced by each OBM filtrate component. Finally, the third part outlines the limitations of the experimental setup and image analysis.

6.1.1. CO_2 Hydrate Morphology

Based on the experiments conducted, various CO_2 hydrate morphologies previously described in the literature were observed, including grain-coating, pore-filling, load-bearing, and patchy structures. In addition to these known types, a sheet-like structure, reported by Schellart (2024) and not commonly found in earlier studies, was also clearly observed in Experiment #2.

Distinct hydrate features were identified in experiments involving oil. Unlike experiments using only water or brine, hydrate formation in the presence of oil (Experiments #3 and #5) occurred not only at the CO_2-water interface but also within the CO_2 flow pathways. These CO_2 pathways appeared noticeably narrower compared to those in oil-free systems, indicating that the presence of oil may influence both the location and confinement of hydrate growth.

In low water saturation conditions and when the water is mainly distributed along the grain edges, grain-coating morphology tends to form. This is because hydrate forms at the interface between water molecules and CO_2 gas. When water is mainly localized near grain surfaces, hydrate nucleation and growth also occur in those regions, resulting in grain-coating structures. This behavior is demonstrated in Experiment #1, as shown in Figure 4.2 and Figure 4.4.

In Experiment #2, where water was well distributed throughout the pore space and the overall water saturation was relatively high, hydrate formation exhibited a wider range of morphologies, including grain-coating, pore-filling, load-bearing, patchy, and sheet-like structures. In Experiment #5, a relatively high water-oil ratio (WOR) of 50:50 led to significant water droplet coalescence. As a result, water saturation became relatively high, and the coalesced droplets were distributed within the pore space. This condition also promoted the formation of pore-filling and patchy hydrate morphologies in certain regions.

In addition to findings on the hydrate morphological type, the experiment shows that the type of hydrate morphology influences permeability impairment. The pressure difference between the inlet and outlet indicates permeability impairment. A higher pressure difference means that the hydrate causes greater permeability reduction. The results of the experiments align well with the understanding that pore-filling

hydrates have a higher impact on permeability impairment compared to grain-coating types. However, as a limitation of the experiments, the pressure difference might not only be caused by the hydrate clogging in the micromodel, but also by hydrate blockage in the tubing line of the system, which could not be visibly observed during the experiment.

In Experiment #1, even though the hydrate saturation was around 7–8%, the inlet and outlet pressures were nearly identical at approximately 25 bar, indicating a negligible pressure difference and low permeability impairment. In contrast, during early hydrate formation in Experiment #2, where the dominant hydrate morphologies were pore-filling and patchy, and the hydrate saturation was around 2–10%, the pressure difference reached approximately 1–3 bar, indicating that the permeability reduction is higher in the pore-filling type even with lower hydrate saturation.

In the experiment with oil, such as Experiment #3 and #5, the pressure difference was influenced not only by the typical morphology of the hydrate, but also by the connectivity of the CO_2 channel, as shown in Figure 4.17 and Figure 4.18. In Experiment #3, during the first 5.8 hours of hydrate formation, hydrate saturation gradually increased to approximately 7–8%, with the hydrate morphology mainly observed inside the CO_2 pathway and only a small amount of pore-filling and patchy types. This growth was also accompanied by poor connectivity of the CO_2 pathway from inlet to outlet. This combination of hydrate formation inside the CO_2 pathway and poor connectivity led to a high pressure difference, reaching up to 14 bar. However, after $t \approx 6$ hours, when the well CO_2 connectivity was established, the pressure difference decreased, even though the hydrate saturation remained stable at 7%.

In Experiment #5, the typical hydrate morphology was mainly hydrate formed inside the CO_2 channels, with some pore-filling and patchy types observed in certain areas. Poor connectivity of the CO_2 channels was also evident. This combination of hydrate forming inside the CO_2 pathway, the presence of pore-filling and patchy morphology, and limited CO_2 channel connectivity led to a high pressure difference across the micromodel.

6.1.2. CO_2 Hydrate Saturation Profile in the Presence of OBM Filtrate and Its Main Components

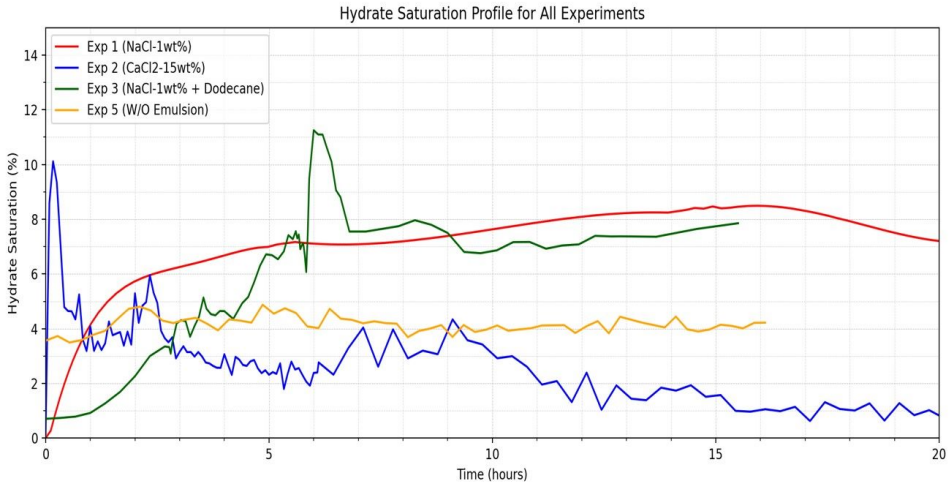

Figure 6.1: Hydrate saturation profile for all experiments

Figure 6.1 and Table 6.1 compare hydrate saturation and conversion factor across all experiments and show that high-salinity $CaCl_2$–15wt% consistently reduced both hydrate saturation and conversion efficiency. With NaCl–1wt% (Experiment #1), hydrate saturation stabilized at 7–8% despite low water saturation (20%), with a conversion efficiency of around 18–20%. The addition of dodecane (Experiment #3) maintained similarly high hydrate saturation (7.1–11.7%) but yielded a higher conversion factor of 28–36%. In contrast, in the experiment which only used $CaCl_2$–15wt% (Experiment #2) produced only 1% hydrate saturation despite 48% water saturation, with a conversion efficiency of just 1.4% under stable conditions. Furthermore, no hydrate formation was observed in Experiment #4, where $CaCl_2$–15wt% was present in the system along with dodecane. These results reflect the strong

Table 6.1: Summary of conversion factor for all experiments.

Experiment	Sw (max)	Hydrate Saturation		Conversion Factor	
		max	stable	max	stable
Exp 1 (NaCl-1wt%)	20%	8.5%	7 – 8 %	20%	18 - 20%
Exp 2 ($CaCl_2$-15wt%)	48%	10.1%	1.2%	11.5%	1.4%
Exp 3 (NaCl-1wt% + Dodecane)	8%	11.7%	7.1%	36.0%	28.0%
Exp 4 ($CaCl_2$-15wt% + Dodecane)	21%	0	0	0	0
Exp 5 (W/O Emulsion)	9%	4.8%	4.1%	17%	14-17%

inhibitory effect of high-salinity $CaCl_2$–15wt%, which reduces water activity and disrupts the hydrogen bonding necessary for hydrate cage formation, with its divalent ions exerting a stronger effect than NaCl (Mahnaz Aghajanloo, Lifei Yan, et al., 2024; M. Aghajanloo et al., 2024; Esfahani, 2023).

In Experiment #5, where a W/O emulsion was present, the hydrate saturation and conversion factor were higher than in the $CaCl_2$–15wt%–only system (Experiment #2) but lower than in the NaCl–1wt% + dodecane system (Experiment #3). This indicates that $CaCl_2$–15wt% still reduced both hydrate saturation and conversion efficiency in the W/O emulsion. However, in the W/O emulsion system, hydrate formation occurred when water coalescence exists, which increased the water-CO_2 contact area. As a result, the hydrate saturation in Experiment #5 was higher than in both Experiment #2 ($CaCl_2$–15wt% only) and Experiment #4 ($CaCl_2$–15wt% + dodecane).

Regarding the hydrate stability, hydrate saturation was relatively stable in Experiment #1, whereas it was notably unstable during the early stages of hydrate formation in Experiment #2. This instability suggests that higher salinity reduces the stability of hydrate formation, particularly in systems with high concentrations of $CaCl_2$. Ion pairing above 10wt% in such systems lowers water activity, hinders the hydration process, and may even promote local dissociation (Lida Yan and Balasubramanian, 2023). Additionally, salt exclusion during hydrate formation can locally elevate salinity, shifting the system toward a three-phase equilibrium (gas, water, hydrate), thereby limiting further hydrate growth (You et al., 2015).

In Experiment #3, despite the low water saturation (below 20%), the hydrate saturation reached approximately 7–11%. However, the presence of oil retard the hydrate growth at the early hydrate formation. This might be because of the presence of oil limiting interaction between CO_2 and water. During Experiment #3, an oil expansion process also occurred, which shows a more complex system in the presence of oil.

In contrast, in Experiment #4, which combined dodecane with high-salinity $CaCl_2$-15wt%, no hydrate formation was observed. This absence of hydrate may be attributed to the stronger inhibitory effect of $CaCl_2$-15wt%, which likely outweighed any hydrate-promoting influence of dodecane, especially under conditions of low water saturation (21%).

6.1.3. Findings on CO_2 Hydrate Formation and Dissociation in the Presence of W/O Emulsion

Experiment #5 investigated the impact of a water-in-oil (W/O) emulsion on CO_2 hydrate formation and dissociation behaviour. The experiment was conducted in two stages. The first stage evaluated the impact of the W/O emulsion in the presence of NaCl-1wt% as the water phase in the system. The second stage focused on hydrate formation originating from the dispersed phase ($CaCl_2$-15wt%) in the emulsion. During the first stage, hydrate did not form, possibly due to the low water saturation of the NaCl-1wt%, which may have been insufficient to promote hydrate nucleation.

In the second stage, the temperature was set lower than in the first stage to ensure that the system was within the hydrate stability zone for $CaCl_2$-15wt% as the dispersed phase in the emulsion. Hydrate formation occurred after a series of processes. Upon CO_2 injection, the gas was observed to dissolve into the emulsion. The lower temperature increased CO_2 solubility in the emulsion (X. Sun et al., 2022), which gradually destabilised the emulsion structure due to changes in interfacial tension and the effects of gas solubility on droplet integrity (Galfré et al., 2011; Hu, Trusler, and Crawshaw, 2017; G. Sun et al., 2018). As a result of this destabilisation, droplet coalescence occurred (Galfré et al., 2011), increasing

the surface area of water and facilitating hydrate nucleation and growth.

The surfactant used in the W/O emulsion was Span80, which generally stabilizes the emulsion and acts as a hydrate inhibitor by preventing hydrate agglomeration (M. Li et al., 2018). However, once the emulsion broke and water droplets spread throughout the system, rapid hydrate formation occurred (M. Li et al., 2018). Under these conditions, Span80 may have acted as a hydrate promoter by facilitating hydrate agglomeration (M. Li et al., 2018).

During the second stage, permeability impairment was also significant, indicated by a pressure difference ranging from 5 to 22 bar. This impairment resulted from a combination of hydrate morphologies, including those hydrate within the CO_2 pathway, pore-filling, and patchy types. Additionally, poor connectivity of the CO_2 channel further exacerbated the permeability reduction.

It was also observed that temperature fluctuations significantly disturbed the system, leading to continuous hydrate formation and dissociation, even under conditions within the hydrate stability zone. In contrast, under stable temperature conditions, hydrate saturation remained relatively constant.

Additionally, the dissociation process revealed that the temperature required to dissociate the hydrate was higher than the typical equilibrium temperature for $CaCl_2$-15wt%. This suggests that the water-in-oil emulsion system thermodynamically promotes hydrate formation.

6.1.4. Limitations of Experimental Setup and Image Analysis

Several limitations related to the experiments were identified as outlined below:

- The initial conditions for all experiments, such as water saturation, oil saturation, and their distribution, could not be kept identical, particularly after the pressure pulse was applied, as shown in Figure 6.2. Nevertheless, analyzing the conversion factor during the experiments provides insight into the individual contribution of each component to the CO_2 hydrate saturation profile.

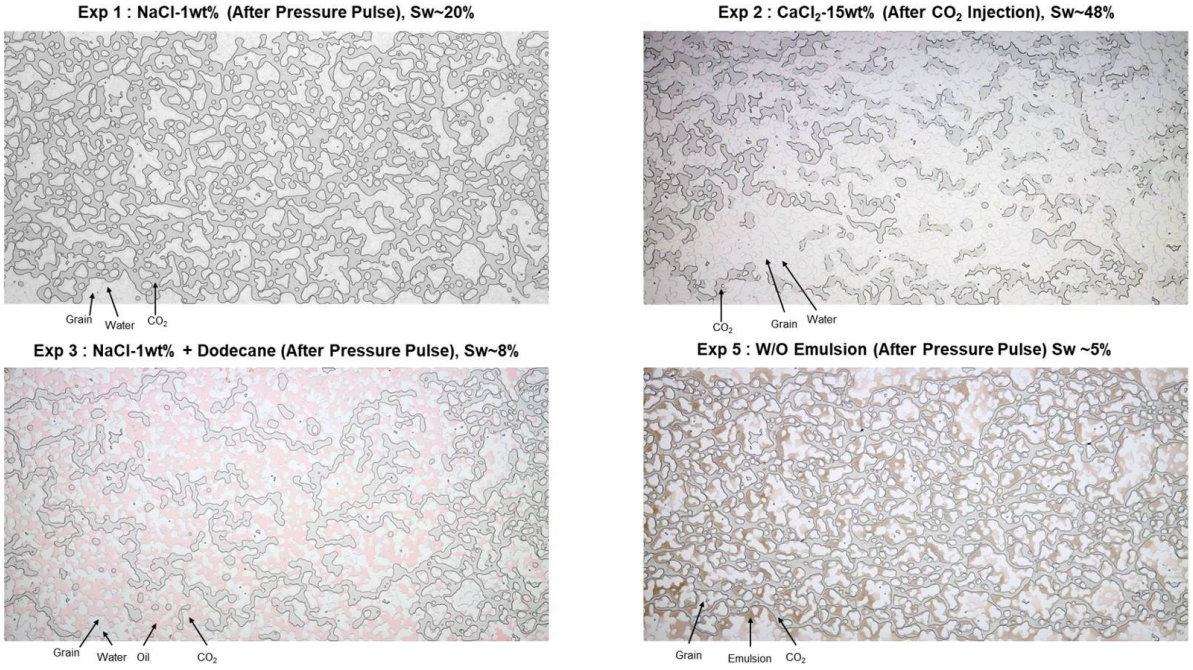

Figure 6.2: Comparison of initial condition for all experiments.

- The setup utilizes a single focal plane, assuming uniformity along the vertical axis of the chip. However, vertical heterogeneity is likely to exist, particularly in systems containing oil, where gas may stratify above oil, or in emulsions where droplet sizes are smaller than the height of the micromodel. This may lead to an inaccurate calculation of the saturation.
- Oil/emulsion and brine are injected from the outlet side of the micromodel. During the subsequent

CO_2 injection, the gas displaces fluids from the inlet line first, potentially altering the distribution of oil/emulsion and brine in the micromodel due to fluid displacement and sweeping effects.

- The CO_2 injection rate is controlled by a Quizix pump, but no flow measurement sensor is installed at the micromodel inlet. Consequently, it is not possible to quantify the amount of CO_2 consumed for hydrate formation or CO_2 dissolved into brine or oil.
- The experimental configuration adopts flow and pressure control from the downstream side using the Quizix pump. If hydrate formation or blockage in the tubing line occurs, the resulting pressure drop in the outlet may fall below the hydrate equilibrium pressure, potentially leading to unintended hydrate dissociation.
- Variations in lighting intensity were observed during hydrate formation, making image analysis more challenging and increasing the potential for calculation errors. In emulsion-based experiments, CO_2 dissolution made the emulsion appear increasingly white, making it difficult to visually distinguish between water and CO_2-rich emulsion. Furthermore, the current image acquisition and processing methods are not capable of differentiating between hydrate and salt formation.
- These micromodel experiments could not provide a quantitative measurement of permeability impairment due to their limitations, including the low pressure difference during the experiments and the potential impact of hydrate blockage in the lines, which can reduce the accuracy of permeability reduction calculations. Further research should be conducted to better quantify the effects of porosity and permeability reduction, for example by using core-flood experiments.

6.2. Coupled Wellbore–Reservoir Simulations

This section discusses the results of the coupled wellbore–reservoir simulations conducted to investigate the impact of formation damage due to OBM filtrate and CO_2 hydrate formation on the pressure and temperature in the near-wellbore in relation to the CO_2 hydrate stability zone.

Compare to only using reservoir simulation, the use of a coupled wellbore–reservoir simulation is more accurate. This coupled approach captures the dynamic interactions between the wellbore and the reservoir: changes in the wellbore directly affect bottom-hole conditions, while dynamic responses in the reservoir simultaneously serve as inputs for the wellbore. This two-way feedback mechanism enhances the reliability of the simulation results.

6.2.1. Impact of Permeability of the Damaged Zone (K_d)

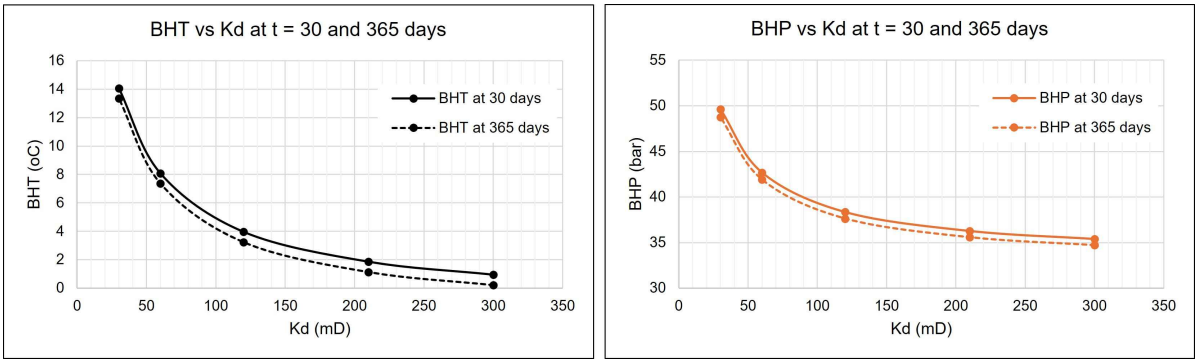

Figure 6.3: Relationship between K_d and bottom-hole pressure (BHP) and temperature (BHT)

Figure 6.3 summarizes the impact of varying K_d values on BHP BHT. It is observed that BHP increases as the permeability of the damaged zone decreases. This occurs because a lower K_d requires a greater pressure drop in the near-wellbore region to maintain the same injection rate, thereby raising the BHP.

Since the boundary condition is set in the wellhead and the wellhead injection pressure is kept constant, a higher BHP results in a smaller pressure drawdown along the wellbore. This reduced drawdown weakens the JT cooling effect, causing an increase in BHT, as illustrated in Figure 6.4. From a CO_2

hydrate risk perspective, greater formation damage may help reduce the risk of hydrate formation by elevating the temperature and pressure in the near-wellbore.

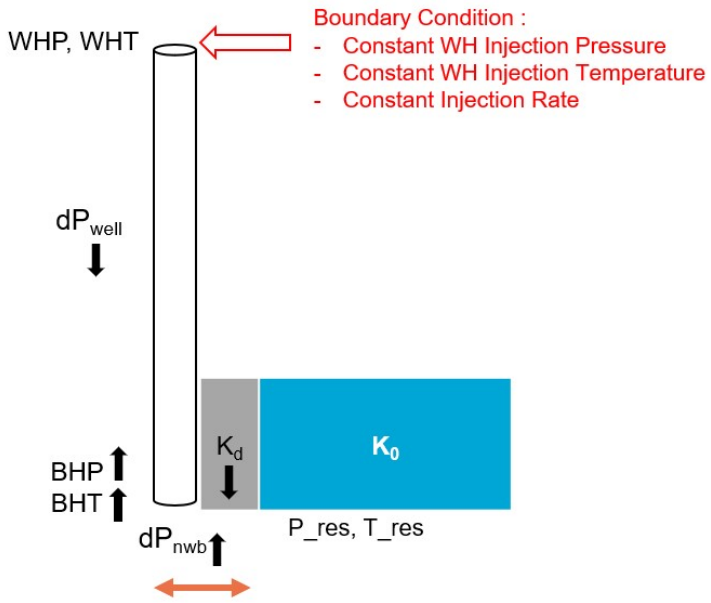

Figure 6.4: Illustration of the impact of K_d on BHP, BHT, and pressure and temperature in the the wellbore and near-wellbore

6.2.2. Impact of Radius of the Damaged-Zone (R_d)

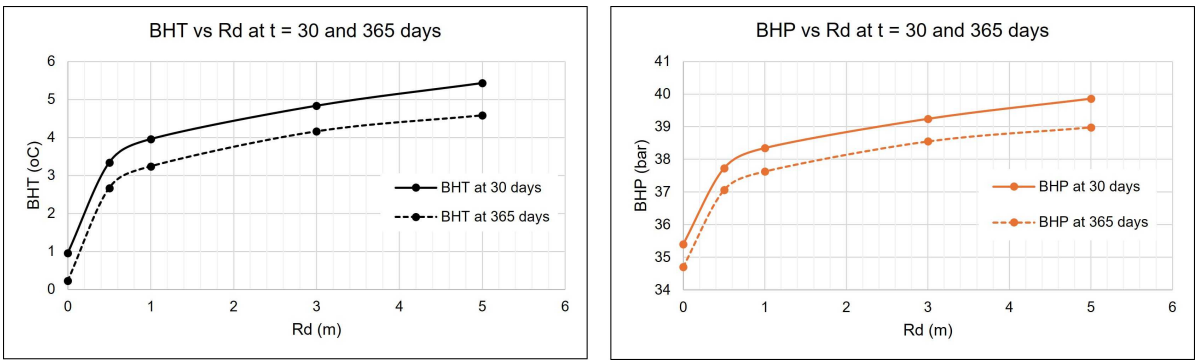

Figure 6.5: Bottom hole temperature and bottom hole pressure for varying R_d values.

Figure 6.5 provides a direct comparison of BHP and BHT at two different times (30 and 365 days) for varying R_d values. The plots show that the most significant changes in both BHP and BHT occur when R_d increases from 0 to approximately 0.5 meters. Beyond this threshold, further increases in R_d result in only marginal changes. This diminishing influence aligns with the logarithmic nature of the impact of damaged-zone radius as described by Hawkin's formula in Equation 2.3.

Compared to the impact of damaged-zone permeability, the influence of increasing R_d is relatively modest. This suggests that although R_d contributes to reservoir behavior, the severity of permeability impairment plays a more significant role in controlling bottom-hole pressure and temperature.

6.2.3. Limitations and Future Work Directions

The formation damage was represented by setting a lower permeability value in the near-wellbore, and this value of the permeability is constant over time. This was because the current simulation framework was not able to incorporate the kinetics of the hydrate formation and their direct effects on porosity and permeability changes over time. However, the simulation results offer important insights: if hydrate

formation does occur and leads to additional permeability impairment, this could result in increased bottom-hole temperatures. Such a temperature rise may help dissociate the hydrates as long as the increase is sufficient to shift the system out of the hydrate stability zone.

It is also important to note that under the current simulation parameters, the system was still able to maintain a constant injection rate despite the formation damage existing. Future studies should explore scenarios where higher formation damage might prevent the system from achieving a constant injection rate. This would allow for further analysis of how such limitations could affect bottom-hole temperature and the dynamics of hydrate formation and dissociation.

The current simulation assumed an infinite reservoir boundary. Therefore, the effect of CO_2 injection on increasing the overall reservoir pressure was not captured. Future studies should incorporate finite reservoir boundaries, as the resulting increase in reservoir pressure could influence changes in near-wellbore pressure, which, in turn, may affect near-wellbore temperature and the associated risk of hydrate formation.

7

Conclusions and Recommendations

7.1. Conclusions

This thesis successfully addressed the research questions on the impact of the synthetic OBM filtrate as the fluid/chemical component, represented by dodecane, $CaCl_2$-15wt%, and W/O emulsion, on the formation of the CO_2 hydrate in porous media, especially the hydrate morphologies and the hydrate saturation in the micromodel experiments. Subsequently, the coupled wellbore-reservoir simulations examined the impact of formation damage on the pressure and temperature in the near-wellbore in relation to the CO_2 hydrate stability zone. The conclusions of the study are summarized as follows.

Impact of the synthetic OBM filtrate as the fluid/chemical component, represented by dodecane, $CaCl_2$–15wt%, and W/O emulsion, on the formation of the CO_2 hydrate in porous media.

- The interaction between CO_2 and the synthetic OBM filtrate can potentially induce CO_2 hydrate formation under certain pressure and temperature conditions.
- Instability of the OBM filtrate emulsion during low-temperature CO_2 injection, followed by water droplet coalescence, increases the water surface area in contact with CO_2, thereby promoting hydrate formation.
- Various types of CO_2 hydrate morphologies described in the literature were observed, including grain-coating, pore-filling, load-bearing, patchy, and sheet-like structures. Furthermore, distinct hydrate features were identified in experiments involving oil and W/O emulsion, which shows that CO_2 hydrate exists not only at the CO_2-water interface but also within the CO_2 flow pathways. Additionally, these CO_2 pathways appeared narrower compared to those in oil-free systems.
- High salinity $CaCl_2$–15wt% acts as CO_2 hydrate inhibitor, which consistently reduced both hydrate saturation and conversion factor.
- Hydrate saturation in the presence of synthetic OBM filtrate is higher than hydrate saturation in the $CaCl_2$–15wt% or $CaCl_2$–15wt% + dodecane system. This was attributed to water coalescence in the W/O emulsion system, which increased the water-CO_2 contact area and facilitated hydrate nucleation.

Impact of formation damage on wellbore pressure and temperature in relation to the CO_2 hydrate stability zone.

- The coupled wellbore-reservoir simulation approach captures the dynamic interactions between the wellbore and the reservoir, enhancing the reliability of the predicted near-wellbore pressure and temperature.
- Greater formation damage may help reduce the risk of hydrate formation by incrasing the temperature and pressure in the near-wellbore.
- If hydrate formation occurs and causes additional permeability impairment, it could lead to increased bottom-hole temperatures. Such a temperature rise may help dissociate the hydrates,

provided the increase is sufficient to shift the system out of the hydrate stability zone (HSZ).

- Formation damage caused by mud-filtrate ($K_d = 0.7K_0$ and $K_d = 0.4K_0$) still keeps the pressure and temperature conditions within the hydrate stability zone. A dditional damage due to hydrate formation ($K_d = 0.2K_0$ and $K_d = 0.1K_0$) significantly increases BHP and BHT, shifting the pressure and temperature condition outside the HSZ.
- Significant changes in both BHP and BHT occur when the radius of the damaged zone (Rd) increases from 0 to approximately 0.5 meters. Beyond this threshold, further increases in Rd result in only marginal changes.

The findings provide insights to improve CCS operations in depleted reservoirs, such as using high-salinity $CaCl_2$ as the dispersed fluid in OBM to mitigate hydrate formation and exploring reversible near-wellbore reservoir damage as a means to prevent hydrates. However, further research is required to enhance the understanding of the effects of OBM filtrate and formation damage on CO_2 hydrate formation in the near-wellbore.

7.2. Recommendations for Future Research

Several recommendations are proposed for future research as follows:

- Improvements to micromodel experiments, such as:
  - Employing stereo cameras to capture multiple vertical focal planes to improve the accuracy of saturation calculations.
  - Installing a flow sensor at the inlet of the micromodel to enable quantification of CO_2 consumption and dissolution, particularly in oil-containing experiments.
  - Improving the lighting and image acquisition system to improve the quality of the data and the reliability of image analysis.
  - Repeating experiments under varying conditions to ensure robust and reproducible results.
  - Installing additional diagnostic tools, such as Raman spectroscopy, may help differentiate between hydrate and salt, especially in high-salinity brine experiments where competition between salt precipitation and hydrate formation may occur.
- Further research on the impact of OBM and formation damage on CO_2 hydrate formation, such as :
  - Conducting a series of experiments with varying oil–water ratios (OWR) to investigate how the proportion of dispersed fluid influences the hydrate formation.
  - Performing experiments with actual OBM and filtrate samples from field operations to provide more realistic insights, as field OBM systems are more chemically complex than simplified laboratory mixtures of oil, brine, and emulsion.
  - Examining the competing effects of salt-induced dry-out and hydrate formation, particularly in experiments involving high-salinity brine.
- Conducting core-scale investigations using core flooding combined with advanced imaging techniques, such as CT scanning or Magnetic Resonance Imaging (MRI), to better understand the effect of OBM on CO_2 hydrate formation in real rock samples with 3D porous structures, quantify permeability impairment, and validate numerical simulation models.
- Enhancing the coupled wellbore–reservoir simulator to incorporate CO_2 hydrate formation and dissociation through kinetic reaction modeling and to simulate their direct effects on porosity and permeability changes.
- Performing simulations with varying wellbore and reservoir parameters and different boundary conditions to obtain more robust and reliable results.

References

Aghajanloo, M. et al. (2024). “Impact of Salts on CO_2 Hydrate Saturation and Injectivity During CO_2 Storage in Depleted Gas Fields”. In: *5th EAGE Global Energy Transition Conference & Exhibition (GET 2024)*. EAGE.

Aghajanloo, Mahnaz, Sadegh M. Taghinejad, et al. (2024). “Influence of water saturation and water memory on CO_2 hydrate formation/dissociation in porous media under flowing condition”. In: *Chemical Engineering Journal* 492. DOI: 10.1016/j.cej.2024.152455.

Aghajanloo, Mahnaz, Lifei Yan, et al. (2024). “Impact of CO_2 hydrates on injectivity during CO_2 storage in depleted gas fields: A literature review”. In: *Gas Science and Engineering* 123. DOI: 10.1016/j.jgsce.2024.205250.

Baker Hughes Drilling Fluids Reference Manual (2006). Revised Edition. Internal publication. Baker Hughes Drilling Fluids. Houston, TX.

Byrne, M., R. Gilbert, and R. Anderson (2024). “Formation Damage in CO_2 Storage Wells – The Same, But Different”. In: vol. SPE International Conference and Exhibition on Formation Damage Control. SPE International Conference and Exhibition on Formation Damage Control, D011S006R002. DOI: 10.2118/217859-MS.

Dai, Meng-Ling et al. (2020). “Effect of n-dodecane on equilibrium dissociation conditions of carbon dioxide hydrate”. In: *Journal of Chemical Thermodynamics* 148, p. 106144. DOI: 10.1016/j.jct.2020.106144.

Dai, W. (2022). “Effect of Liquid Alkane on Carbon Dioxide Hydrate Formation”. In: *Journal of Molecular Liquids* 364, p. 120013. DOI: 10.1016/j.molliq.2022.120013.

Davison, J. M. et al. (2001). “Oil-Based Muds for Reservoir Drilling: Their Performance and Cleanup Characteristics”. In: *SPE Drilling & Completion* 16.02, pp. 127–134. ISSN: 1064-6671. DOI: 10.2118/72063-PA.

Davoodi, Shadfar et al. (2023). “Review of technological progress in carbon dioxide capture, storage, and utilization”. In: *Gas Science and Engineering* 117. DOI: 10.1016/j.jgsce.2023.205070.

Emiliani, C.N. et al. (2005). “QBM’s filtrate damaging effect on gas wells”. In: pp. 383–389.

Esfahani, Sadegh Mohammad Taghinejad (2023). “Experimental Investigation on Impact of Salt on CO_2 Hydrate Formation/Dissociation, and Injectivity”. Master’s thesis. Delft, Netherlands: Politecnico di Torino.

Estrada, Jose Kevin Pauyac (2023). “Transient Effects in Coupled Wellbore-Reservoir Modelling for Geological CO_2 Sequestration”. Master’s Thesis. Montanuniversität Leoben.

Fakoya, Muili F. and Ramadan M. Ahmed (2018). “A generalized model for apparent viscosity of oil-based muds”. In: *Journal of Petroleum Science and Engineering* 165, pp. 777–785. DOI: 10.1016/j.petrol.2018.03.029.

Galfré, Aurélie et al. (2011). “Carbon dioxide hydrates crystallisation in emulsion”. In: *Proceedings of the 7th International Conference on Gas Hydrates (ICGH 2011)*. Edinburgh, United Kingdom, p. 442. URL: https://hal.science/hal-00617479.

Gambelli, Alberto Maria, Mirko Filipponi, and Federico Rossi (2022). “Sequential Formation of CO_2 Hydrates in a Confined Environment: Description of Phase Equilibrium Boundary, Gas Consumption, Formation Rate and Memory Effect”. In: *Sustainability (Switzerland)* 14.14. DOI: 10.3390/su14148829.

Grigg, R.B. and G.L. Lynes (1992). “Oil-based drilling mud as a gas-hydrates inhibitor”. In: *SPE drilling engineering* 7.1, pp. 32–38. DOI: 10.2118/19560-PA.

Heidarabad, Reyhaneh Ghorbani and Kyuchul Shin (2024). “Carbon Capture and Storage in Depleted Oil and Gas Reservoirs: The Viewpoint of Wellbore Injectivity”. In: *Energies* 17.5. DOI: 10.3390/en17051201.

Hoteit, Hussein, Marwan Fahs, and Mohamad Reza Soltanian (2019). “Assessment of CO_2 injectivity during sequestration in depleted gas reservoirs”. In: *Geosciences (Switzerland)* 9.5. DOI: 10.3390/geosciences9050199.

Hu, Ruien, J. P. Martin Trusler, and John P. Crawshaw (2017). “Effect of CO_2 Dissolution on the Rheology of a Heavy Oil/Water Emulsion”. In: *Energy & Fuels* 31.4, pp. 3399–3408. DOI: 10.1021/acs.energyfuels.6b02359. URL: https://doi.org/10.1021/acs.energyfuels.6b02359.

IEAGHG (2022). *Criteria for Depleted Reservoirs to be Developed for CO_2 Storage*. Tech. rep. IEAGHG Technical Report 2022-01.

— (2024). *Managing the transition of depleted oil and gas fields to CO_2 storage*. IEAGHG Report 2024-05. DOI: 10.62849/2024-05. URL: https://doi.org/10.62849/2024-05.

Indina, V. et al. (2024). “On the Significance of Hydrate Formation/Dissociation during CO_2 Injection in Depleted Gas Reservoirs”. In: DOI: 10.2118/218550-MS.

IOGP (2025). *CO_2 Storage Projects in Europe*. URL: https://iogpeurope.org/wp-content/uploads/2025/05/CO2-Storage-Projects-in-Europe-map_May25.pdf.

Khait, Mark and Denis V. Voskov (2017). “Operator-based linearization for general purpose reservoir simulation”. In: *Journal of Petroleum Science and Engineering* 157, pp. 990–998. DOI: 10.1016/j.petrol.2017.08.009.

Kumar, Asheesh et al. (2015). “Role of Surfactants in Promoting Gas Hydrate Formation”. In: *Industrial & Engineering Chemistry Research* 54.49, pp. 12217–12232. DOI: 10.1021/acs.iecr.5b03476. URL: https://doi.org/10.1021/acs.iecr.5b03476.

Lavrik, Evgeny (2017). “Development of Quality Assurance Procedures and Methods for the CBM Silicon Tracking System”. Dissertation. Tübingen, Germany: Eberhard Karls Universität Tübingen.

Le Goff, Tuyet-Hang, Frédéric Lagarde, and Enric Santanach Carreras (2022). “A Microfluidic Experimental Approach to Assess CO_2 Hydrate Risk for CO_2 Storage into Depleted Gas Reservoirs”. In: *Proceedings of the 16th Greenhouse Gas Control Technologies Conference (GHGT-16), 23–24 October 2022*. Available at SSRN: https://ssrn.com/abstract=4284971. DOI: 10.2139/ssrn.4284971.

Li, Jin et al. (2022). “Filter Cake Removal during the Cementing and Completion Stages in CO_2 Storage Wells: Current Developments, Challenges, and Prospects”. In: *Energy Technology* 10.6. DOI: 10.1002/ente.202101134.

Li, Mingzhong et al. (2018). “Effects of sorbitan monooleate on the interactions between cyclopentane hydrate particles and water droplets”. In: *Journal of Dispersion Science and Technology* 39.3, pp. 360–366. DOI: 10.1080/01932691.2017.1318706. URL: https://doi.org/10.1080/01932691.2017.1318706.

Lv, Xiaofang et al. (2022). “Study on the Formation Characteristics of CO_2 Hydrate and the Rheological Properties of Slurry in a Flow System Containing Surfactants”. In: *ACS Omega* 7.2, pp. 2444–2457. DOI: 10.1021/acsomega.1c06523. URL: https://doi.org/10.1021/acsomega.1c06523.

Metz, Bert et al., eds. (2005). *IPCC Special Report on Carbon Dioxide Capture and Storage*. Prepared by Working Group III of the Intergovernmental Panel on Climate Change (IPCC). Cambridge, United Kingdom: Cambridge University Press, p. 431. URL: https://www.ipcc.ch/report/carbon-dioxide-capture-and-storage/.

Moslehi, S. and D. Voskov (Mar. 2025). “DARTS-well: An Open-Source Coupled Wellbore-Reservoir Numerical Model for Subsurface CO_2 Sequestration”. In: SPE Reservoir Simulation Conference. DOI: 10.2118/223892-MS.

Nimwegen, A.T. Van et al. (2023). “Cold CO_2 Injection in Depleted Gas Fields: Coupling of Wellbore and Reservoir”. In: *The Fourth EAGE Global Energy Transition Conference and Exhibition*. European Association of Geoscientists & Engineers, pp. 1–5. DOI: 10.3997/2214-4609.202321091.

Numkam, Gilles Landry and Babak Akbari (2018). “Changes in Drilling Fluid Rheology with Emulsifier Type”. In: *Proceedings of the 2018 AADE Fluids Technical Conference and Exhibition*. AADE-18-FTCE-045. American Association of Drilling Engineers. Houston, Texas, pp. 1–13.

— (2019). “Effect of surfactant chemistry on drilling mud performance”. In: *Journal of Petroleum Science and Engineering* 174, pp. 1309–1320. DOI: 10.1016/j.petrol.2018.11.075.

Oldenburg, C. M., K. Pruess, and S. M. Benson (2001). “Process Modeling of CO_2 Injection into Natural Gas Reservoirs for Carbon Sequestration and Enhanced Gas Recovery”. In: *Energy & Fuels* 15.2, pp. 293–298. DOI: 10.1021/ef000247h. eprint: https://doi.org/10.1021/ef000247h. URL: https://doi.org/10.1021/ef000247h.

Oldenburg, Curtis M. (2007). “Joule-Thomson cooling due to CO_2 injection into natural gas reservoirs”. In: *Energy Conversion and Management* 48.6. Geologic Carbon Sequestration and Methane Hydrates Research from the TOUGH Symposium 2006, pp. 1808–1815. ISSN: 0196-8904. DOI: https:

//doi.org/10.1016/j.enconman.2007.01.010. URL: https://www.sciencedirect.com/science/article/pii/S0196890407000349.

Orun, Cosmas B., Julius U. Akpabio, and Okorie E. Agwu (2023). "Drilling fluid design for depleted zone drilling: An integrated review of laboratory, field, modelling and cost studies". In: *Geoenergy Science and Engineering* 226. DOI: 10.1016/j.geoen.2023.211706.

Park, Jason, Cas Berentsen, and C. J. (Hans) de Pater (2024). "Thermal Fracture Simulation in Depleted Gas Field Carbon Capture and Storage: Implications for Injectivity and Flow Assurance". In: *SPE International Hydraulic Fracturing Technology Conference and Exhibition*. Paper SPE 215661. Presented 12–14 September 2023. Revised manuscript received 19 February 2024. Peer approved 4 March 2024. Society of Petroleum Engineers. Muscat, Sultanate of Oman.

Patil, Parimal A. et al. (2010). "Experimental study of electrical properties of oil-based mud in the frequency range from 1 to 100 MHz". In: *SPE Drilling and Completion* 25.3, pp. 380–390. DOI: 10.2118/118802-pa.

Ren, Xingwei et al. (2020). "Permeability of hydrate-bearing sediments". In: *Earth-Science Reviews* 202, p. 103100. ISSN: 0012-8252. DOI: https://doi.org/10.1016/j.earscirev.2020.103100. URL: https://www.sciencedirect.com/science/article/pii/S001282521930323X.

Sandoval, D. et al. (2019). "Influence of Adding Asphaltenes and Gas Condensate on CO_2 Hydrate Formation in Water–CO_2–Oil Systems". In: *Journal of Natural Gas Science and Engineering*.

Scheffer, B.B. (2022). "The impact of thermal fracturing on the near-wellbore region during CO_2 injection in depleted gasfields: a numerical investigation". Supervisors: Femke C. Vossespoel, Alexandros Daniilidis; Committee: A. Barnhoorn. Master Thesis. Delft University of Technology. URL: https://resolver.tudelft.nl/uuid:2f48aADF-cf15-4f8d-bdd5-538cddc0614f.

Schellart, Manon Arianne Renée (2024). "Impact of pore scale heterogeneity on salt precipitation and hydrate formation during CO_2 storage in porous media". Master's thesis. Delft University of Technology.

Sinquin, A. et al. (2001). "Kinetics of Hydrate Formation: Influence of Crude Oils". In: *SPE Annual Technical Conference and Exhibition*. SPE-71543-MS.

Skogestad, Jan Ole et al. (2024). "ASSESSING HYDRATE FORMATION RISK IN INFILL CCS WELLS". In: vol. 8. American Society of Mechanical Engineers (ASME). DOI: 10.1115/OMAE2024-122640. URL: https://www.scopus.com/inward/record.uri?eid=2-s2.0-85210034296&doi=10.1115%2fOMAE2024-122640&partnerID=40&md5=30bad4e9f765c4c041a6bffa294efed0.

Sloan, E. D. and C. A. Koh (2008). *Clathrate Hydrates of Natural Gases*. 3rd. Boca Raton, FL: CRC Press—Taylor and Francis Group LLC.

Song, Jia and Zhigao Sun (2022). "Can surfactant promote cyclopentene hydrate formation for cool storage?" In: *Journal of Molecular Liquids* 368, p. 120655. ISSN: 0167-7322. DOI: https://doi.org/10.1016/j.molliq.2022.120655. URL: https://www.sciencedirect.com/science/article/pii/S0167732222021948.

Strpić, Kristina (2022). "Coupled Wellbore–Reservoir Simulation of Thermal Effects During Multiphase CO_2 Injection". Doctorate in Civil, Chemical, Environmental, and Materials Engineering (Ciclo XXXIV). PhD Thesis. Italy: University of Bologna.

Sun, Guangyu et al. (2018). "Effects of Dissolved CO_2 on the Crude Oil/Water Interfacial Viscoelasticity and the Macroscopic Stability of Water-in-Crude Oil Emulsion". In: *Energy & Fuels* 32.9, pp. 9330–9339. DOI: 10.1021/acs.energyfuels.8b02180. URL: https://doi.org/10.1021/acs.energyfuels.8b02180.

Sun, Jinsheng et al. (2018). "Development of key additives for organoclay-free oil-based drilling mud and system performance evaluation". In: *Petroleum Exploration and Development* 45.4, pp. 764–769. DOI: 10.1016/s1876-3804(18)30079-x.

Sun, Xiaohui et al. (2022). "Experiments and modeling of CO_2 solubility in water-based and oil-based drilling fluids". In: *Journal of Petroleum Science and Engineering* 212, p. 110336. ISSN: 0920-4105. DOI: https://doi.org/10.1016/j.petrol.2022.110336. URL: https://www.sciencedirect.com/science/article/pii/S0920410522002236.

Voronov, V.P. et al. (2016). "Properties of equilibrium carbon dioxide hydrate in porous medium". In: *Chemical Physics* 476, pp. 61–68. ISSN: 0301-0104. DOI: https://doi.org/10.1016/j.chemphys.2016.05.031. URL: https://www.sciencedirect.com/science/article/pii/S0301010415300707.

Waite, W.F. et al. (2009). “Physical properties of hydrate-bearing sediments”. In: *Reviews of Geophysics* 47.4, pp. 465–484. DOI: 10.1029/2008RG000279.

Wan, N.-H. et al. (2021). “Modeling Transient Flow in CO_2 Injection Wells by Considering the Phase Change”. In: *Processes* 9.12, p. 2164. DOI: 10.3390/pr9122164.

Xu, Zelin and Yoshihiro Konno (2025). “Morphological Change of Hydrate Caused by Ostwald Ripening and Sintering”. In: *Energy and Fuels* 39.9, pp. 4238–4248. DOI: 10.1021/acs.energyfuels.4c05531.

Yamada, Kenta et al. (2024). “Development of a hydrate risk assessment tool based on machine learning for CO_2 storage in depleted gas reservoirs”. In: *Fuel* 357, p. 129670. ISSN: 0016-2361. DOI: https://doi.org/10.1016/j.fuel.2023.129670. URL: https://www.sciencedirect.com/science/article/pii/S0016236123022846.

Al-Yami, AS et al. (2018). “Emulsifiers Used in Designing Emulsion Based Drilling Fluids”. In: *Research & Reviews: Journal of Chemistry* 7.4. ISSN: 2319-9849, pp. 9–20. URL: https://www.rroij.com/open-access/emulsifiers-used-in-designing-emulsion-based-drilling-fluids.php.

Yan, Lida and Ganesh Balasubramanian (2023). “Examining the Hydration Behavior of Aqueous Calcium Chloride (CaCl2) Solution via Atomistic Simulations”. In: *Physchem* 3.3, pp. 319–331. ISSN: 2673-7167. DOI: 10.3390/physchem3030022. URL: https://www.mdpi.com/2673-7167/3/3/22.

Yan, Lifei (2024). *Experimental setup for CO_2 hydrate in microfluidics*. Experimental procedure, Reservoir Engineering Laboratory, Delft University of Technology.

Yan, Lifei et al. (2023). “Direct Evidence of Salinity Difference Effect on Water Transport in Oil: Pore-Scale Mechanisms”. In: *Energy and Fuels* 37.20, pp. 15537–15552. DOI: 10.1021/acs.energyfuels.3c02245.

You, Kehua et al. (2015). “Salinity-buffered methane hydrate formation and dissociation in gas-rich systems”. In: *Journal of Geophysical Research: Solid Earth* 120.2, pp. 643–661. DOI: 10.1002/2014JB011190.

Zhang, Dongxu et al. (2021). “Effects of waxes and asphaltenes on CO2 hydrate nucleation and decomposition in oil-dominated systems”. In: *Journal of Natural Gas Science and Engineering* 88. DOI: 10.1016/j.jngse.2021.103799.

A

Reservoir Parameter for Decoupled Reservoir Simulation

Table A.1: Reservoir and Injection Parameters (modified from Curtis M. Oldenburg (2007))

Parameter	Value	Unit
Reservoir Top Depth	1000	m
Reservoir Temperature	45	$^{\circ}$C
Reservoir Pressure	25	bar
Thickness	50	m
Permeability	50	mD
Porosity	0.3	-
S_w	0.2	-
Reservoir Radius	1130	m
Reservoir Boundary	Infinite	-
Grid number (nr)	100	-
Wellbore radius	0.1	m
Injection Rate	3	kg/s
	140000	m^3/d
Injection Fluid	100% CO_2	-
Injection Temperature	15	$^{\circ}$C
Rock heat capacity	1000	J/(kg·$^{\circ}$C)
Rock heat conductivity	2.51	W/(m·$^{\circ}$C)
Radius of Damage	1	meter

B

Governing Equations for Coupled Wellbore-Reservoir Simulations

This study utilizes the open-source numerical framework DARTS-well, which couples a non-isothermal, multi-segment, multi-phase wellbore model, formulated using the Drift-Flux Model (DFM) with the Delft Advanced Reservoir Terra Simulator (DARTS) for reservoir modeling (Moslehi and D. Voskov, 2025). The simulator adopts the Operator-Based Linearization (OBL) technique to handle complex physical interactions efficiently while substantially reducing computational costs (**KHAIT2017990**; Moslehi and D. Voskov, 2025). The simulation framework is configured using the Pressure-Enthalpy (PH) formulation and incorporates the effects of gravitational potential energy. The modeling scenario involves a single-component CO_2 system with two-phase (gas and liquid) flow. The governing equations used in this study are presented as follows:

Reservoir Mass Conservation

$$\frac{\partial(\phi\rho_i S_i)}{\partial t} + \nabla \cdot (\rho_i \mathbf{v}_i) = q_i \tag{B.1}$$

- ϕ: porosity
- ρ_i: phase density
- S_i: phase saturation
- $\mathbf{v}_i$: Darcy velocity
- q_i: source/sink term

Reservoir Energy Conservation

$$\frac{\partial(\phi\rho h)}{\partial t} + \nabla \cdot (\rho h \mathbf{v}) = Q + q_h \tag{B.2}$$

- h: enthalpy
- Q: heat transfer (often neglected in isothermal models)
- q_h: enthalpy source/sink

Wellbore Mass Conservation Equation
For a one-dimensional vertical wellbore discretized into segments, the mass conservation equation for each segment is given by:

$$\frac{\partial}{\partial t}(\rho_m A \Delta z) + \sum_{i=1}^{n_{faces}} (\rho_m v_m A)_i = q_m \tag{B.3}$$

where:

- ρ_m is the mixture density,
- v_m is the mixture velocity,
- A is the cross-sectional area,
- Δz is the segment length,
- q_m is the source/sink mass term.

Wellbore Momentum Conservation Equation
The momentum balance accounts for pressure gradient, gravitational head, and frictional losses:

$$\rho_m \frac{dv_m}{dt} = -\frac{\partial p}{\partial z} - \rho_m g \cos(\theta) - \frac{f_f}{D}\frac{\rho_m v_m |v_m|}{2} \tag{B.4}$$

where:

- p is pressure,
- g is gravitational acceleration,
- θ is inclination angle,
- f_f is the Fanning friction factor,
- D is the pipe diameter.

Wellbore Energy Conservation Equation
Using Pressure-Enthalpy (PH) formulation and considering potential energy:

$$\frac{\partial}{\partial t}(\rho_m h_m A \Delta z) + \sum_{i=1}^{n_{faces}} (\rho_m h_m v_m A)_i = q_E - \rho_m g z v_m A \tag{B.5}$$

where:

- h_m is the mixture enthalpy,
- q_E is the net heat addition (e.g., from ambient),
- z is the elevation (TVD).

Drift-Flux Model
The phase velocities v_g and v_l are modeled using the drift velocity approach:

$$v_g = C_0 v_m + v_d \tag{B.6}$$

$$v_l = \frac{v_m - \alpha_g v_g}{1 - \alpha_g} \tag{B.7}$$

where:

- C_0 is the profile parameter,
- v_d is the drift velocity,
- α_g is gas holdup.

Coupling Between Wellbore and Reservoir

At the perforation interface:

- Mass and enthalpy flux continuity is enforced between the well segment and the adjacent reservoir cell:

$$\dot{m}_{\text{in}} = \dot{m}_{\text{res}} = \dot{m}_{\text{wb}} \quad , \quad \dot{H}_{\text{in}} = \dot{H}_{\text{res}} = \dot{H}_{\text{wb}} \tag{B.8}$$

with phase split based on pressure and enthalpy from the well/reservoir interface.

C

Repeat Experiment #3: NaCl-1wt% + Dodecane

In the main Experiment #3, hydrate dissociation occurred unintentionally due to a pressure drop caused by an operational issue. Therefore, a repeat experiment was conducted to systematically investigate the dissociation temperature for the NaCl-1wt% + Dodecane system.

Figure C.1 presents the pressure, temperature, and hydrate saturation profiles during the dissociation process in the repeat experiment. The pressure was maintained at 25 bar, while the temperature was increased stepwise—from -1°C to 3°C, then from 3°C to 5°C, and finally from 5°C to 8°C.

Throughout the temperature increase, the hydrate saturation remained relatively stable at approximately 1.6–2%. The dissociation temperature was identified as the point where hydrate saturation began to decrease significantly. According to the figure, dissociation was observed within the temperature range of 5.1–5.6°C.

Figure C.2 and Figure C.3 display micromodel images taken before and after hydrate dissociation, respectively. In Figure C.3, the disappearance of hydrate features confirms that dissociation occurred.

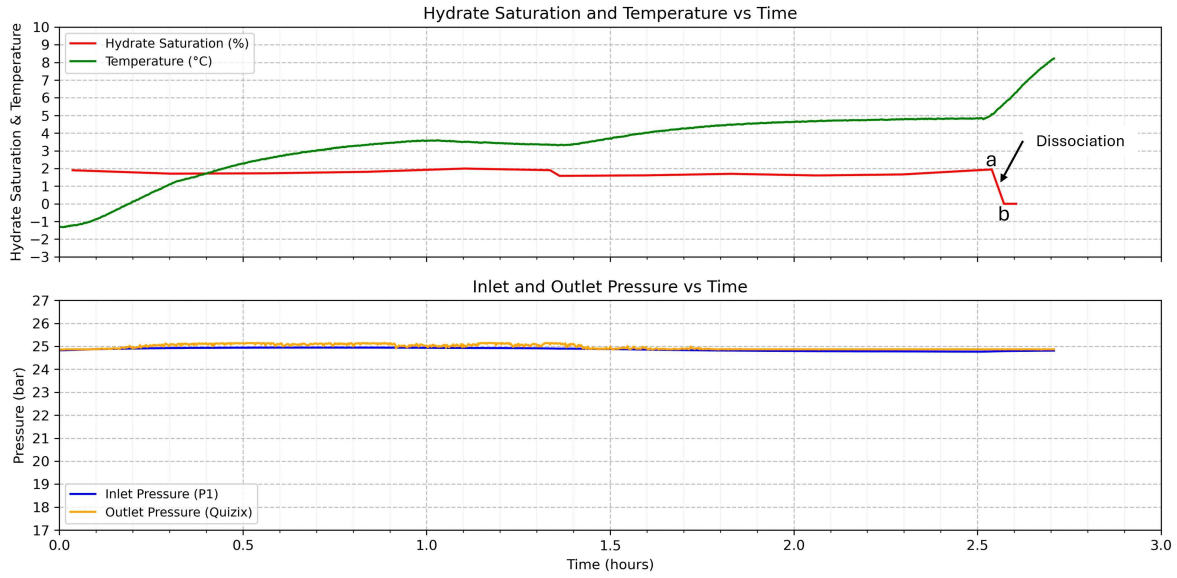

Figure C.1: Hydrate saturation, temperature, and pressure profile during the dissociation process in repeated Experiment #3.

(a) t = 2.54 hours

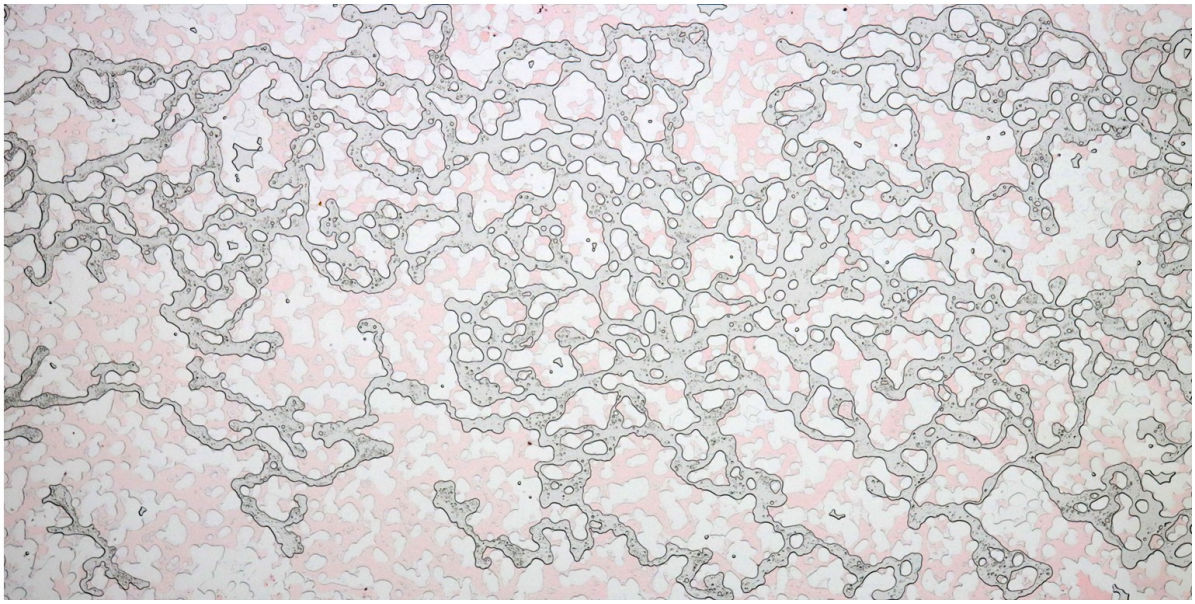

Figure C.2: Micromodel image before dissociation (t = 2.54 hours) during repeated Experiment #3.

(b) t = 2.57 hours

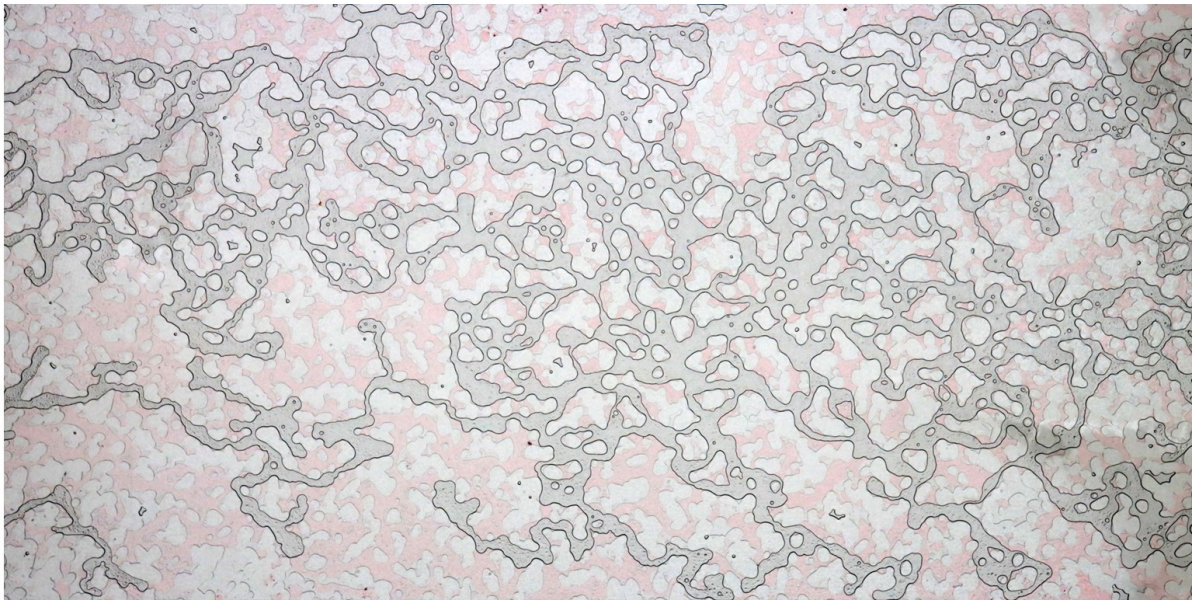

Figure C.3: Micromodel image after dissociation (t = 2.57 hours) during repeated Experiment #3.

D

Repeat Experiment #4: $CaCl_2$-15wt% + Dodecane

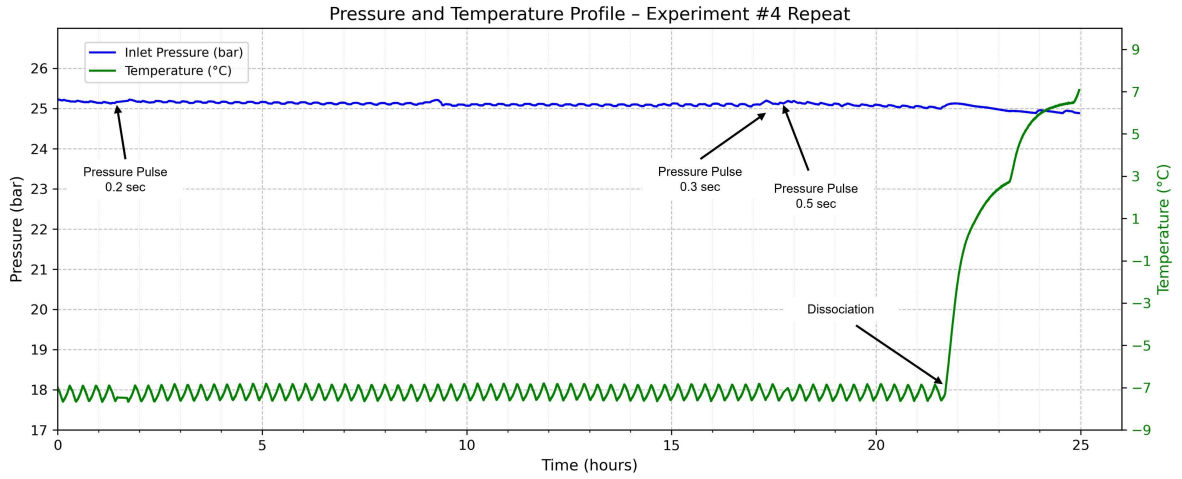

Figure D.1: Pressure and temperature profile during repeated Experiment #4.

Figure D.1 shows the pressure and temperature profile during repeated Experiment #4 ($CaCl_2$-15wt% + Dodecane). This experiment was conducted to verify whether hydrate formation occurred and to identify if the 'dark feature' observed inside the CO_2 channel was indeed a hydrate.

CO_2 was injected for two hours, followed by the application of a 0.2-second pressure pulse to trigger hydrate nucleation. The system was then monitored for 15 hours. During this period, no hydrate formation was observed, while the dark feature inside the CO_2 channel persisted.

Subsequently, another pressure pulse of 0.3 seconds was applied. After 30 minutes, the visual appearance of the feature remained unchanged, similar to the observation after the first pulse. A final pulse of 0.5 seconds was then applied, followed by four additional hours of monitoring. Again, no hydrate formation was observed; only a persistent 'dark feature' was present, visually consistent with that seen in the main Experiment #4.

To confirm the nature of this feature, a dissociation test was performed by increasing the temperature in a stepwise manner up to 9 °C. As shown in Figure D.3, the feature inside the CO_2 channel did not dissociate even at this elevated temperature. This suggests that the dark feature was not a hydrate.

Thus, the results of this repeat experiment are consistent with the main Experiment #4: no hydrate formation occurred throughout the experiment.

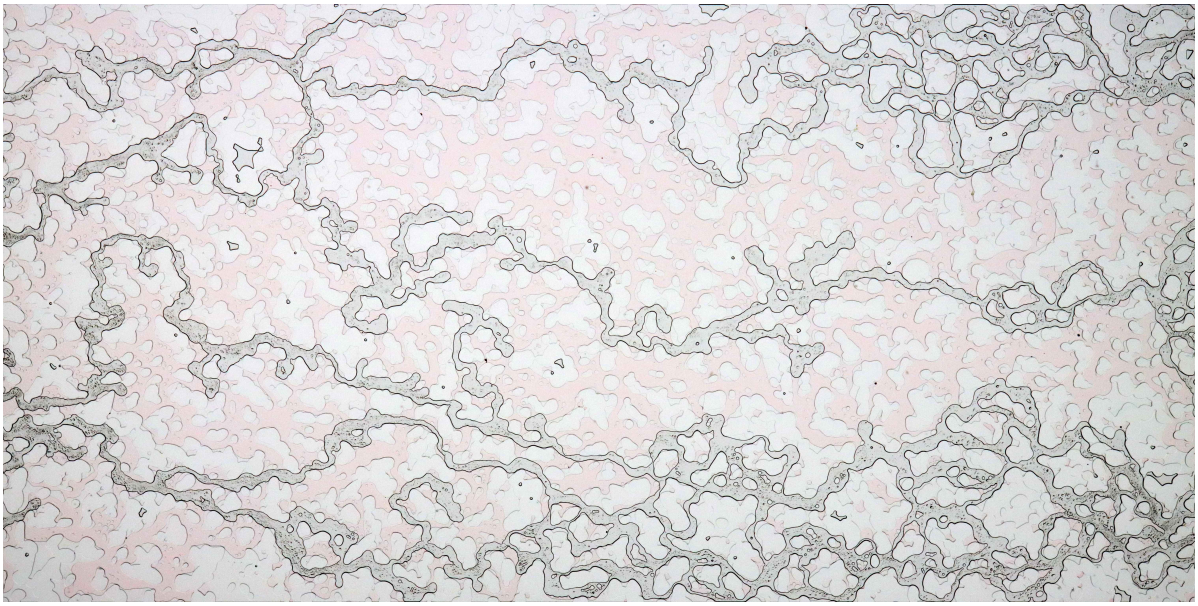

Figure D.2: Micromodel image before dissociation process in repeated Experiment #4.

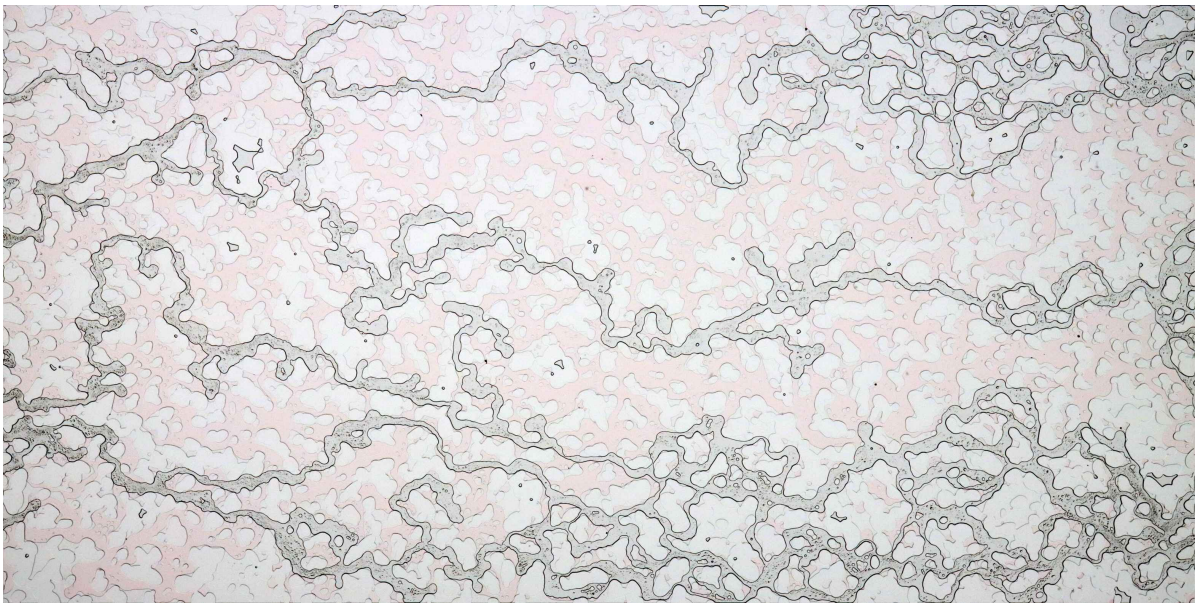

Figure D.3: Micromodel image at 9 °C during the dissociation test in repeated Experiment #4.

E

Appendix of Coupled Wellbore-Reservoir Simulations Result

Impact of Permeability of the Damaged-Zone (K_d)

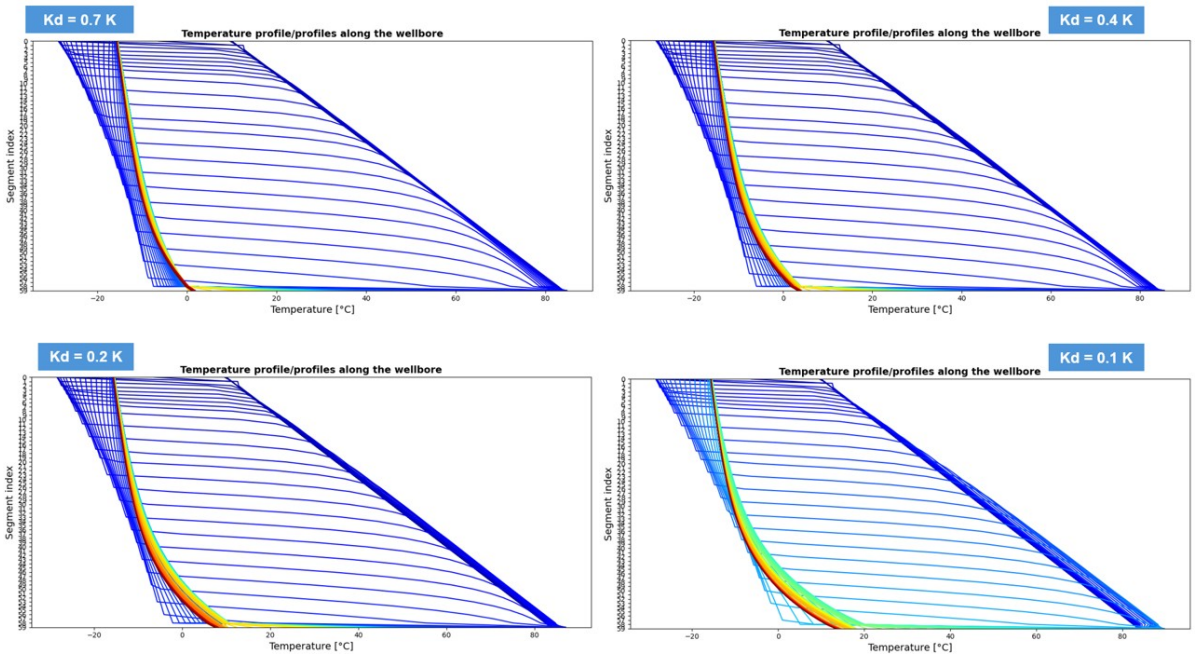

Figure E.1: Temperature profile along the wellbore over time for various value of K_d.

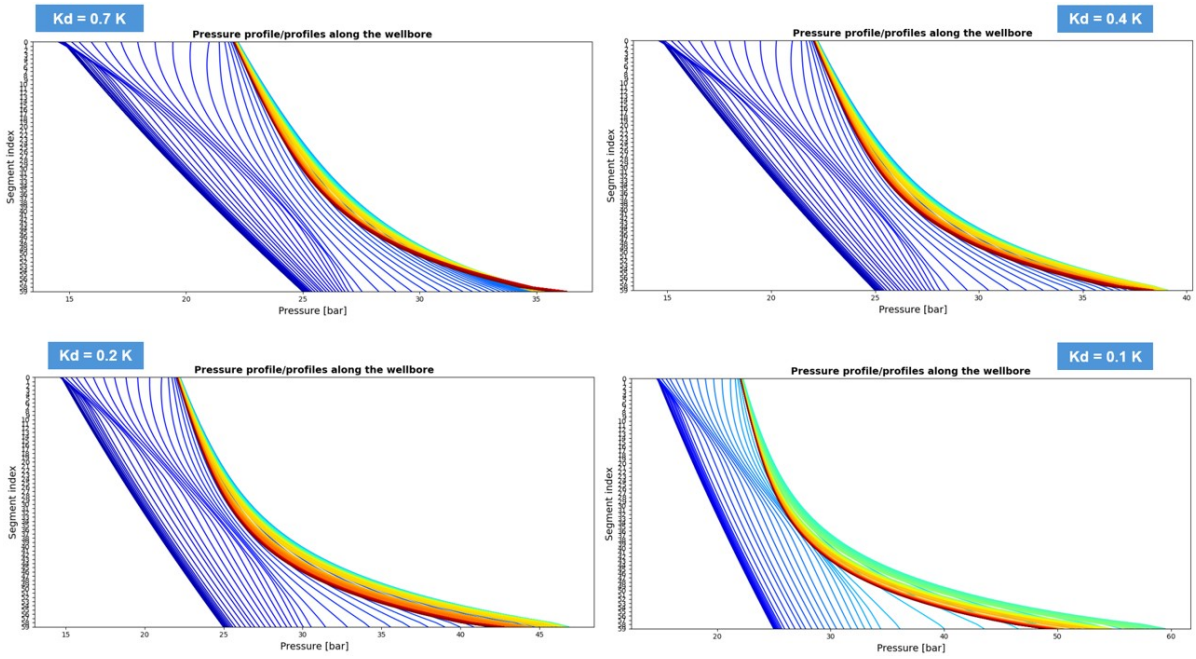

Figure E.2: Pressure profile along the wellbore over time for various value of K_d.

The Risk of Hydrate Formation as the Impact of Permeability of the Damaged-Zone

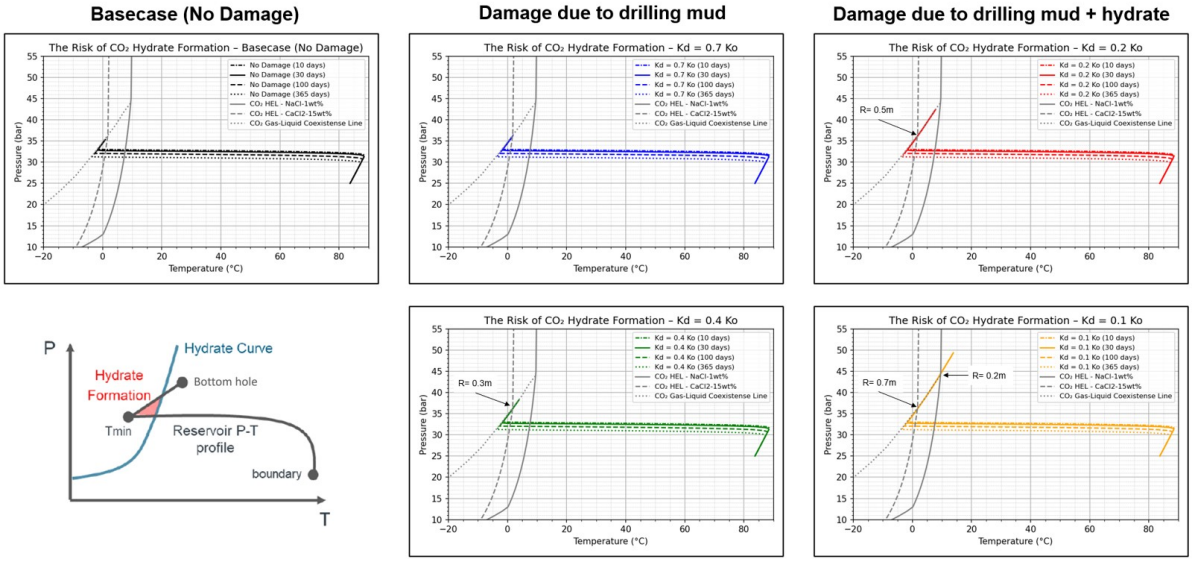

Figure E.3: The risk of hydrate formation as the impact various value of K_d.

Impact of Radius of the Damaged-Zone (R_d)

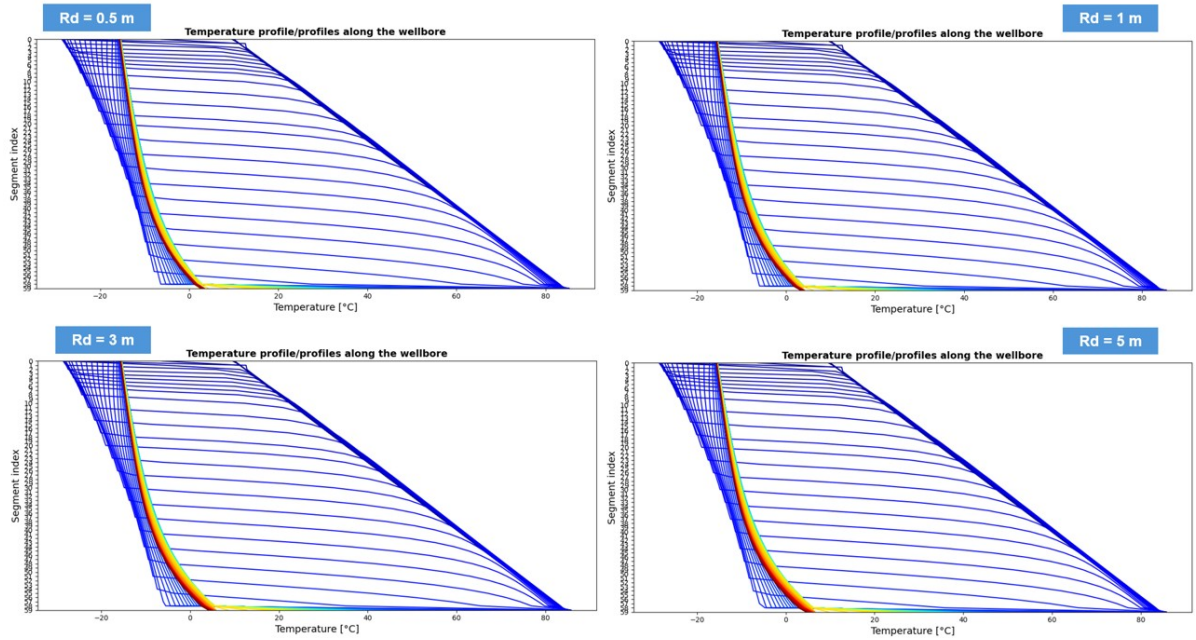

Figure E.4: Temperature profile along the wellbore over time for various value of R_d.

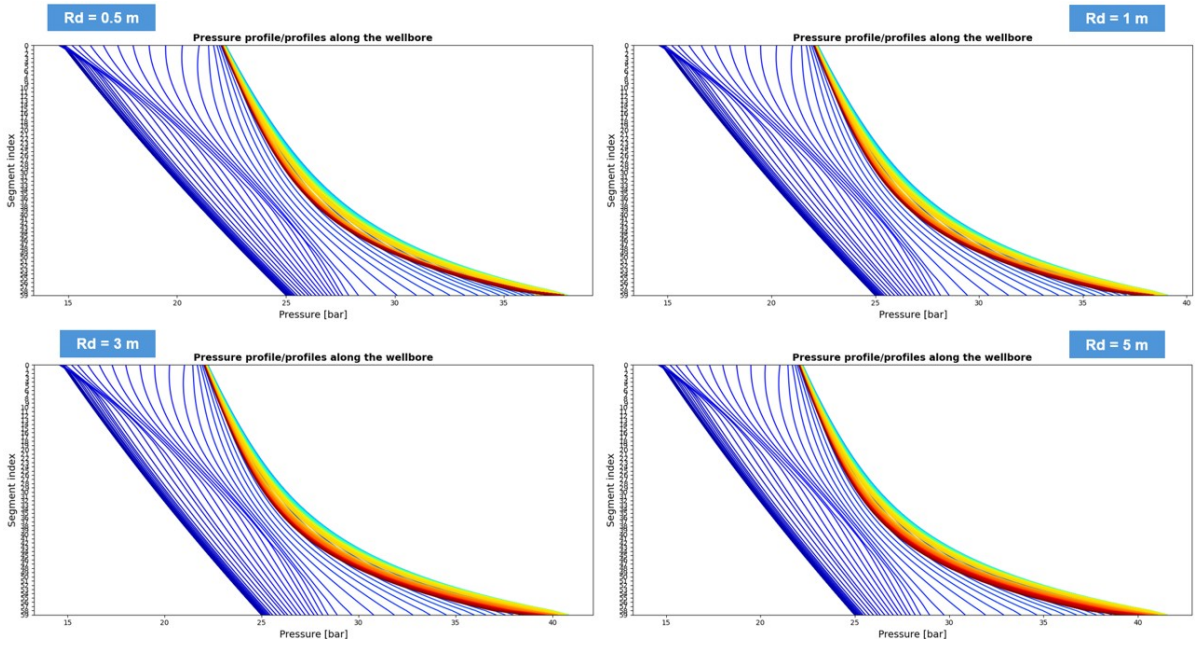

Figure E.5: Pressure profile along the wellbore over time for various value of R_d.